From Synthesis to Electrochemical Applications of Electroactive Polymer Composites and Hybrid Materials

Lead Guest Editor: Hoang Vinh Tran
Guest Editors: Viet Hai Le and Benoit Piro

From Synthesis to Electrochemical Applications of Electroactive Polymer Composites and Hybrid Materials

From Synthesis to Electrochemical Applications of Electroactive Polymer Composites and Hybrid Materials

Lead Guest Editor: Hoang Vinh Tran
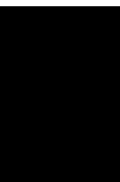Guest Editors: Viet Hai Le and Benoit Piro

Chief Editor

Contents

WILEY | Hindawi

Research Article

Poly(1,5-Diaminonaphthalene)-Modified Screen-Printed Device for Electrochemical Lead Ion Sensing

Mai T. T. Nguyen (ID),[1] **Huy L. Nguyen** (ID),[1,2] **and Dung T. Nguyen** (ID)[2]

[1]*School of Chemical Engineering, Hanoi University of Science and Technology, 1 Dai Co Viet Road, Hanoi, Vietnam*
[2]*Institute for Tropical Technology, Vietnam Academy of Science and Technology, 18 Hoang Quoc Viet Road, Hanoi, Vietnam*

Correspondence should be addressed to Huy L. Nguyen; huy.nguyenle@hust.edu.vn and Dung T. Nguyen; ndung@itt.vast.vn

Poly(1,5-diaminonaphthalene) has been electropolymerized on the screen-printed device with a three-electrode configuration. The modified electrodes have been developed as the new electrode for electrochemical determination of trace levels of lead ions (Pb^{2+}). The poly(1,5-diaminonaphthalene) film prevents the deposition of Pb^{2+} into the surface defects of the bare carbon screen-printed electrode and possesses sensitivity to heavy metal ions thanks to amine and secondary amino groups on the polymer chain. The square wave anodic stripping voltammetry was applied to detect Pb^{2+} ions, showing a sharp stripping peak with the linear range from $0.5\,\mu g \cdot L^{-1}$ to $5.0\,\mu g \cdot L^{-1}$ ($R^2 = 0.9929$). The limit of detection was found to be $0.30\,\mu g \cdot L^{-1}$. The sensors were applied to the analysis of Pb^{2+} in the tap water sample matrix with satisfactory results.

1. Introduction

At present, lead is one of the most critical toxic pollutants for biological systems. Lead is not biodegradable and accumulated in the food chain, so this metal remains a significant health concern. Exposure to even a low level of lead ions (Pb^{2+}) may cause severe damage to the brain and kidneys [1]. According to the stipulation of the European Union, the maximum allowable concentrations in food have been set to be from 0.02 to $1\,mg \cdot L^{-1}$ [2], and as for the World Health Organization (WHO), it has been set as $10\,\mu g \cdot L^{-1}$ for drinking water [3]. Due to these reasons, the rapid detection of Pb^{2+} at lower concentration levels is an important issue. A series of methods have been used for the detection of Pb^{2+}, such as Atomic Absorption Spectroscopy (AAS) [4], Inductively Coupled Plasma Mass Spectroscopy (ICP-MS) [5], and X-Ray Fluorescence (XRF) spectrometry [6]. Using these methods, we can detect high accuracy and high sensitivity, but some disadvantages include bulky equipment size, expensive cost, a requirement of trained professionals, and large-scale analysis for indoor use. Besides, the electrochemistry method with the anodic stripping voltammetry (ASV)

technique is also a powerful tool for detecting trace amounts of Pb^{2+}. The advantages of the electroanalytical method are its rapid detection, small size, easy operation, and high sensitivity. The working electrodes based on the hanging drop mercury electrodes (HDME), dropping mercury electrodes (DME), and mercury film electrodes (MFE) have been widely reported during the past several decades [7]. However, mercury is toxic and unsuitable for portable devices. To date, there is a tendency to use the alternative of mercury electrodes (mercury-free) such as inorganic materials like bismuth [8], functionalized mesoporous silica [9], boron-doped diamond [10], nanoscale carbon materials [11–13], and boron-doped diamond [14]. The polymer electrodes based on the conductive polymer film have been investigated toward metal ion detection with different approaches.

The conducting polymer's interesting features are its superior electrical conductivity, high specific surface area, good adhesion, and enhanced signal responses for target metal ions [15]. A large number of reports have shown that people used polymer composite electrodes for detection of Pb^{2+} such as polyaniline/carbon nanotubes [16], poly(vinylsulfonate)-doped polyaniline [17], *p*-phenylenediamine [18], poly(3,4-
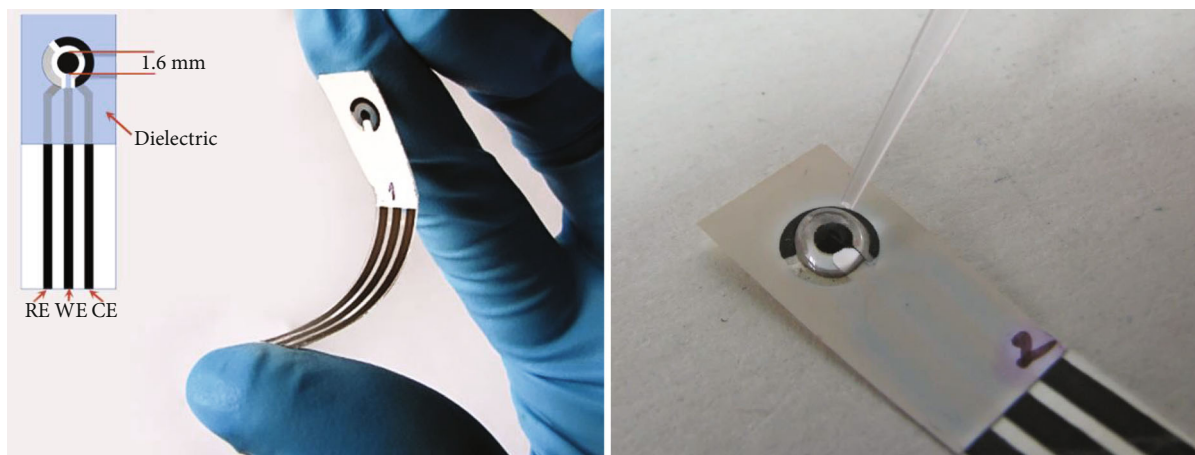
Figure 1: The illustration of the screen-printed devices with a three-electrode configuration.
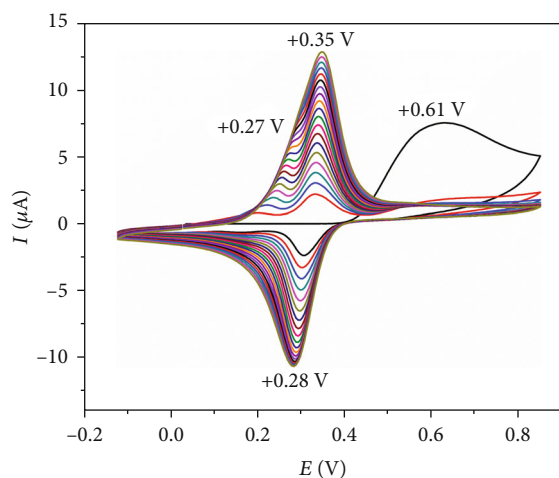
Figure 2: Cyclic voltammetric curves during p(1,5-DAN) film growth onto SPEs for 20 cycles. Solution: 1 mM of 1,5-DAN and 0.1 M LiClO$_4$ in 1 M HClO$_4$; scan rate: 50 mV·s^{-1}.

(a) Bare SPEs
(b) p(1,5-DAN)/SPEs

Figure 3: CVs of bare SPEs (curve (a)) and p(1,5-DAN)/SPEs (curve (b)) in 0.1 M acetate buffer (pH 4.5) with the scan rate of 50 mV·s^{-1}.

ethylenedioxythiophene) [19], polypyrrole/carbon nanofibers [20], PEDOT/black TiO$_2$ [21], and polydiaminonaphthalene [22, 23]. Among these conducting polymers, poly(1,5-diaminonaphthalene) (p(1,5-DAN)) has shown the capacity of collecting some metal ions because it possesses chelating properties and/or reduction properties owing to the electron-donating groups (amine and secondary amino groups) on the polymer chain [24]. Thus, p(1,5-DAN) could increase the stripping responses and the reproducibility for sensing.

Most of the work about polymer electrodes is based on the glassy carbon electrodes and carbon paste electrodes, which is not suitable for on-site applications. A screen-printed electrode emerged as a promising solution for this problem. The coupling of a screen-printed electrode with anodic stripping voltammetry (ASV) is more favorable in the heavy metal analysis due to the following: prepared in large quantities, rapid, inexpensive, flexible, and miniaturization. This study is aimed at preparing for a "*lab-made*" screen-printed device with a three-electrode configuration (consisting of the silver chloride pseudoreference electrode;

carbon as a working electrode, and counter electrode) modified by p(1,5-DAN) for square wave anodic stripping voltammetry (SWASV) analysis of lead ions.

2. Materials and Methods

2.1. Reagents and Apparatus. 1,5-Diaminonaphthalene monomer, LiClO$_4$, and HClO$_4$ were obtained from Sigma-Aldrich. Lead solutions were prepared from a standard stock solution (1,000 mg·L^{-1}, atomic absorption standard solution, Scharlau Chemie). Sodium acetate buffer (0.1 M, pH 4.5), prepared by mixing an appropriate amount of CH$_3$COOH and CH$_3$COONa, was used as a supporting electrolyte. All other reagents of analytical grade and deionized water were used throughout the experiments.

The bare screen-printed devices with a three-electrode configuration (SPEs) were fabricated on a polypropylene sheet substrate with a DEK Albany 247 printing machine (DEK, Weymouth, UK). These "*lab-made*" SPEs have dimensions about 1 cm × 4 cm with a classical three-electrode system,

(a)

(b)
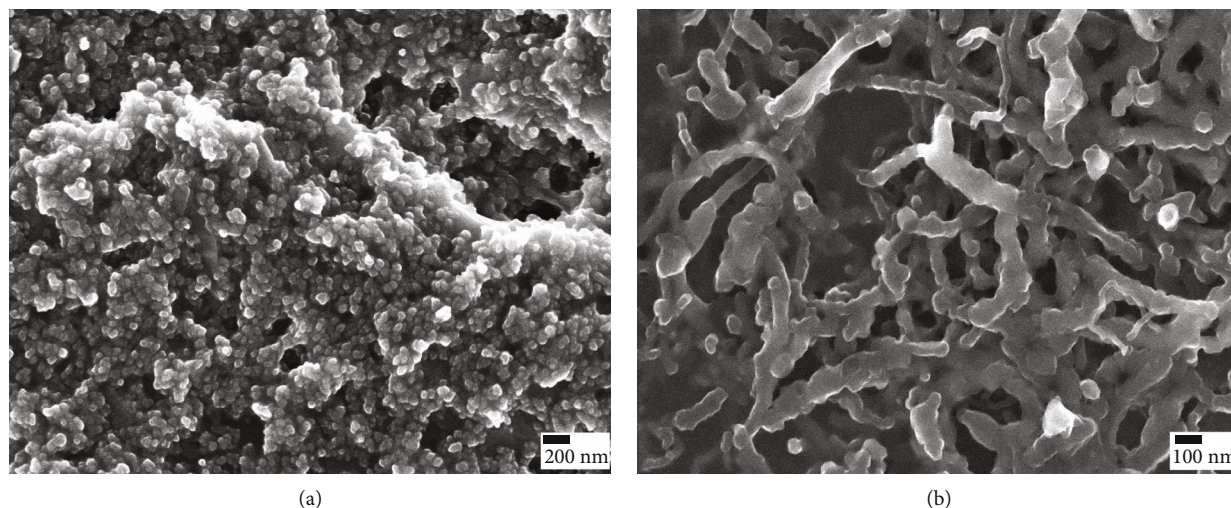
FIGURE 4: SEM image of (a) bare SPEs and (b) p(1,5-DAN)/SPEs.

including a silver chloride-based screen-printed pseudoreference electrode, carbon working electrode, and carbon counter electrode. The SPE fabrication process was described in our previous publication [25]. The working carbon electrode diameter was 1.6 mm in a geometric area of 0.02 cm^2 with the thickness of coated layers of about 10 μm. The ratio counter electrode/working electrode surface area was 4/1, and the silver chloride pseudoreference electrode with $E_{ref.} \approx +0.3$ V and standard hydrogen electrode (SHE) are shown in Figure 1.

All electrochemical experiments were performed with an Autolab PGSTAT30 electrochemical analyzer (EcoChemie, the Netherlands) under the control of GPES version 4.9 data acquisition software. The electrochemical setup measurements were performed with the reaction solution's droplet (15−50 μL) at room temperature (~25°C) and nondeaerated solutions. The morphology was observed by field emission scanning electron microscopy (FE-SEM; Hitachi S-4800).

2.2. SPEs Modified by p(1,5-DAN). The p(1,5-DAN) film was electrochemically synthesized on SPEs in an aqueous solution consisting of the 1,5-diaminonaphthalene monomer with a concentration of 1.0 mM and 0.1 M LiClO$_4$ in a 1 M HClO$_4$ using cyclic voltammetry. The polymerization was performed in 20 cycles within the potential range from -0.02 V to +0.95 V with a sweep rate of 50 mV·s^{-1}. Afterward, the produced electrodes p(1,5-DAN)/SPEs were washed with deionized water.

2.3. Procedure for the SWASV Analysis. Square wave anodic stripping voltammetry is a frequently used anodic stripping voltammetry method because it can greatly reduce the background noise coming from the charging current during the potential scan [26]. The detection of Pb^{2+} was performed for various concentrations of Pb^{2+} in 0.1 M acetate buffer (pH 4.5) using square wave voltammetry under the following conditions: frequency of 50 Hz, amplitude of 50 mV, and step potential of 5 mV. The stripping voltammetric measurement procedure consisted of two steps: an accumulation step and a stripping step. Firstly, lead ions were deposited on the surface electrode at the negative potential for 180-480 s.
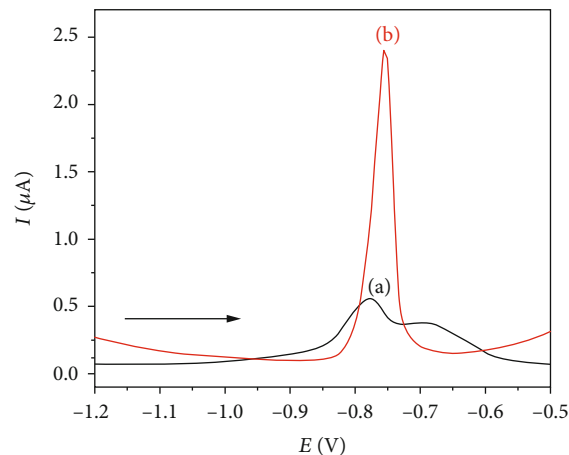
FIGURE 5: SWASV of 4.5 μg·L^{-1} Pb^{2+} in acetate buffer (pH 4.5) at bare SPEs (a) and p(1,5-DAN)/SPEs (b). Deposition potential: -1.2 V; deposition time: 360 s.

Then, the square wave anodic stripping voltammograms (SWASV) are recorded by applying a positive-going scan from -1.2 to -0.5 V.

3. Results and Discussion

3.1. Electropolymerization of p(1,5-DAN) on the SPEs. Figure 2 displays the cyclic voltammograms between -0.02 and +0.95 V at a scan rate of 50 mV·s^{-1} taken during the electrochemical polymerization onto SPEs. In the first scan, the anodic peak at around +0.61 V corresponds to the 1,5-diaminonaphthalene monomer oxidation to the radical cation than the dication. In subsequent cycles, this peak seems to disappear, but at lower potentials, two anodic peaks are obtained at +0.27 V and +0.35 V and one cathodic peak at +0.28 V. The characteristic peaks characterized show electroactivity of p(1,5-DAN) in acid medium, and the current continuously increased during scans reflecting the growth of the conductive polymer film on the SPEs [23, 27–29].

(a)

(b)
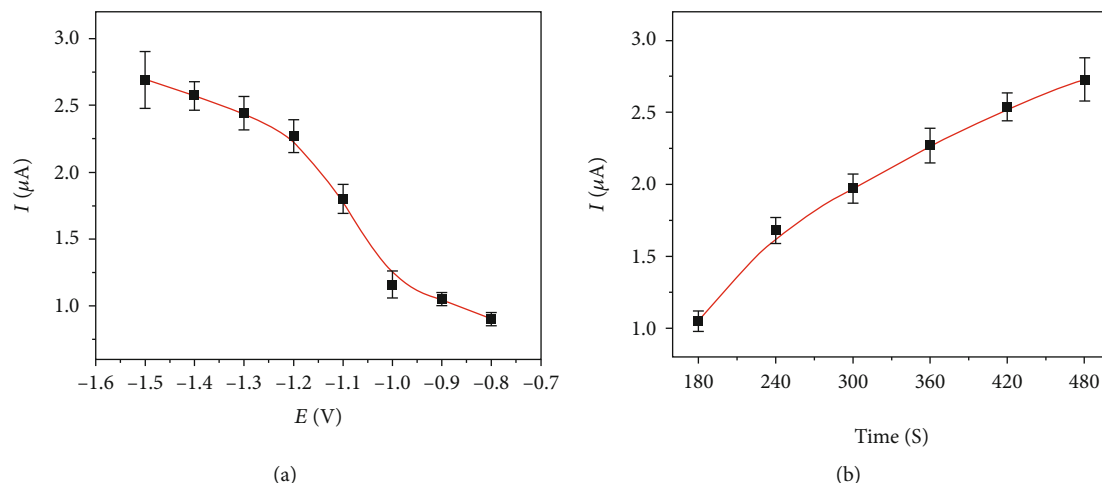
FIGURE 6: Effect of deposition potential (a) and deposition time (b) of $4.5\,\mu g \cdot L^{-1}$ Pb^{2+} detection in acetate buffer (pH 4.5) on p(1,5-DAN)/SPEs.

To confirm the successful polymerization of 1,5-diaminonaphthalene on SPEs, the electrodes were obtained by scanning the cyclic voltammograms in acetate buffer solution (pH 4.5) in the absence of the monomer. The cyclic voltammetry was performed between -1.5 V and +0.25 V at a scan rate of $50\,mV \cdot s^{-1}$.

As shown in Figure 3, the cyclic voltammogram of p(1,5-DAN)/SPEs (curve (b)) has shown two typical redox couples (I_1/I_1' and I_2/I_2') corresponding to doping and undoping of protons and anions in the p(1,5-DAN) film [28] clearly seen when compared with CVs of bare SPEs (curve (a)) under the same conditions. This result confirmed the successful polymerization of 1,5-DAN on screen-printed devices.

The working potential window's width is important for determining heavy metal ions with the anodic stripping voltammetry technique. As shown in Figure 3 (curve (b)), the voltammogram was almost straight from -1.5 V to -0.4 V (not affected by oxidation peaks of the polymer) and did not show an apparent influence of hydrogen evolution currents until -1.5 V. And the anodic peak for Pb^{2+} ion stripping is inside this potential range. That proves that the p(1,5-DAN)/SPEs are suitable for electrochemical determination of Pb^{2+} in acetate buffer electrolyte solution. The wide range of potential is promising for anodic stripping voltammetry of heavy metals such as Zn^{2+}, Cd^{2+}, and Cu^{2+}.

3.2. Morphological Characteristics. The scanning electron microscope (SEM) morphologies of the bare SPEs and p(1,5-DAN)/SPEs were characterized by scanning electron microscopy, as shown in Figure 4. The bare carbon electrode was displayed with many dispersing small particles (Figure 4(a)). The small particles can be assigned as the carbon particles dispersed in a conductive screen printable ink. After electropolymerization, the morphology of the electrode changed significantly. The fabricated p(1,5-DAN) has a porous structure with a large active area and is homogeneously distributed throughout the electrode surface. The most widely accepted p(1,5-DAN) polymerization mechanism is the radical-mediated one, as reported in previous
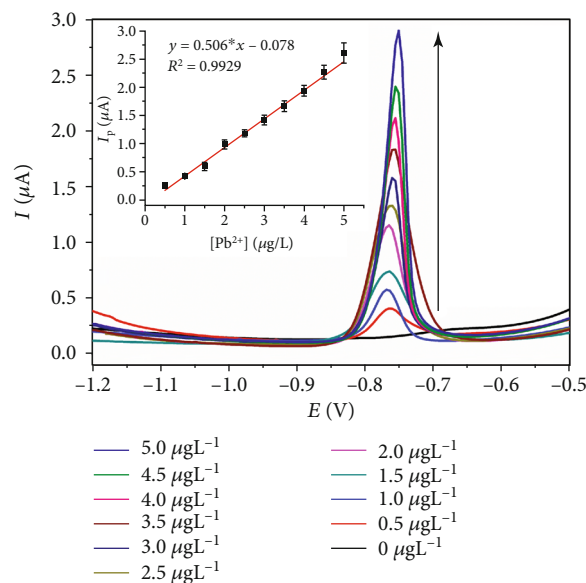
FIGURE 7: The SWASV response for the increasing concentration of Pb^{2+} in 0.5–$5.0\,\mu g \cdot L^{-1}$ and the corresponding calibration plots (inset) of p(1,5-DAN)/SPEs. Electrolyte: acetate buffer (pH 4.5); deposition potential: -1.2 V; deposition time: 360 s.

work [28–31]. In the initiation step, radical cations were generated from monomer oxidation by electrons on the anode. In the next steps, the radicals were then coupled to form oligomers and so on. However, the carbon screen-printed electrode has lower electron conductivity than the other electrodes (such as Au, Pt, and glassy carbon), which is attributed to the polymeric binder in the carbon ink [32]. The decrease in the electron transfer rate for screen-printed electrodes helps the formation of p(1,5-DAN)-like nanowires at the low current density [33]. This film is suitable for the deposition of heavy metal ions in the preconcentration step.

3.3. The Application of p(1,5-DAN)/SPEs for Pb^{2+} Sensors. Figure 5 shows the SWASV of $4.5\,\mu g \cdot L^{-1}$ Pb^{2+} in acetate

TABLE 1: Summary of publications relevant to the electrochemical detection of Pb^{2+} using conducting polymers.

Electrode	Active layer	LOD ($\mu g \cdot L^{-1}$)	Linear range ($\mu g \cdot L^{-1}$)	Ref.
Glassy carbon	Poly(3,4-ethylenedioxythiophene)/black TiO_2 composites	0.15	8.28-256.93	[21]
Sputtered planar platinum	Poly(1,5-diaminonaphthalene)/graphene	0.02	0.2-700	[23]
Glassy carbon	Polyaniline	20.72	0-414.4	[34]
Glassy carbon	Overoxidized polypyrrole doped with 2(2-pyridylazo) chromotropic acid anion	10	0-200	[36]
Planar platinum	Interpenetrated multiwalled carbon nanotubes/poly (1,5-diaminonaphthalene)	2.1	4-150	[37]
Glassy carbon	Poly(1,2-diaminoanthraquinone)	0.58	0-120	[38]
Glassy carbon	Imidazole-functionalized polyaniline	20	2.07-2.07×10^5	[39]
Carbon paste		2	0.21-2.07×10^5	
Glassy carbon	Silver nanoparticles deposited on poly(1,8-diaminonaphthalene)	0.031	207.2-2,486	[40]
Glassy carbon	Polypyrrole-reduced graphene oxide nanocomposite hydrogels	0.062	0.1-93.2	[41]
Magnetic glassy carbon	Core-shell ferroferric oxide@polyaniline	0.006	0.02-2,072	[42]
Glassy carbon	Polyaniline-alanine-reduced graphene oxide	0.009	0.016-20.72	[43]
SPE	Graphene-polyaniline	0.1	1–300	[44]
SPE	Graphene/polyaniline/polystyrene	3.3	10–500	[45]
SPE	Poly(1,5-diaminonaphthalene)	0.30	0.5–5.0	This work

buffer (pH 4.5) at bare SPEs (curve (a)) and p(1,5-DAN)/SPEs (curve (b)). The current response on bare SPEs is very poor, with a dwarf peak. Under identical conditions, the p(1,5-DAN)-modified SPEs present significantly increased signals at -0.75 V.

The enhancement effects on the p(1,5-DAN)/SPEs are remarkably high in contrast to those on the bare SPEs. This result showed that p(1,5-DAN) was able to preconcentrate lead and was related to the amino and imine groups in the polymer chain. Besides, Wang et al. suggested that the conducting polymer has effectively prevented the adsorption of heavy metal ions on the microporous glassy carbon electrode [34]. So, almost all target ions are deposited on the electrode's surface, and the stripping voltammetry process is perfect.

3.4. Optimization of Conditions for Pb^{2+} Detection. In order to get the best of SWASV of the p(1,5-DAN)/SPEs toward Pb^{2+}, some of the key parameters were selected for optimized experiments. The effect of deposition potential and deposition time of Pb^{2+} detection in 0.1 M acetate buffer solution (pH 4.5) was investigated and is shown in Figure 6.

As shown in Figure 6(a), the stripping peak current of $4.5 \mu g \cdot L^{-1}$ Pb^{2+} after 360 s of deposition increased when the deposition potential decreased. The peak current quickly increased as the deposition potential decreased to -1.2 V. The deposition potential decreased from -1.2 and -1.5 V, and the peak current increased but slower. However, to avoid possible interference with other metals and damage to the working electrode, the potential at -1.2 V is chosen for continuous studies.

The effect of the deposition time for $45 \mu g \cdot L^{-1}$ Pb^{2+} detections on p(1,5-DAN)/SPEs was studied in the range from 180 to 480 s (Figure 6(b)). Under a fixed deposition potential at -1.2 V, the peak current increased steadily with increasing deposition time. A 360 s deposition time was selected as a compromise between high signal and reasonable assay time.

3.5. Calibration Plot. The square wave peak current (I_p) for Pb^{2+} detection in 0.1 M acetate buffer solution (pH 4.5) in the concentration range from $0.5 \mu g \cdot L^{-1}$ to $5.0 \mu g \cdot L^{-1}$ is shown in Figure 7. The peak current increases with an increase in the concentration of Pb^{2+} ions. The calibration curve (Figure 7, inset) was derived from the peak currents of SWASV curves that exhibit excellent linear dependence on the concentration of Pb^{2+} with a linearity regression equation $I_p (\mu A) = 0.506 \times C (\mu g \cdot L^{-1}) - 0.078$ ($R^2 = 0.9929$). The limit of detection (LOD) was calculated by using the formula LOD = $3.3 \times$ standard deviation of response/slope of the calibration curve [35]. The LOD obtained for the sensor was found to be $0.30 \mu g \cdot L^{-1}$.

In order to test the repeatability of sensors, the p(1,5-DAN)/SPEs were used for five measurements of $4.5 \mu g \cdot L^{-1}$ Pb^{2+} in acetate buffer solution. The relative standard deviation (% RSD, $n = 5$) of 3.1% was found. This result suggests that the poly(1,5-diaminonaphthalene)-modified screen-printed device exhibited good reproducibility and stability toward the Pb^{2+} ion sensing.

The analytical performance of p(1,5-DAN)/SPEs for Pb^{2+} was compared with other reported conducting polymers based on the literature, and results are summarized in Table 1. As can be seen, almost all conducting polymers are usually combined with inorganic nanomaterials for sensor sensitivity enhancement. Comparisons showed that the poly(1,5-diaminonaphthalene)-modified screen-printed device is a potential sensor for electroanalysis of Pb^{2+} with a low LOD value.

3.6. Interferences of Other Metallic Ions. The interferences of some metallic ions on the detection of Pb^{2+} was investigated

TABLE 2: Interferences of some metallic ions on the SWASV peak currents of $5.0\ \mu g \cdot L^{-1}\ Pb^{2+}$.

Interferent	Concentration ($\mu g \cdot L^{-1}$)	Peak current change (%)
Zn^{2+}	500	-0.4
Mn^{2+}	500	+0.9
Fe^{2+}	500	-2.6
Cu^{2+}	20	+4.5
Al^{3+}	500	-3.1
Hg^{2+}	8	+15.7

Electrolyte: acetate buffer (pH 4.5); deposition potential: -1.2 V; deposition time: 360 s; frequency: 50 Hz; amplitude: 50 mV; step potential: 5 mV.

TABLE 3: Determination of Pb^{2+} in different tap water samples (mean of three determinations).

Sample	Original ($\mu g \cdot L^{-1}$)	Add ($\mu g \cdot L^{-1}$)	Found ($\mu g \cdot L^{-1}$)	Recovery (%)
Tap water 1	Not detected	2.0	1.98	94.5
Tap water 2	Not detected	3.0	3.02	100.7
Tap water 3	Not detected	4.0	4.05	101.2

under the optimal experimental conditions discussed above. Table 2 suggests that some metallic ions, such as Zn^{2+}, Mn^{2+}, Fe^{2+}, and Al^{2+} (each 100-fold excess) and Cu^{2+} (4-fold excess), did not influence the SWASV peak currents of $5.0\ \mu g \cdot L^{-1}\ Pb^{2+}$ (the ratios for a ±5% peak current change). For the concentration of Hg^{2+} ($>8\ \mu g \cdot L^{-1}$), the anodic stripping peak currents of Pb^{2+} increase due to mercury ions that can be reduced and form a mercury film at the electrode surface.

3.7. Analysis of Lead Ions in Tap Water. The p(1,5-DAN)/SPEs were employed for the detection of Pb^{2+} in the tap water sample matrix. The 2 mL tap water sample was mixed well into a buffer solution (pH 4.5) by sodium acetate and acetic acid, then dropped onto the p(1,5-DAN)/SPEs using a micropipette. The various concentrations of Pb^{2+} were spiked in the sample matrix. The SWASV was recorded under the optimum conditions. As can be seen in Table 3, the recoveries of Pb^{2+} were obtained with the concentration found divided by the assigned concentration of Pb^{2+} in the sample matrix. It is shown that the p(1,5-DAN)/SPEs are promising for the determination of Pb^{2+} in the real sample.

4. Conclusions

This work describes the use of the integrated screen-printed electrodes for the voltammetric determination of Pb^{2+} based on the poly(1,5-diaminonaphthalene) conductive polymer. The advantages of screen-printed electrodes, such as mass production, reproducibility, and ease of the preparation process, combined with a conductive polymer p(1,5-DAN), presented the excellent effect as a very inexpensive portable heavy metal ion analyzer. The modified screen-printed electrodes were used for the sensitive determination of Pb^{2+} by anodic stripping voltammetry.

Data Availability

The data used to support the findings of this study are included in the article.

Conflicts of Interest

The authors declare that there is no conflict of interest regarding the publication of this paper.

Acknowledgments

References

[1] H. Needleman, "Lead poisoning," *Annual Review of Medicine*, vol. 55, no. 1, pp. 209–222, 2004.

[2] "Commission Regulation (EC) No 1881/2006 of 19 December 2006 setting maximum levels for certain contaminants in foodstuffs," 2006.

[3] WHO (WHO), "Guidelines for Drinking Water Quality," 2008.

[4] W. S. Zhong, T. Ren, and L. J. Zhao, "Determination of Pb (lead), Cd (cadmium), Cr (chromium), Cu (copper), and Ni (nickel) in Chinese tea with high-resolution continuum source graphite furnace atomic absorption spectrometry," *Journal of Food and Drug Analysis*, vol. 24, no. 1, pp. 46–55, 2016.

[5] H. P. Longerich, B. J. Fryer, and D. F. Strong, "Determination of lead isotope ratios by inductively coupled plasma-mass spectrometry (ICP-MS)," *Spectrochimica Acta Part B: Atomic Spectroscopy*, vol. 42, no. 1-2, pp. 39–48, 1987.

[6] M. Ali, T. R. Choudhury, B. Hossain, and M. P. Ali, "Determination of traces of molybdenum and lead in foods by X-ray fluorescence spectrometry," *SpringerPlus*, vol. 3, no. 1, 2014.

[7] J. Barek, A. G. Fogg, A. Muck, and J. Zima, "Polarography and voltammetry at mercury electrodes," *Critical Reviews in Analytical Chemistry*, vol. 31, no. 4, pp. 291–309, 2001.

[8] J. Wang, "Stripping analysis at bismuth electrodes: a review," *Electroanalysis*, vol. 17, no. 15-16, pp. 1341–1346, 2005.

[9] N. Cotolan, L. M. Mureşan, A. Salis, L. Barbu-Tudoran, and G. L. Turdean, "Electrochemical detection of lead ions with ordered mesoporous silica–modified glassy carbon electrodes," *Water, Air, & Soil Pollution*, vol. 231, no. 5, 2020.

[10] J. H. T. Luong, K. B. Male, and J. D. Glennon, "Boron-doped diamond electrode: synthesis, characterization, functionalization and analytical applications," *Analyst*, vol. 134, no. 10, pp. 1965–1979, 2009.

[11] A. K. Wanekaya, "Applications of nanoscale carbon-based materials in heavy metal sensing and detection," *Analyst*, vol. 136, no. 21, pp. 4383–4391, 2011.

[12] S. Arora, M. K. Punith Kumar, and C. Srivastava, "Graphene–ZnO nanocomposite sensor for lead-ion detection," *Philosophical Magazine Letters*, vol. 100, no. 11, pp. 533–541, 2020.

[13] K. Wu, S. Hu, J. Fei, and W. Bai, "Mercury-free simultaneous determination of cadmium and lead at a glassy carbon electrode modified with multi-wall carbon nanotubes," *Analytica Chimica Acta*, vol. 489, no. 2, pp. 215–221, 2003.

[14] T. M. Arantes, A. Sardinha, M. R. Baldan, F. H. Cristovan, and N. G. Ferreira, "Lead detection using micro/nanocrystalline boron-doped diamond by square-wave anodic stripping voltammetry," *Talanta*, vol. 128, pp. 132–140, 2014.

[15] V. Sethumadhavan, S. Rudd, E. Switalska, K. Zuber, P. Teasdale, and D. Evans, "Recent advances in ion sensing with conducting polymers," *BMC Materials*, vol. 1, no. 1, 2019.

[16] Z. Wang, E. Liu, D. Gu, and Y. Wang, "Glassy carbon electrode coated with polyaniline-functionalized carbon nanotubes for detection of trace lead in acetate solution," *Thin Solid Films*, vol. 519, no. 15, pp. 5280–5284, 2011.

[17] J. H. Santos, M. R. Smyth, and R. Blanc, "Mercury-free anodic stripping voltammetry of lead ions using a PVS-doped polyaniline modified glassy carbon electrode," *Analytical Communications*, vol. 35, no. 10, pp. 345–348, 1998.

[18] I. Adraoui, M. el?Rhazi, A. Amine, L. Idrissi, A. Curulli, and G. Palleschi, "Lead determination by anodic stripping voltammetry using ap-Phenylenediamine modified carbon paste electrode," *Electroanalysis*, vol. 17, no. 8, pp. 685–693, 2005.

[19] P. Manisankar, C. Vedhi, G. Selvanathan, and P. Arumugam, "Differential pulse stripping voltammetric determination of heavy metals simultaneously using new polymer modified glassy carbon electrodes," *Microchimica Acta*, vol. 163, no. 3-4, pp. 289–295, 2008.

[20] L. Oularbi, M. Turmine, and M. El Rhazi, "Electrochemical determination of traces lead ions using a new nanocomposite of polypyrrole/carbon nanofibers," *Journal of Solid State Electrochemistry*, vol. 21, no. 11, pp. 3289–3300, 2017.

[21] Z. Yu, R. Jamal, R. Zhang et al., "PEDOT-type conducting polymers/black TiO_2 Composites for electrochemical determination of Cd^{2+} and Pb^{2+}," *Journal of The Electrochemical Society*, vol. 167, no. 6, article 067514, 2020.

[22] S. Majid, M. E. Rhazi, A. Amine, A. Curulli, and G. Palleschi, "Carbon paste electrode bulk-modified with the conducting polymer poly(1,8-diaminonaphthalene): application to lead determination," *Microchimica Acta*, vol. 143, no. 2-3, pp. 195–204, 2003.

[23] T. D. Nguyen, T. T. H. Dang, H. Thai et al., "One-step electrosynthesis of poly(1,5-diaminonaphthalene)/graphene nanocomposite as platform for lead detection in water," *Electroanalysis*, vol. 28, no. 8, pp. 1907–1913, 2016.

[24] X.-G. Li, J.-L. Zhang, and M.-R. Huang, "Chemical response of nanocomposite membranes of electroactive polydiaminonaphthalene nanoparticles to heavy metal ions," *The Journal of Physical Chemistry C*, vol. 118, no. 22, pp. 11990–11999, 2014.

[25] H. L. Nguyen, H. H. Cao, D. T. Nguyen, and V.-A. Nguyen, "Sodium dodecyl sulfate doped polyaniline for enhancing the electrochemical sensitivity of mercury ions," *Electroanalysis*, vol. 29, no. 2, pp. 595–601, 2017.

[26] X. S. Zhu, C. Gao, J.-W. Choi, P. L. Bishop, and C. H. Ahn, "On-chip generated mercury microelectrode for heavy metal ion detection," *Lab on a Chip*, vol. 5, no. 2, pp. 212–217, 2005.

[27] S. K. Yadav, B. Agrawal, and R. N. Goyal, "AuNPs-poly-DAN modified pyrolytic graphite sensor for the determination of cefpodoxime proxetil in biological fluids," *Talanta*, vol. 108, pp. 30–37, 2013.

[28] M. C. Pham, M. Oulahyne, M. Mostefai, and M. M. Chehimi, "Multiple internal reflection FT-IR spectroscopy (MIRFTIRS) study of the electrochemical synthesis and redox process of poly (1,5-diaminonaphthalene)," *Synthetic Metals*, vol. 93, no. 2, pp. 89–96, 1998.

[29] V. A. Nguyen, H. L. Nguyen, D. T. Nguyen, Q. P. Do, and L. D. Tran, "Electrosynthesized poly(1,5-diaminonaphthalene)/polypyrrole nanowires bilayer as an immunosensor platform for breast cancer biomarker CA 15-3," *Current Applied Physics*, vol. 17, no. 11, pp. 1422–1429, 2017.

[30] K. Jackowska, J. Bukowska, and M. Jamkowski, "Synthesis, electroactivity and molecular structure of poly(1,5-diaminonaphthalene)," *Journal of Electroanalytical Chemistry*, vol. 388, no. 1-2, pp. 101–108, 1995.

[31] M. C. Pham, M. Oulahyane, M. Mostefai, and P. C. Lacaze, "Electrosynthesis and in situ multiple internal reflection FTIR spectroscopic (MIRFTIRS) study of poly(1,5-diaminonaphthalene)," *Synthetic Metals*, vol. 84, no. 1-3, pp. 411-412, 1997.

[32] K. Grennan, A. J. Killard, and M. R. Smyth, "Physical characterizations of a screen-printed electrode for use in an amperometric biosensor system," *Electroanalysis*, vol. 13, no. 8-9, pp. 745–750, 2001.

[33] L. Liang, J. Liu, C. F. Windisch, Jr, G. J. Exarhos, and Y. Lin, "Direct assembly of large arrays of oriented conducting polymer nanowires," *Angewandte Chemie International Edition*, vol. 41, no. 19, pp. 3665–3668, 2002.

[34] Z. Wang, E. Liu, and X. Zhao, "Glassy carbon electrode modified by conductive polyaniline coating for determination of trace lead and cadmium ions in acetate buffer solution," *Thin Solid Films*, vol. 519, no. 15, pp. 5285–5289, 2011.

[35] A. Shrivastava and V. B. Gupta, "Methods for the determination of limit of detection and limit of quantitation of the analytical methods," *Chronicles of Young Scientists*, vol. 2, no. 1, pp. 21–25, 2011.

[36] A. Wanekaya and O. A. Sadik, "Electrochemical detection of lead using overoxidized polypyrrole films," *Journal of Electroanalytical Chemistry*, vol. 537, no. 1-2, pp. 135–143, 2002.

[37] H. D. Vu, L.-H. Nguyen, T. D. Nguyen, H. B. Nguyen, T. L. Nguyen, and D. L. Tran, "Anodic stripping voltammetric determination of Cd^{2+} and Pb^{2+} using interpenetrated MWCNT/P1,5-DAN as an enhanced sensing interface," *Ionics*, vol. 21, no. 2, pp. 571–578, 2015.

[38] K. M. Hassan, S. E. Gaber, M. F. Altahan, and M. A. Azzem, "Novel sensor based on poly (1,2-diaminoanthraquinone) for individual and simultaneous anodic stripping voltammetry of Cd^{2+}, Pb^{2+}, Cu^{2+} and Hg^{2+}," *Electroanalysis*, vol. 30, no. 6, pp. 1155–1162, 2018.

[39] P. Kumar, A. Joseph, P. C. Ramamurthy, and S. Subramanian, "Lead ion sensor with electrodes modified by imidazole-functionalized polyaniline," *Microchimica Acta*, vol. 177, no. 3-4, pp. 317–323, 2012.

[40] K. M. Hassan, G. M. Elhaddad, and M. AbdelAzzem, "Voltammetric determination of cadmium(II), lead(II) and copper(II) with a glassy carbon electrode modified with silver nanoparticles deposited on poly(1,8-diaminonaphthalene)," *Microchimica Acta*, vol. 186, no. 7, 2019.

[41] V. Suvina, S. M. Krishna, D. H. Nagaraju, J. S. Melo, and R. G. Balakrishna, "Polypyrrole-reduced graphene oxide nanocomposite hydrogels: a promising electrode material for the simultaneous detection of multiple heavy metal ions," *Materials Letters*, vol. 232, pp. 209–212, 2018.

[42] Y. Kong, T. Wu, D. Wu et al., "An electrochemical sensor based on Fe3O4@PANI nanocomposites for sensitive detection of Pb^{2+} and Cd^{2+}," *Analytical Methods*, vol. 10, no. 39, pp. 4784–4792, 2018.

[43] M. Akhtar, A. Tahir, S. Zulfiqar et al., "Ternary hybrid of polyaniline-alanine-reduced graphene oxide for electrochemical sensing of heavy metal ions," *Synthetic Metals*, vol. 265, article 116410, 2020.

[44] N. Ruecha, N. Rodthongkum, D. M. Cate, J. Volckens, O. Chailapakul, and C. S. Henry, "Sensitive electrochemical sensor using a graphene-polyaniline nanocomposite for simultaneous detection of Zn(II), Cd(II), and Pb(II)," *Analytica Chimica Acta*, vol. 874, pp. 40–48, 2015.

[45] N. Promphet, P. Rattanarat, R. Rangkupan, O. Chailapakul, and N. Rodthongkum, "An electrochemical sensor based on graphene/polyaniline/polystyrene nanoporous fibers modified electrode for simultaneous determination of lead and cadmium," *Sensors and Actuators B: Chemical*, vol. 207, pp. 526–534, 2015.

WILEY | Hindawi

Research Article

Cerium Oxide/Polypyrrole Nanocomposite as the Matrix for Cholesterol Biosensor

Ta Thi Nhat Anh [ID],[1,2] **Vu Van Thu** [ID],[3] **Hai-Son Dang,**[4] **Vuong-Hung Pham** [ID],[1] **and Phuong Dinh Tam** [ID][4]

[1]*Advanced Institute for Science and Technology, Hanoi University of Science and Technology, Vietnam*
[2]*Vinh Phuc Technology Economic College, No. 10 Hung Vuong Road, Vinhyen, Vinh Phuc, Vietnam*
[3]*Faculty of Occupational Safety and Health, Trade Union University, Hanoi, Vietnam*
[4]*Faculty of Material Science and Engineering, Phenikaa University, Hanoi 12116, Vietnam*

Correspondence should be addressed to Vuong-Hung Pham; vuong.phamhung@hust.edu.vn
and Phuong Dinh Tam; tam.phuongdinh@phenikaa-uni.edu.vn

A nanocomposite comprising cerium oxide nanoparticles (CeO_2 NPs) and polypyrrole (PPy) was fabricated onto a microelectrode for cholesterol sensing application. The cholesterol oxidase (ChOx) was immobilized on the CeO_2 NPs/PPy/electrode by the physical adsorption route. The structure and morphology of the CeO_2 NPs/PPy nanocomposite were characterized by X-ray diffraction, field emission scanning electron microscopy, and energy dispersive X-ray spectroscopy. Results showed that the ChOx/CeO_2 NPs/PPy/electrode was linearly related with cholesterol in the range of 50 to 500 mg/dL. The sensitivity of ChOx/CeO_2 NPs/PPy/electrode was 5.7×10^{-6} mA/mg·dL^{-1}. The optimal parameters, including pH value and temperature, and selectivity, storage stability, and reproducibility of ChOx/CeO_2 NPs/PPy/electrode were investigated.

1. Introduction

Cholesterol is an important component of cell membranes. Normally, the total cholesterol amount in the human blood at less than 200 mg/dL represents the desirable level, from 200 to 239 mg/dL is the borderline high for heart disease, and above 240 mg/dL corresponds to high blood cholesterol [1]. High cholesterol levels in the human blood are usually associated to heart diseases, diabetes, nephrosis, and obstructive jaundice [2]. Thus, cholesterol level estimation is extremely important in clinical diagnosis. The different approaches, including high-performance liquid chromatography [3–6], near-infrared (IR) spectra [7–9], and colorimetric assay [10–12], have been used for cholesterol level detection. However, the abovementioned approaches are expensive and time consuming and require large amounts of serum samples [13, 14]. Therefore, a rapid, robust, and sensitive cholesterol detection method should be developed [15].

Electrochemical biosensors, owing to their advantages of simplicity, selectivity, rapid response, stability, low cost, and ease of fabrication [15–20], have been recently studied to detect cholesterol levels. Tiwari and Gong [20] reported a novel chitosan (CHIT)/SiO_2/multiwalled carbon nanotube (MWCNT)/electrode-based cholesterol biosensor. They established the linear relationship between oxidation current response and cholesterol concentrations to be in the range of 5.0–5000 μg/mL, a response time of 5 s, and a sensitivity of 3.4nA/mg dL^{-1}. Wisitsoraat et al. [21] developed a new cholesterol biosensor by using carbon nanotubes (CNT) directly growth on a glass-based chip via the low-temperature chemical vapor deposition process. They determined the linear detection range to be between 50 and 400mg/dL with a sensitivity of 0.0512nA/mg·dL^{-1}. Khan et al. [22] studied a cholesterol biosensor by using nano-ZnO–CHIT as the sensing element. They found that the granular porous morphology of nano-ZnO–CHIT could provide an even better
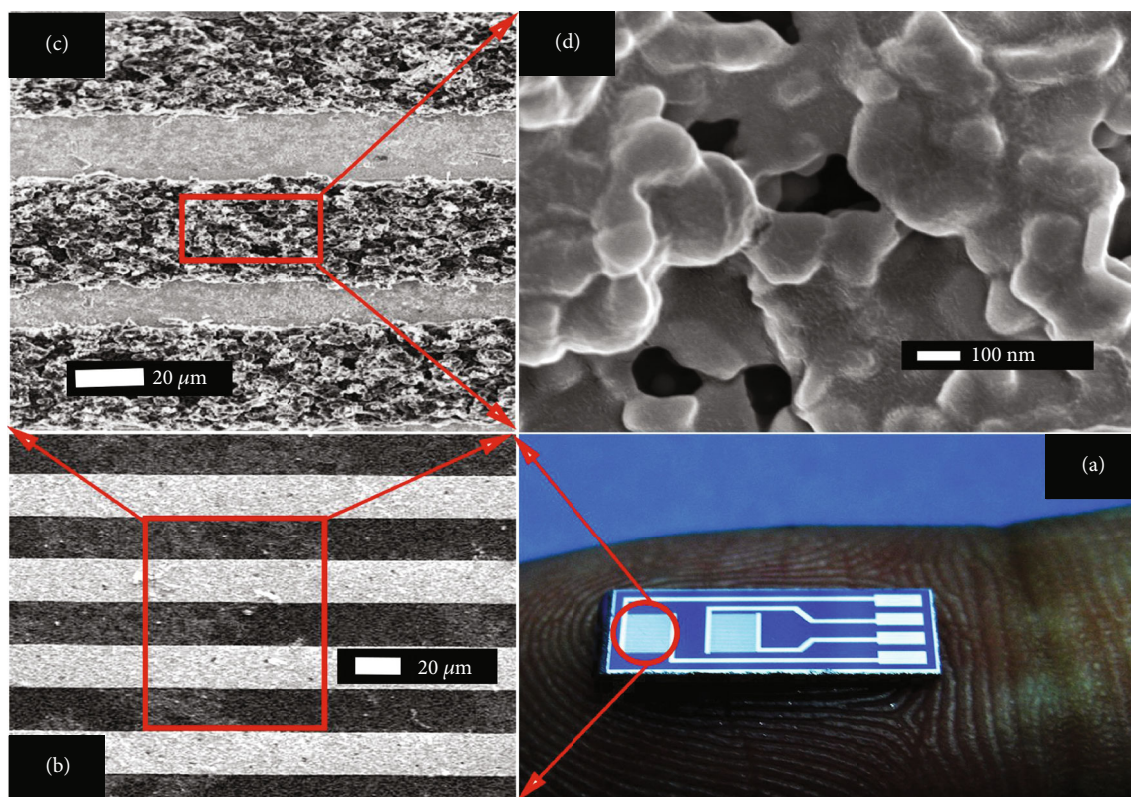
SCHEME 1: Schematic of cholesterol biosensor fabrication, (a) microelectrode, and (b)–(d) magnification of CeO$_2$ NPs/PPy nanocomposite-modified electrode.

biocompatible environment for the enzymes. The developed sensor presented a linearity from 5 to 300mg·dL^{-1} and a shelf life of 85 days. Ansari et al. [23] studied the CHIT–tin oxide (SnO$_2$) nano-biocomposite film for cholesterol biosensor development. They showed that ChOx/CHIT-SnO$_2$/ITO (indium–tin–oxide) was more stable than the ChOx/CHI-T/ITO bioelectrode, and it presented a high sensitivity of 34.7mA/mgdL^{-1}cm^2, a linear response in the range of 10–400mg/dL, and a low detection limit of 5mg/dL.

Polypyrrole (PPy), a functional conducting polymer material, is usually considered to be a p-type material with good thermal and high environmental stability, low oxidation potential, and high conductivity [24]. In recent years, PPy-based nanocomposites with different nanomaterials, such as CNT [25], metal oxide [26], dodecylbenzene sulfonate (DBS) [27], have attracted wide attention for biosensor development owing to their large specific surface areas, high conductivity, and biocompatibility. Singh et al. [25] studied a biosensor by using PPy/MWCNT as the mediator for cholesterol sensing. The PPy and carboxy-functionalized MWCNT were electrochemicaly synthesized onto the ITO electrode by using p-toluene sulfonic acid (PTS). Moreover, ChOx and cholesterol esterase (ChEt) were immobilized onto the PPy-MWCNT/ITO electrode by using N-ethyl-N-(3-dimethylaminopropyl) carbodiimide and N-hydroxy succinimide chemistry. The ChEt–ChOx/PPy–MWCNT/PTS/ITO electrode presented a rapid response time of approximately 9 s with a detection limit of 0.04mM/L. They also demonstrated that the developed cholesterol biosensor could be easily fabricated, had a rapid response time, and was useful in blood serum sampling. A novel amperometric biosensor based on a conducting polymer and DBS-modified electrode was successfully developed by Ozer et al. [27]. ChOx was physically entrapped onto the PPy–DBS film surface; then, the cholesterol concentration was determined by performing an electrochemical detection of the H$_2$O$_2$ generated in the enzymatic reaction of cholesterol. Their results showed that 90.0% of the response current of the cholesterol biosensor could be retained after 30 activity assays, and the minimum detectable concentration of 10nM was also determined. Wang et al. [28] synthesized the CeO$_2$/PPy composite for electrochemical sensor application to detect sodium nitrite. The CeO$_2$/PPy composite was prepared by in situ compounding and coated on a glassy carbon electrode to obtain the electrochemical sensor. They showed the anode peak current response was proportional to the sodium nitrite concentration in the range 0.125–22.5mmol/L, and the detection limit was 0.08μmol/L. Nguyet et al. [29] reported a DNA sensor based on the CeO$_2$/PPy nanocomposite for Salmonella detection. In situ chemical oxidative polymerization was used to prepare the core–shell CeO$_2$-NR@PPy nanocomposite, which provided a suitable platform for electrochemical DNA biosensor fabrication. The sDNA/CeO$_2$NRs@PPy/electrode response under optimal conditions presented a linearity between 0.01 and 0.4nM with a sensitivity of 593.7Ω•nM^{-1}•cm^{-2}.

(a)

(b)

(c)
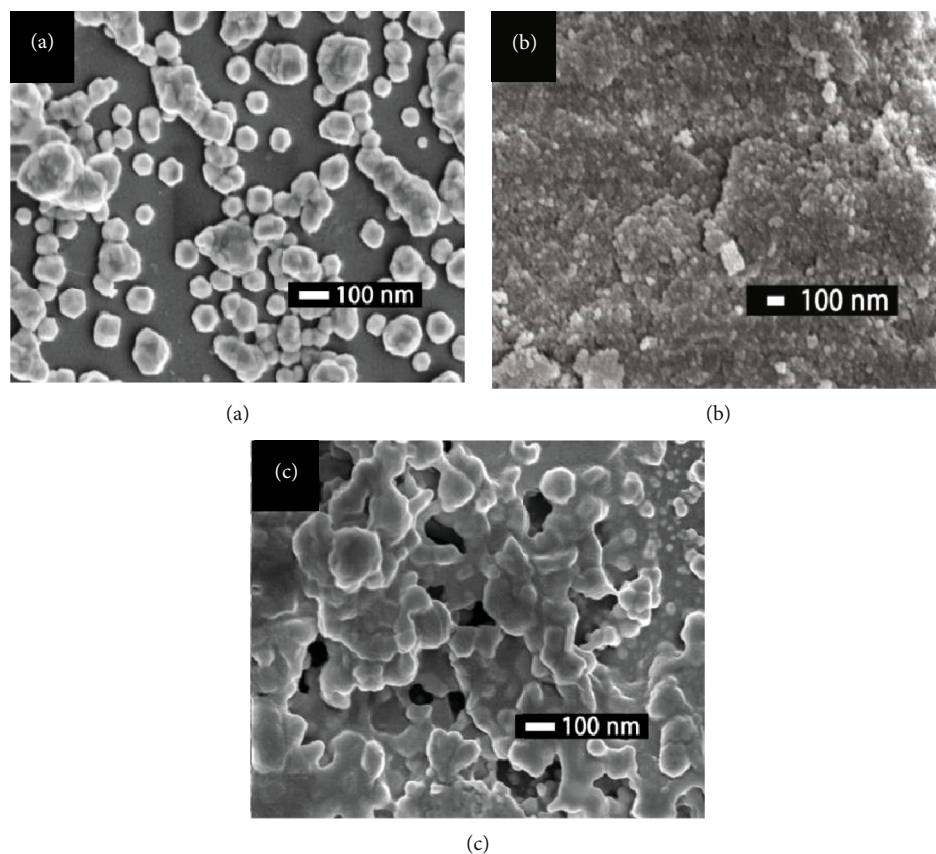
FIGURE 1: FE-SEM images of (a) pristine CeO$_2$ NPs, (b) pure PPy, and (c) CeO$_2$ NPs/PPy nanocomposite.

(a)

(b)
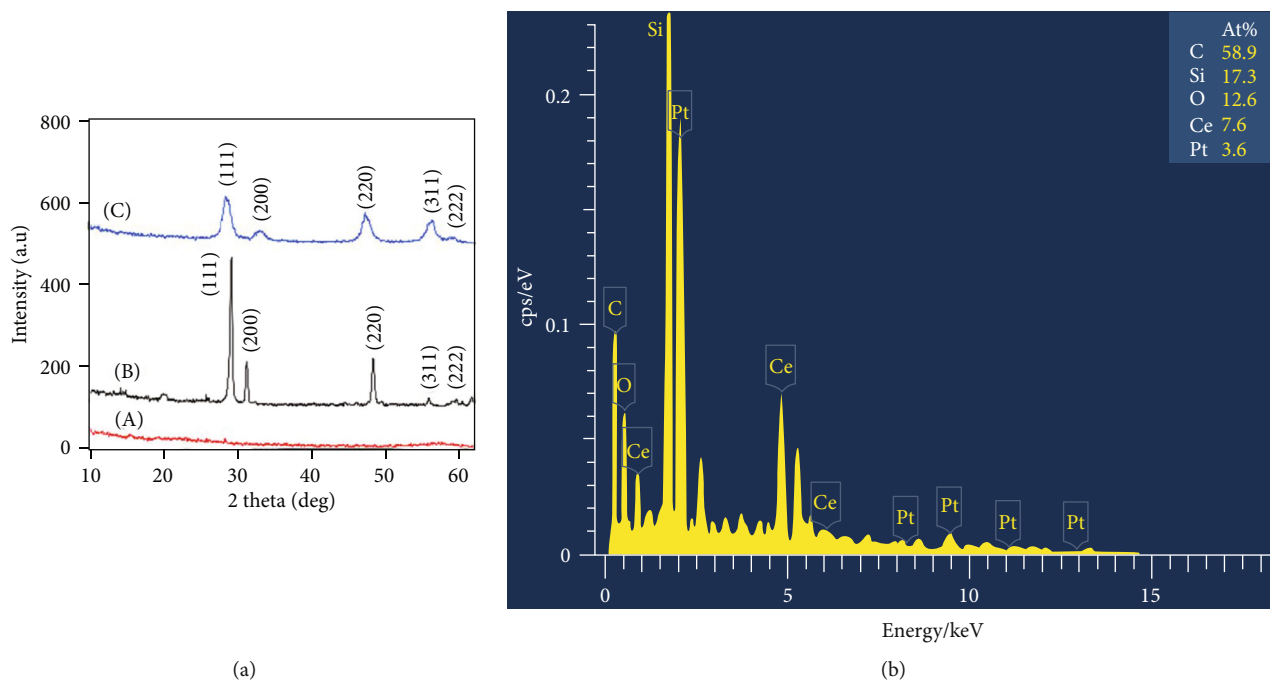
FIGURE 2: (a) XRD patterns of (A) pure PPy, (B) pristine CeO$_2$ NPs, and (C) CeO$_2$ NPs/PPy nanocomposite and (b) EDS of CeO$_2$ NPs/PPy nanocomposite.

CeO$_2$/PPy material-based biosensors have been widely studied for various biosensor applications. However, the reports on cholesterol biosensors, which use CeO$_2$/PPy nanomaterials as mediators, are limited. To the best of the author's knowledge, CeO$_2$ NPs/PPy nanocomposite based-biosensors have been rarely used in cholesterol detection.

In this study, we developed a cholesterol biosensor by using a CeO$_2$ NPs/PPy nanocomposite as the mediator to immobilize ChOx on the electrode surface without using an intermediate linker. The results showed improvements in the performance of cholesterol sensing, which may be due to the synergic effect of PPy and CeO$_2$ NPs. The influencing factors, including pH value and temperature, and the selectivity, storage stability, and reproducibility of ChOx/CeO$_2$ NPs/PPy/electrode were highlighted in this work.

2. Experimental

2.1. Chemical Reagents. ChOx was procured from Sigma-Aldrich. The potassium hexacyanoferrate (III) (K$_3$[Fe(CN)$_6$]), potassium hexacyanoferrate (II) (K$_4$Fe(CN)$_6$]), and phosphate buffer saline (PBS) were purchased from Beijing Chemical Reagent (China). Cerium III nitrate hexahydrate Ce(NO$_3$)$_3$.6H$_2$O (99.999%), CH$_3$COONH$_4$ (99.999%), cholesterol (95%), and KCl purity $\geq$ 99% were purchased from Sigma-Aldrich. All solutions were prepared with ultrapure water (18.2 MΩ·cm) from a Millipore Milli-Q system.

2.2. CeO$_2$ NPs/PPy Nanocomposite Synthesis. In this work, the microelectrode was used as a working electrode for cholesterol biosensor preparation. The sample was fabricated by sputtering 20 nm of Cr and 200 nm of Au on an approximately 100 nm thick silicon dioxide layer that was thermally grown on top of a silicon wafer. A saturated Ag/AgCl electrode was used as the reference electrode. A platinum plate was used as the counter-electrode. Before the electrode was modified, its surface was cleaned with KCr$_2$O$_7$ in 98% H$_2$SO$_4$. Then, the cleaned electrodes were treated via the cyclic voltammetry (CV) technique with a potential range from −0.5 to 2.1 V using 0.5 M H$_2$SO$_4$ as the electrolytes, rinsed with distilled H$_2$O until the pH of the solution was neutral, and dried under nitrogen stream. Subsequently, the CeO$_2$ NPs were electrochemically synthesized in a conventional three-electrode cell via CV in the range from −0.6 to 1.8 V with a scanning rate of 100-500 mV/s at room temperature in the electrolytic solution. The solution contained mixtures of 0.001-0.02 M of Ce(NO$_3$)$_3$.6H$_2$O, 0.01 M of KCl, and 0.02 M CH$_3$COONH$_4$. Finally, the PPy was electrochemically synthesized by galvanostatic polarization using an aqueous oxalic acid solution with 0.1 M pyrrole monomer for 240 seconds at 1 mA/cm^2. After the electrochemical deposition, the CeO$_2$ NPs/PPy-modified electrode was washed with ethanol and distilled water to remove impurities and then dried at room temperature. The schematic of the cholesterol biosensor fabrication is shown in Scheme 1.
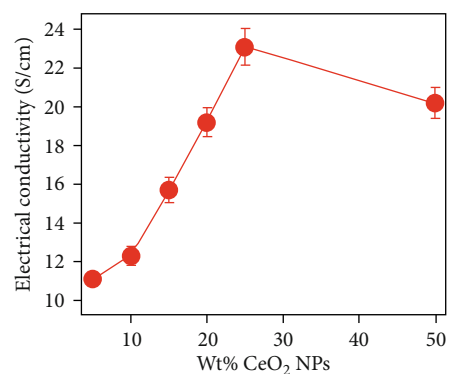
FIGURE 3: Electrical conductivity of CeO$_2$ NPs/PPy nanocomposite with different wt% of CeO$_2$ NPs.

2.3. Preparation of ChOx/CeO$_2$ NPs/PPy/Electrode. For the ChOx immobilization, the CeO$_2$ NPs/PPy-modified electrode was immersed in an immobilization solution (ChOx 1.0 mg/mL in 0.1 M PBS) for 12 h to enable the binding of ChOx on the electrode surface through physical adsorption. Then, the ChOx/CeO$_2$ NPs/PPy/electrode was further rinsed with DI water for several times to remove the unbound ChOx. A total of 5 μL of Nafion solution was dropped onto the electrode surface to prevent possible enzyme leakage. The ChOx/CeO$_2$ NPs/PPy/electrodes were stored in PBS at 4°C.

2.4. Electrochemical Measurements for ChOx/CeO$_2$ NPs/PPy/Electrode. The electrochemical measurements were performed using an IM6 impedance analyzer with the IM6-THALES software in PBS solutions containing Fe(CN)$_6^{3/4-}$ as a redox probe. The ChOx/CeO$_2$ NPs/PPy/electrode was connected to the test and sense probes, and the Pt electrode was connected to the counter-electrode of the IM6 impedance analyzer. The reference electrode was an Ag/AgCl electrode. The CV plots were recorded, and the difference in oxidation peak current density was considered the signal produced by ChOx-catalyzed cholesterol oxidation.

3. Results and Discussion

3.1. Structural Characterization. The morphological of (a) pristine CeO$_2$ NPs, (b) pure PPy, and (c) CeO$_2$ NPs/PPy nanocomposite was characterized through field emission scanning electron microscopy (FE-SEM) (Figure 1). Figure 1(a) indicates the morphology of the pristine CeO$_2$ NPs, which are synthesized in solution contained mixtures of 0.015 M of Ce(NO$_3$)$_3$.6H$_2$O, 0.01 M of KCl, and 0.02 M CH$_3$COONH$_4$ via CV in the range from −0.6 to 1.8 V. It can be seen that the morphology is uniformly distributed, with a diameter of approximately 80–100 nm. The morphology of the pure PPy with cauliflower-like structure is presented in Figure 1(b). Figure 1(c) shows FE-SEM of the CeO$_2$-NPs/PPy nanocomposite with a slight agglomeration and a diameter of approximately 100–120 nm, which is electrochemically synthesized by galvanostatic polarization using
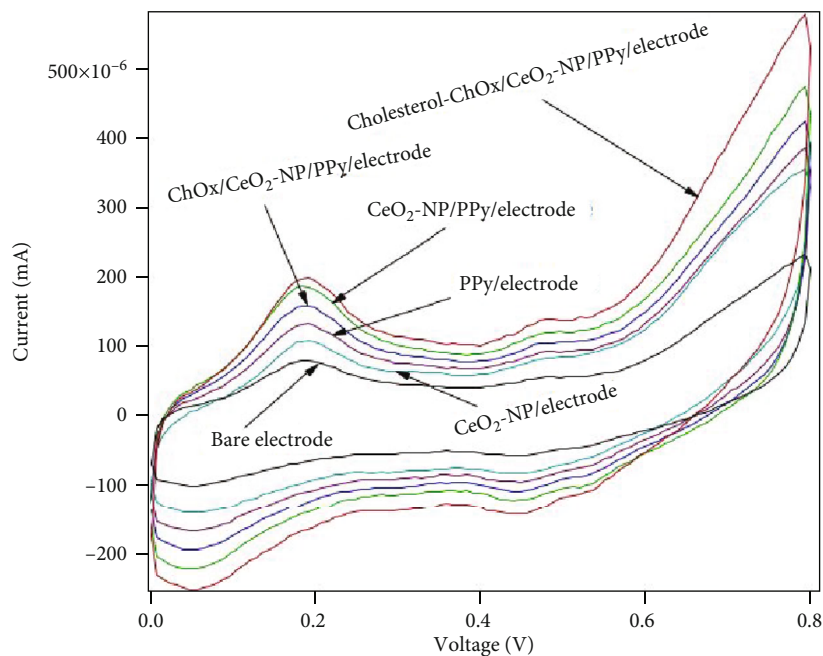
Figure 4: CV of bare electrode, CeO_2-NPs/electrode, PPy/electrode, CeO_2 NPs/PPy/electrode, ChOx/CeO_2 NPs/PPy/electrode, and cholesterol-ChOx/CeO_2 NPs/PPy/electrode in PBS solution containing $Fe(CN)_6^{3-/4-}$.

(a)

(b)
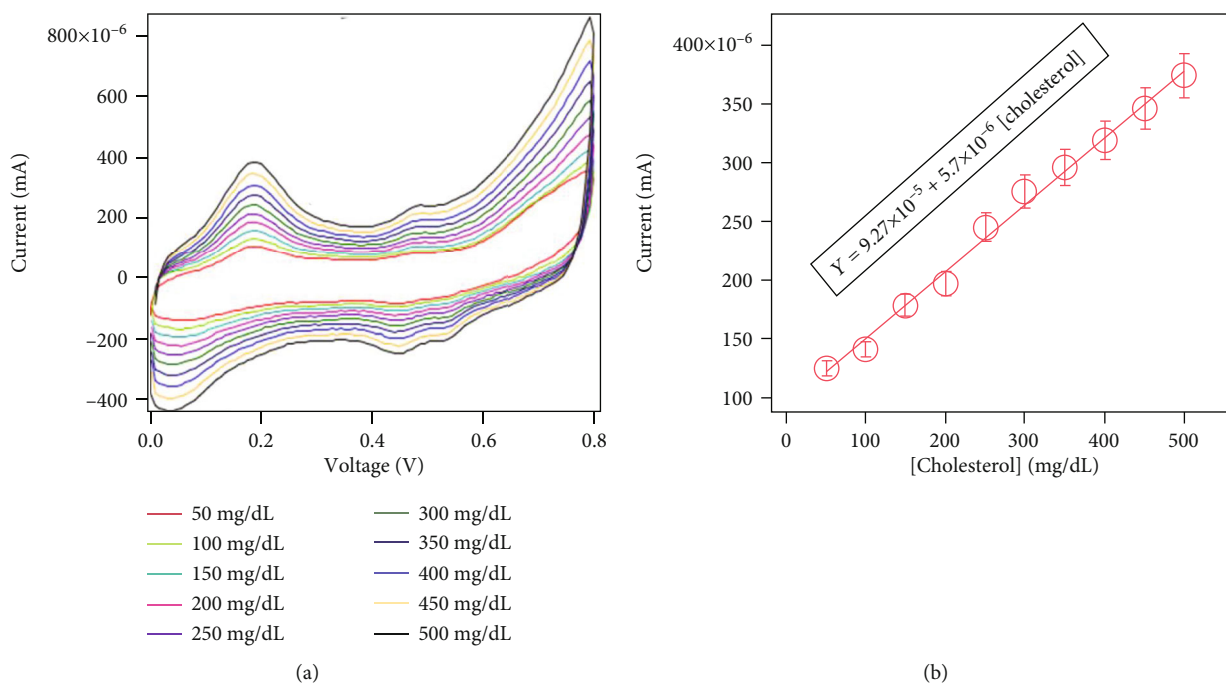
Figure 5: (a) CV with varying cholesterol concentrations from 50 to 500 mg/dL on ChOx/CeO_2 NPs/PPy/electrode in PBS solution containing $Fe(CN)_6^{3-/4-}$ and (b) electrode response as a function of cholesterol concentration.

an aqueous oxalic acid solution with 0.1 M pyrrole monomer for 240 seconds at 1 mA/cm².

The X-ray diffraction (XRD) patterns of the (a) pure PPy, (b) pristine CeO_2 NPs, and (c) CeO_2 NPs/PPy nanocomposite are shown in Figure 2(a). As illustrated in Figure 2(a), (A), the XRD pattern of the pure PPy is amorphous, as no peaks can be defined in its XRD pat-

tern. The diffraction peaks found at 28.6°, 33.1°, 47.6°, 56.5°, and 59.1° correspond to the (111), (200), (220), (311), and (222) planes with a cubic fluorite structure of the pristine CeO_2 NPs, as shown in Figure 2(a), (B). These peaks were indexed using JCPD card no. 34-0394. The XRD pattern of the CeO_2 NPs/PPy nanocomposite is illustrated in Figure 2(a), (C). The profile of the sample shown

Ref 21	Ref 22	Ref 23	Ref 24	Ref 33	This work
3.40E-06	5.12E-08	0.141	0.03447	0.0013	5.70E-06

(a)

Ref 21	Ref 22	This work
3.40E-06	5.12E-08	5.70E-06

(b)

Ref 21	Ref 22	Ref 23	Ref 24	Ref 33	This work
24	4	12	6	12	13
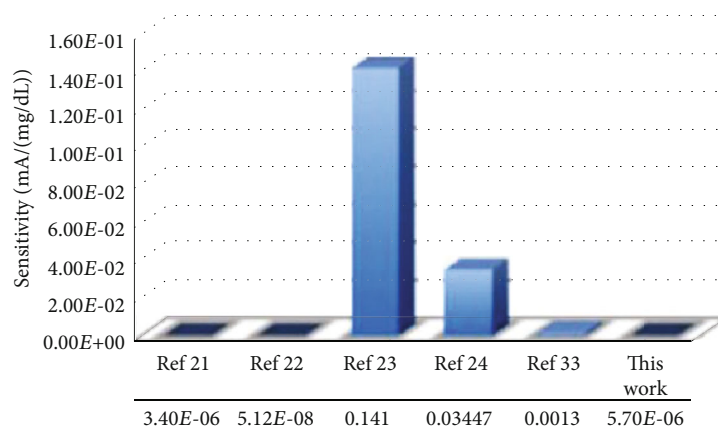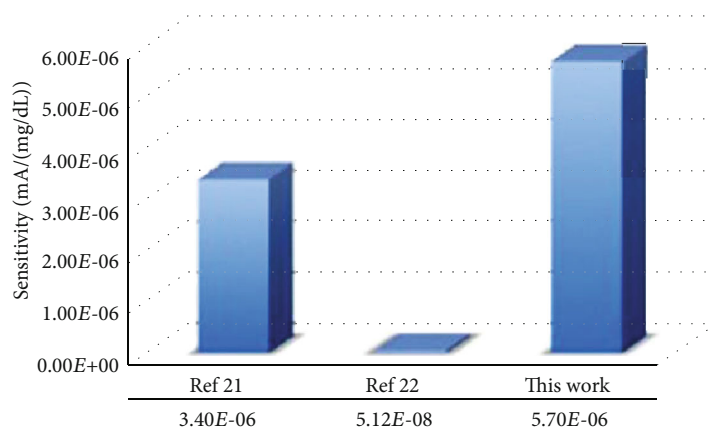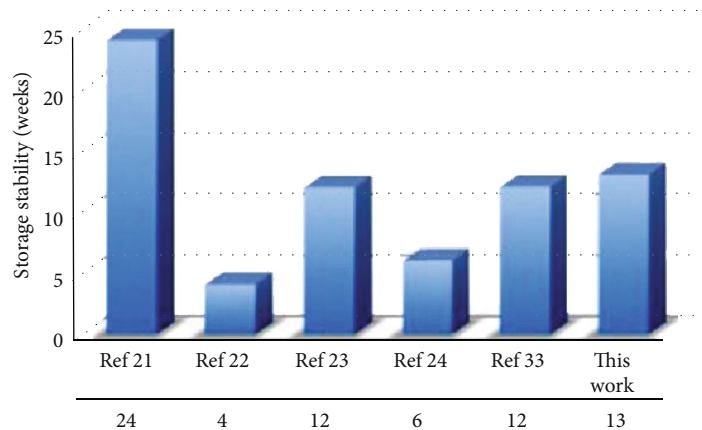
(c)

Figure 6: Continued.
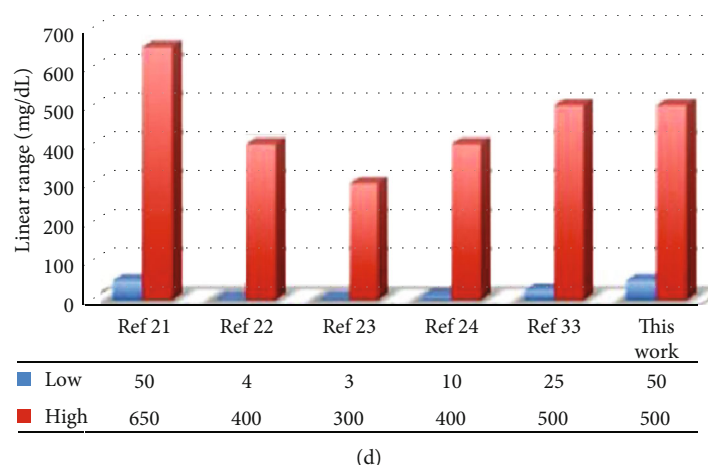
FIGURE 6: Comparative performance of different cholesterol biosensors: (a, b) sensitivity, (c) storage stability, and (d) linear range of cholesterol biosensor.
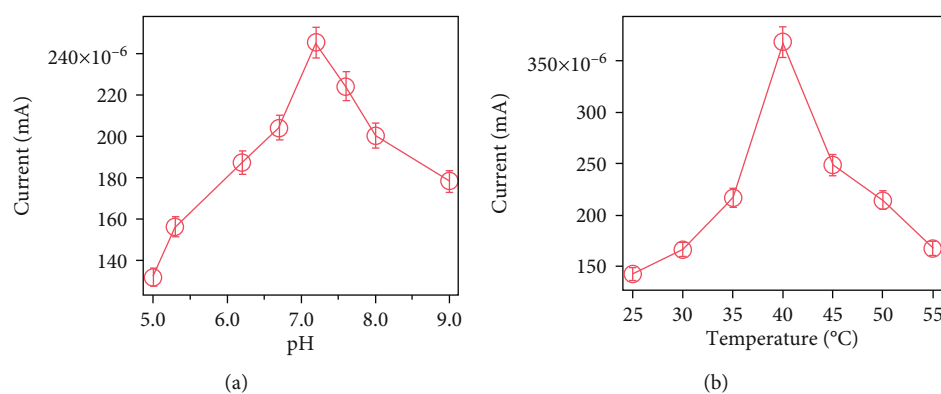
FIGURE 7: Effect of (a) pH and (b) temperature on the response of ChOx/CeO₂ NPs/PPy electrode with 200 mg/dL cholesterol.

in the figure is similar to that of the pristine CeO_2 NPs. The obtained results indicate that the crystal structure of the CeO_2 NPs was unmodified by pure PPy. However, when PPy was used to modify the CeO_2 NPs, the diffraction peak intensity of the sample was reduced with respect to that of the pristine CeO_2 NPs.

Figure 2(b) shows the energy dispersive X-ray spectroscopy (EDS) of the CeO_2 NPs/PPy nanocomposite. As shown in Figure 2(b), the presence of Ce and O was associated with the CeO_2 NPs. The carbon elements were related to the PPy. No contaminating elements could be found in the CeO_2 NPs/PPy during sample preparation, as no other peaks were detected except for the Si and Pt peaks originating from the substrate.

3.2. Electrical Conductivity Characterization of the CeO_2 NPs/PPy Nanocomposite.
The electrical conductivity of the CeO_2 NPs/PPy nanocomposite as a function of the CeO_2 concentration at room temperature is shown in Figure 3. The pure PPy electrical conductivity was obtained at approximately 11.3 S/cm. The conductivity increased to 23.1 S/cm when the CeO_2 NP amount of up to 25 wt.% was added; then, it decreased at the higher CeO_2 NP concentration. This result

is the same as the result obtained by Seema and Prasad [30], who determined that electrical conductivity was due to the excessive formation of charge carriers. Here, the decrease in conductivity may be due to the relatively large dimension of the CeO_2 NPs, which hinders the hopping of the charge carrier.

3.3. Electrochemical Characterization of Cholesterol Biosensor.
CV is a powerful tool for evaluating the interfacial properties of biosensors. Figure 4 shows the CV results of the cholesterol biosensor in the PBS solution (pH 7.4) containing the $[Fe(CN)_6]^{3-/4-}$ mediator within the range of 0.0–0.8 V and a scan rate of 100 V/s. The oxidation current peaks in the figure are 78.6×10^{-6}, 107×10^{-6}, and 131×10^{-6} mA for the bare electrode, CeO_2 NPs/electrode, and PPy/electrode, respectively. The results pertaining to the increasing oxidation current can be explained by the increasing electroactive electrode surface, which has led to the increasing electrochemical response. The oxidation current peak continuously further increased to 185×10^{-6} mA when the CeO_2 NPs/PPy nanocomposite-modified electrode facilitated the electron transfer of the redox probe $[Fe(CN)_6]^{3-/4-}$ between the electrolyte solution and the electrode. A decrease
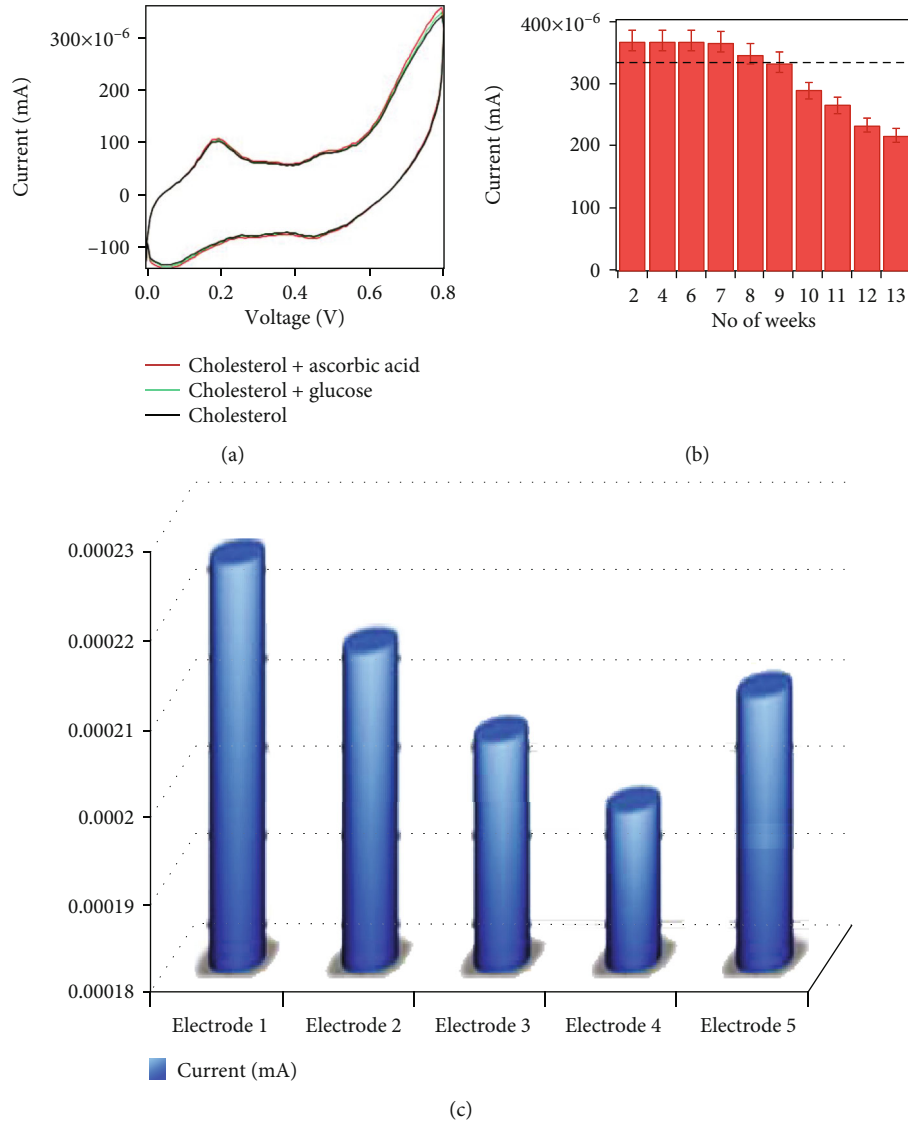
FIGURE 8: Results of (a) selectivity and (b) storage stability and (c) reproducibility of ChOx/CeO$_2$ NPs/PPy/electrode measured at 100 mV/s scan rates in the presence of 200 mg/dL cholesterol concentration.

in oxidation current peak was observed at 158×10^{-6} mA after ChOx was attached onto the CeO$_2$ NPs/PPy/electrode surface, which formed a thick film. The electron transfer was inhibited due to the insulating nature of the bulky protein molecules. The oxidation current was significantly enhanced at 198×10^{-6} mA for the ChOx/CeO$_2$ NPs/PPy/electrode in the presence of 200 mg/dL cholesterol in the PBS buffer. This finding may be explained as follows:

$$\text{Cholesterol} + \text{O}_2\,(\text{ChOx}) > \text{Cholestenone} + \text{H}_2\text{O}_2, \quad (1)$$

$$\text{H}_2\text{O}_2 > \frac{1}{2\text{O}_2} + \text{H}_2\text{O} + 2\text{e}^-. \quad (2)$$
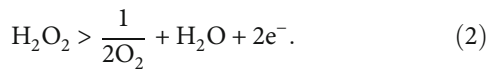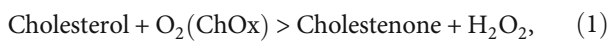
In reaction (1), cholesterol was first oxidized by oxygen to form cholestenone and H$_2$O$_2$ in the presence of ChOx. Then, H$_2$O$_2$ was reduced at the electrode surface to produce elec-

trons [31]. The CeO$_2$ NPs/PPy nanocomposite transferred the electrons to the electrode via probe indicator conversion, resulting in an increased oxidation current peak. This oxidation current peak response is directly proportional to the added cholesterol concentration, as illustrated in Figure 5.

As shown in Figure 5(a), the oxidation current peak increases along with the varying amounts of cholesterol from 50 to 500 mg/dL in the PBS buffer (pH 7.4) at the 100 mV/s scan rate. The cholesterol was oxidized in the presence of ChOx, which generated a number of electrons, as described in reaction (2). The calibration plots of the ChOx/CeO$_2$ NPs/PPy/electrode are replotted from the CV response, as shown in Figure 5(b). A linear relationship, with the cholesterol concentration ranging from 50 to 500 mg/dL, was observed following the linear regression equation of Y (mA) $= 9.27 \times 10^{-5} + 5.7 \times 10^{-6} \times$ [cholesterol] (mg/dL). The sensitivity of the cholesterol biosensor calculated from the slope

of the calibration curve was 5.7×10^{-6} mA/mg·dL^{-1}. A comparison of the developed biosensor with other cholesterol biosensors is presented in Figure 6. As shown in Figures 6(a) and (b), the developed cholesterol biosensor sensitivity is higher than those in the findings of Tiwari and Gong [20] and Wisitsoraat et al. [21], whereas it is lower than those in the findings of Khan et al. [22], Ansari et al. [23], and Dhand et al. [32]. The shelf life of the developed sensor is 13 weeks, which is better than that found by Wisitsoraat et al. [21], Khan et al. [22], Ansari et al. [23], and Dhand et al. [32] (Figure 6(c)). The linear range of the developed cholesterol biosensor is also good with respect to those of the other group (Figure 6(d)).

3.4. Optimal of the Experimental Conditions. The cholesterol biosensor was optimized for the pH value (Figure 7(a)). The magnitude of the oxidation current peak increased with the increase in pH from 5.0 to 7.4. The change in oxidation current peak with varying pH values can be attributed to the enzyme with maximum activity and the ChOx that was not denatured and thus had retained its natural structure. The oxidation current peak was reduced with the further increase in pH from 7.4 to 9.0. This condition may be due to the activity loss of the ChOx enzyme at the high pH value. Thus, the pH of 7.4 was used as the optimal value in all of the succeeding experiments.

The effect of working temperature on cholesterol biosensor response was studied in the range of 25°C to 55°C. As presented in Figure 7(b), the output signal of the biosensor increases with the increase in temperature to up to 40°C, and the value decreases when the temperature continuously increases above 40°C. This trend may be due to the enzymes that could have been denatured at the high temperature, thus losing their catalytic activity. The temperature of 40°C was considered the optimal temperature for cholesterol biosensor response. However, subsequent experiments were performed at room temperature for practical applications.

3.5. Selectivity, Storage Stability, and Reproducibility of the Cholesterol Biosensor. The selectivity measurements of the ChOx/CeO$_2$ NPs/PPy/electrode were evaluated in PBS containing 200 mg/dL cholesterol with and without glucose and ascorbic acid. The fabricated biosensor was negligibly influenced by interferences (Figure 8(a)). The response values of 2.67% and 2.36% accounted for 90 mg/dL glucose and 20 mg/dL ascorbic acid, respectively. The obtained results indicate that the ChOx/CeO$_2$ NPs/PPy/electrode is highly selective for practical applications.

The storage stability of the ChOx/CeO$_2$ NPs/PPy/electrode was further studied by storing it in PBS at 4°C; then, its response was tested (Figure 8(b)). The electrode activity retained 90% of its initial response after 9 weeks. After 13 weeks, the electrode response was 63%, which is higher than the value reported in the literature [21–23, 32].

Five different ChOx/CeO$_2$ NPs/PPy/electrodes were prepared, and their electrochemical responses were studied in PBS containing 200 mg/dL cholesterol. The CV technique was used to evaluate the reproducibility of the cho-

lesterol biosensor. As shown in Figure 8(c), all of the fabricated biosensors have the same response characterizations. The relative standard deviation of the parallel measurements for the five modified electrodes was 3.3%. This finding confirms that the cholesterol biosensor has good reproducibility.

4. Conclusion

In this study, we developed a cholesterol biosensor by using the CeO$_2$ NPS/PPy nanocomposite as the mediator to immobilize ChOx onto the electrode surface. The results confirm that the fabricated ChOx/CeO$_2$ NPs/PPy/electrode has a wide linear response range (50–500 mg/dL) and high sensitivity (5.7×10^{-6} mA/mg·dL^{-1}). In addition, the cholesterol biosensor exhibited good selectivity and reproducibility and acceptable storage stability. These results indicate that the developed cholesterol biosensor can be used as a useful tool for cholesterol detection in clinical diagnostics.

Data Availability

The data presented in this study are available on request from the corresponding author.

Conflicts of Interest

The authors declare that they have no conflicts of interest.

Acknowledgments

References

[1] H. B. Ma and K. J. Shieh, "Cholesterol and human health," *The Journal of American Science*, vol. 2, pp. 46–50, 2006.

[2] M. Nauck, W. Marz, and H. Wieland, "Is lipoprotein(a) cholesterol a significant indicator of cardiovascular risk?," *Clinical Chemistry*, vol. 46, no. 3, pp. 436-437, 2000.

[3] K. Hojo, H. Hakamata, A. Ito et al., "Determination of total cholesterol in serum by high-performance liquid chromatography with electrochemical detection," *Journal of Chromatography A*, vol. 1166, no. 1-2, pp. 135–141, 2007.

[4] K. Osada, A. Ravandi, and A. Kuksis, "Rapid analysis of oxidized cholesterol derivatives by high-performance liquid chromatography combined with diode-array ultraviolet and evaporative laser light-scattering detection," *Journal of the American Oil Chemists' Society*, vol. 76, no. 7, pp. 863–871, 1999.

[5] M. A. Paulazo and A. O. Sodero, "Analysis of cholesterol in mouse brain by HPLC with UV detection," *PLoS one*, vol. 15, no. 1, article e0228170, 2020.

[6] H. I. Oh, T. S. Shin, and E. J. Chang, "Determination of cholesterol in milk and dairy products by high-performance liquid chromatography," *Asian-Australasian Journal of Animal Sciences*, vol. 14, no. 10, pp. 1465–1469, 2001.

[7] K. Z. Liu, M. Shi, A. Man, T. C. Dembinski, and R. A. Shaw, "Quantitative determination of serum LDL cholesterol by

near-infrared spectroscopy," *Vibrational Spectroscopy*, vol. 38, no. 1-2, pp. 203–208, 2005.

[8] J. Wang, Y. J. Geng, B. Guo et al., "Near-infrared spectroscopic characterization of human advanced atherosclerotic plaques," *Journal of the American College of Cardiology*, vol. 39, no. 8, pp. 1305–1313, 2002.

[9] J. Chitra, M. Ghosh, and H. N. Mishra, "Rapid quantification of cholesterol in dairy powders using Fourier transform near infrared spectroscopy and chemometrics," *Food Control*, vol. 78, pp. 342–349, 2017.

[10] T. Lin, L. Zhong, H. Chen et al., "A sensitive colorimetric assay for cholesterol based on the peroxidase-like activity of MoS_2 nanosheets," *Microchimica Acta*, vol. 184, no. 4, pp. 1233–1237, 2017.

[11] X. Li, Z. Pu, and H. Zhou, "Synergistically enhanced peroxidase-like activity of Pd nanoparticles dispersed on CeO_2 nanotubes and their application in colorimetric sensing of sulfhydryl compounds," *Journal of Materials Science*, vol. 53, no. 19, pp. 13912–13923, 2018.

[12] Y. Lia, Z. Kang, L. Kong et al., "MXene-Ti_3C_2/CuS nanocomposites: enhanced peroxidase-like activity and sensitive colorimetric cholesterol detection," *Materials Science & Engineering C*, vol. 104, article 110000, 2019.

[13] A. K. Giri, C. Charan, A. Saha, V. K. Shahi, and A. B. Panda, "An amperometric cholesterol biosensor with excellent sensitivity and limit of detection based on an enzyme-immobilized microtubular ZnO@ZnS heterostructure," *Journal of Materials Chemistry A*, vol. 2, no. 40, pp. 16997–17004, 2014.

[14] U. Saxena and A. B. Das, "Nanomaterials towards fabrication of cholesterol biosensors: key roles and design approaches," *Biosensor and Bioelectronic*, vol. 75, pp. 196–205, 2016.

[15] M. Dervisevic, E. Çevik, M. Şenel, C. Nergiz, and M. F. Abasiyanik, "Amperometric cholesterol biosensor based on reconstituted cholesterol oxidase on boronic acid functional conducting polymers," *Journal of Electroanalytical Chemistry*, vol. 776, pp. 18–24, 2016.

[16] X. Lin, Y. Ni, and S. Kokot, "Electrochemical cholesterol sensor based on cholesterol oxidase and MoS_2-AuNPs modified glassy carbon electrode," *Sensors and Actuators B: Chemical*, vol. 233, pp. 100–106, 2016.

[17] A. Ahmadalinezhad and A. Chen, "High-performance electrochemical biosensor for the detection of total cholesterol," *Biosensors and Bioelectronics*, vol. 26, no. 11, pp. 4508–4513, 2011.

[18] C. Jianrong, M. Yuqing, H. Nongyue, W. Xiaohua, and L. Sijiao, "Nanotechnology and biosensors," *Biotechnology Advances*, vol. 22, no. 7, pp. 505–518, 2004.

[19] M. Mehrvar and M. Abri, "Recent developments, characteristics, and potential applications of electrochemical biosensors," *Analytical Science*, vol. 20, no. 8, pp. 1113–1126, 2004.

[20] A. Tiwari and S. Gong, "Electrochemical study of chitosan-SiO_2-MWNT composite electrodes for the fabrication of cholesterol biosensors," *Electroanalysis*, vol. 20, no. 19, pp. 2119–2126, 2008.

[21] A. Wisitsoraat, P. Sritongkham, C. Karuwan, D. Phokharatkul, T. Maturos, and A. Tuantranont, "Fast cholesterol detection using flow injection microfluidic device with functionalized carbon nanotubes based electrochemical sensor," *Biosensors and Bioelectronics*, vol. 26, no. 4, pp. 1514–1520, 2010.

[22] R. Khan, A. Kaushik, P. R. Solanki, A. A. Ansari, M. K. Pandey, and B. D. Malhotra, "Zinc oxide nanoparticles-chitosan com-

[23] A. A. Ansari, A. Kaushik, P. R. Solanki, and B. D. Malhotra, "Electrochemical cholesterol sensor based on tin oxide-chitosan nanobiocomposite film," *Electroanalysis*, vol. 8, pp. 965–972, 2009.

[24] I. S. Chronakis, S. Grapenson, and A. Jakob, "Conductive polypyrrole nanofibers via electrospinning: electrical and morphological properties," *Polymer*, vol. 47, no. 5, pp. 1597–1603, 2006.

[25] K. Singh, P. R. Solanki, T. Basu, and B. D. Malhotra, "Polypyrrole/multiwalled carbon nanotubes-based biosensor for cholesterol estimation," *Polymers for Advanced Technologies*, vol. 23, no. 7, pp. 1084–1091, 2012.

[26] A. Pawaiya, N. Jadon, and R. Jain, "Polypyrrole-cerium oxide nano composite glassy carbon platform for the quantification of Torsemide," *Insights Analytical Electrochemistry*, vol. 4, pp. 1–10, 2018.

[27] B. O. Özer and S. Çete, "Development of a novel biosensor based on a polypyrrole–dodecylbenzene sulphonate (PPy–DBS) film for the determination of amperometric cholesterol," *Artificial Cells, Nanomedicine, and Biotechnology*, vol. 45, no. 4, pp. 824–832, 2017.

[28] Y. Wang, X. Xiao, F. Zhang et al., "Synthesis of CeO2/PPy composites for use in the electrocatalytic detection of nitrite," *Inorganic and Nano-Metal Chemistry*, vol. 50, no. 12, pp. 1308–1314, 2020.

[29] N. T. Nguyet, L. T. H. Yen, V. Y. Doan et al., "A label-free and highly sensitive DNA biosensor based on the core-shell structured CeO_2-NR@Ppy nanocomposite for *Salmonella* detection," *Materials Science & Engineering C*, vol. 96, pp. 790–797, 2019.

[30] S. Seema and M. V. N. A. Prasad, "Studies on DC conductivity and LPG sensing behaviour of nanostructured polypyrrole CeO_2 composites," in , Article ID 030019*AIP Conference Proceedings*, vol. 1989, Solapur, India, 2018.

[31] T. T. N. Anh, L. T. Tam, V. V. Thu, A. T. Le, V. P. Hung, and P. D. Tam, "Nano-rods structured cerium oxide platform for cholesterol biosensor," *Journal of Inorganic and Organometallic Polymers and Materials*, vol. 30, no. 10, pp. 3886–3893, 2020.

[32] C. Dhand, M. D. G. Sumana, A. K. Srivastava et al., "Preparation, characterization and application of polyaniline nanospheres to biosensing," *Nanoscale*, vol. 2, no. 5, pp. 747–754, 2010.

WILEY | Hindawi

Research Article

Scalable Electrochemical Synthesis of Novel Biogenic Silver Nanoparticles and Its Application to High-Sensitive Detection of 4-Nitrophenol in Aqueous System

Van-Tuan Hoang [ID],[1] **Ngo Xuan Dinh** [ID],[1] **Tuyet Nhung Pham** [ID],[1] **Tran Vinh Hoang** [ID],[2] **Pham Anh Tuan,**[3,4] **Tran Quang Huy** [ID],[1,5] **and Anh-Tuan Le** [ID][1,3]

[1]*Phenikaa University Nano Institute (PHENA), Phenikaa University, Hanoi 12116, Vietnam*
[2]*School of Chemical Engineering, Hanoi University of Science and Technology, 01 Dai Co Viet Street, Hai Ba Trung District, Hanoi 10000, Vietnam*
[3]*Faculty of Materials Science and Engineering, Phenikaa University, Hanoi 12116, Vietnam*
[4]*Vicostone Joint Stock Company, Phenikaa Group, Hanoi 12116, Vietnam*
[5]*Faculty of Electric and Electronics, Phenikaa University, Hanoi 12116, Vietnam*

Correspondence should be addressed to Van-Tuan Hoang; tuan.hoangvan@phenikaa-uni.edu.vn
and Anh-Tuan Le; tuan.leanh@phenikaa-uni.edu.vn

This study reports a scalable green electrochemical synthesis of novel biogenic silver nanoparticles colloid (biogenic AgNPs) in large scale up to 5 liters using the bulk silver bar and the green tea leaves (*Camellia sinensis*) extract (GTE) as reducing agent during the electrochemical process. Under a direct-current voltage source, the biomolecules in GTE can release electrons to promote the reducing process of Ag^+ to Ag^0. More interestingly, the formation of the intermediate complex helps to cap on the nanoparticles, which leads to stabilizing AgNPs. The as-synthesized biogenic AgNPs with the size of 34 nm exhibit the outstanding electrochemical properties due to the presence of biomolecules on the biogenic AgNPs surface, which facilitates the effective attaching of AgNPs on the carbon surface of the screen-printed carbon electrode (SPE) through the formation of the strong C-O coordinate bonds between O atom of oxygen functional groups and C atom of SPE. The electrochemical properties of the biogenic AgNPs-modified SPE are enhanced significantly in comparison with bare SPE and pure AgNPs-SPE. The biogenic AgNPs-SPE is applied successfully to the detection of 4-nitrophenol (4-NP). The electrochemical sensor using biogenic AgNPs can reliably detect 4-NP in the linear range from 0.1 to 25 μM with the sensitivity about 6.69 μA μM^{-1} cm^{-2}. The present work reveals, as the greener synthesis method with ultra-large scalable ability, high purity, and excellent electrochemical properties of biogenic AgNPs is very promising for technological applications in high-sensitive electrochemical chemosensors, nanopharmaceuticals, and other fields.

1. Introduction

AgNPs are one of the nanomaterials possessing the highest degree of commercialization owing to the full range of potential applications in sensors, biomedical imaging, disinfection agents, healthcare products, cleaning agents, food storage, textile coatings, and medical devices [1–3]. The synthetic methods of AgNPs can be divided into chemical, physical, and biological synthesis [3], in which biosynthesis has attracted increasing interest in the production of biogenic AgNPs due to its simplicity, low cost, and usage of environmentally friendly materials. Instead of using chemical compounds as reducing agents, this approach employs natural biological agents, including plants, algae, bacteria, yeast, and fungi. These agents not only play roles to reduce silver ions (Ag^+) to metallic silver (Ag^0) but also stabilize the formed

AgNPs during the synthetic process. Plant extracts, more namely, green tea extract, have been widely used for the synthesis of AgNPs because it is a rich source of polyphenolic compounds [4, 5]. Moreover, the GTE has also been employed in cosmetic and therapeutic applications due to its safety and environmentally friendly. Unfortunately, despite having many unique advantages, the traditional methods used green tea extract have been still limited by requiring time-consuming and the difficulty in scaled-up production.

Meanwhile, the electrochemical method has been recently considered as a promising approach for the straightforward synthesis of pure AgNPs with high quality, large scale, and low cost [6, 7]. In this technique, the bulk silver electrodes are the major pure precursor for the formation of AgNPs. A bulk silver electrode is anodically dissolved to create Ag^+, and then, they are reduced to Ag^0 under the presence of metal salts in the electrolyte at the cathode. Based on the advantages and disadvantages of both biosynthesis method and electrochemical method, in this work, we propose a scalable green electrochemical process to rapidly synthesize biogenic AgNPs in large scale up to 5 liters using the bulk silver bar and the GTE as reducing agent to replace metal salts in the normal electrochemical method which is aimed at promoting synthetic efficiency in the short time and safety of the product. Besides, with the presence of biomolecules in extract solution, this reduces the large amounts of aggregation of silver on the surface of the cathode site and enhances their stability. Moreover, to analyze the applicability of the formed product, the biomolecule-based functionalized AgNPs are considered to be the critical factor of the electrode modification for the functional electrochemical sensors due to the unique features such as good electrocatalytic properties and high conductivity, as well as compatibility with other biomolecules [8, 9]. We have studied potential electrochemical properties of biogenic AgNPs as a signal translation probe towards the sensitive detection of 4-nitrophenol (4-NP), one of the hazardous substances causes headache, drowsiness, nausea, and cyanosis for humans, which is found into the environment as a side product in the production process of pharmaceuticals, pesticides, and dyes [10–12]. The formation mechanism and excellent electrochemical properties of biogenic AgNPs have been discussed in detail.

2. Experimental Procedures

2.1. Synthesis of Biogenic AgNPs by Modified Electrochemical Method. The proposed method for preparing biogenic AgNPs is based on the green electrochemical process using the inexpensive Ag metal bares as two electrodes. The GTE solution was prepared by boiling 1 g green tea leaves in 100 mL distilled water for 10 min. This extract solution was diluted to 500 mL at room temperature. Then, two parallel silver electrodes were immersed in a 500 mL glass beaker, which was filled extract solution under the magnetic stirring condition and was connected to the DC voltage source. The electrolysis was carried out with various supplied voltages from 4 V to 14 V at room temperature and under magnetic stirring for 30 min. The obtained biogenic AgNP solution was stored under ambient conditions in plastic containers.

Scaled-up production of the biogenic AgNPs has successfully performed using two large silver electrodes ($L \times W \times H = 45 \times 4 \times 0.6$ cm) and 6 L cylinder glass vase. The GTE solution was prepared by boiling 10 g green tea leaves in 1 liter distilled water for 10 min, filtering and then diluted to 5 L at room temperature. Electrolysis was carried out under continuous stirring for 60 min at room temperature and at a voltage of 12 V. The obtained product was stored under ambient conditions.

2.2. Characterization of Biogenic AgNPs. The biogenic AgNP formation was confirmed by an ultraviolet-visible (UV-vis) spectrophotometry (HP 8453 spectrophotometer). The crystalline structure of biogenic AgNPs was analyzed by a Bruker D5005 X-ray Diffractometer using Cu Kα radiation ($\lambda = 0.154056$ nm) under a voltage of 40 kV. The morphology of biogenic AgNPs was studied by a JEOL JEM 1010 transmission electron microscope (TEM) at an accelerating voltage of 80 kV.

2.3. Electrochemical Measurements. The screen-printed carbon electrodes (SPEs), DRP-110-U75 purchased from Metrohm, were carefully polished with 0.05 μm Al_2O_3 and were thoroughly cleaned by sonication in distilled water and ethanol. Biogenic AgNPs-SPEs were prepared by depositing three drops (1 μL each) of the biogenic AgNP solution onto a bare SPE. These electrodes were dried in air at room temperature. For comparison, pure AgNPs were synthesized by an electrochemical method as described above using $NaBH_4$ as both electrolyte and reductant agents instead of GTE solution. Pure AgNPs-SPEs were prepared with a similar procedure. Electrochemical measurements were performed using PalmSens 3 analyzer, controlled by a PC running PSTrace software version 4.8.1. The cyclic voltammetry (CV) was conducted from -0.3 V to 0.6 V with the scan rate of 50 mV s^{-1}. Electrochemical impedance spectroscopy (EIS) was recorded in 0.1 mol L^{-1} KCl solution, where the frequency range is from 0.01 Hz to 10 kHz with a signal amplitude of 5 mV.

3. Results and Discussion

3.1. The Characterization of As-Synthesized Biogenic AgNPs. The biogenic AgNPs formation was initially analyzed by optical properties using UV-visible spectroscopic analysis. Figure 1(a) shows the UV-vis absorption spectra of synthesized samples under different voltages. It can be seen that no absorption peak was found for the samples synthesized at the voltage of 4 V, 6 V, 8 V, and 10 V, respectively. In contrast, at the voltage of 12 V and 14 V, they exhibited strong absorption peaks at 437 nm and 443 nm, respectively, due to the surface plasmon resonance (SPR) effect of AgNPs [1, 2]. In our present experiment, it demonstrates that AgNPs did not form when the applied voltage was <12 V. On the other hand, it is also noted that the absorption band was shifted to longer wavelengths for biogenic AgNPs synthesized at 14 V as compared to the sample at 12 V. This shift can be attributed to the formation of the AgNPs with larger sizes in the solution. It can be seen that the applied voltage strongly affects the formation and growth of biogenic AgNPs.

(a)

(b)
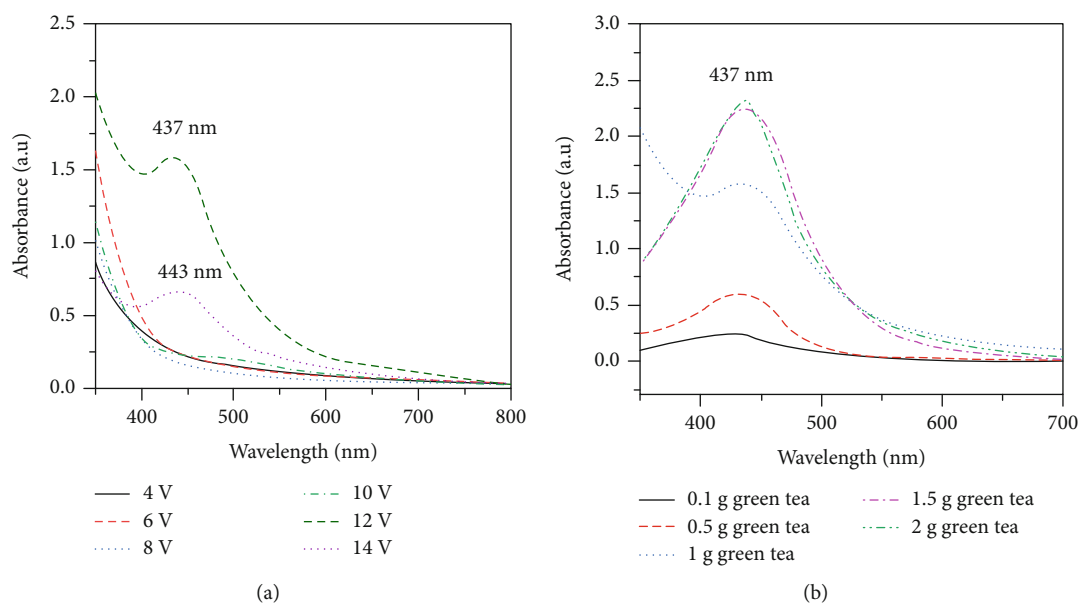
FIGURE 1: UV-vis spectra of the synthesized biogenic AgNPs corresponding to the different supplied voltages from (a) 4 V to 14 V and different amounts of green tea from (b) 0.1 g to 2 g.

(a)

(b)

(c)
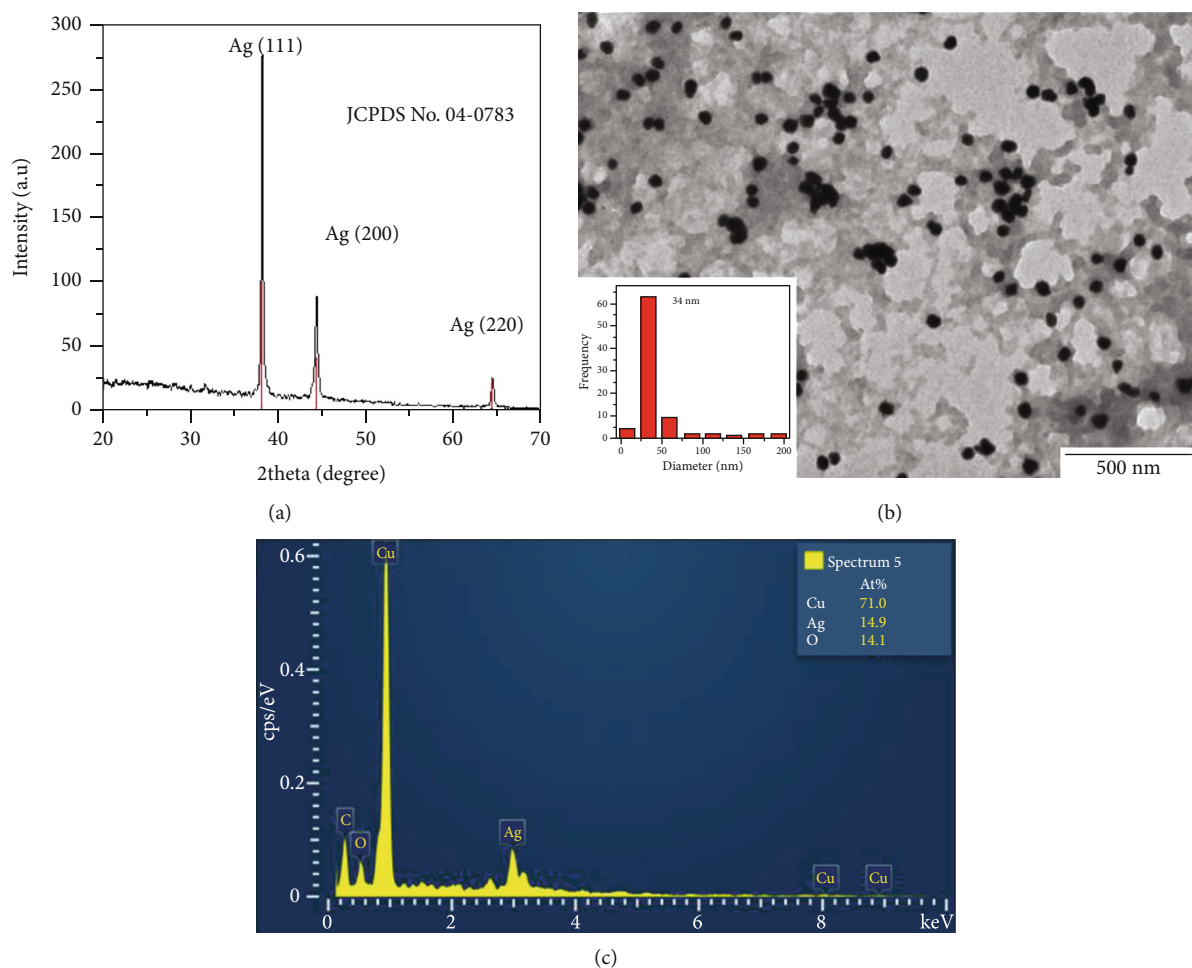
FIGURE 2: (a) XRD pattern, (b) TEM image, and (c) EDX spectrum of the biogenic AgNPs synthesized at 12 V.
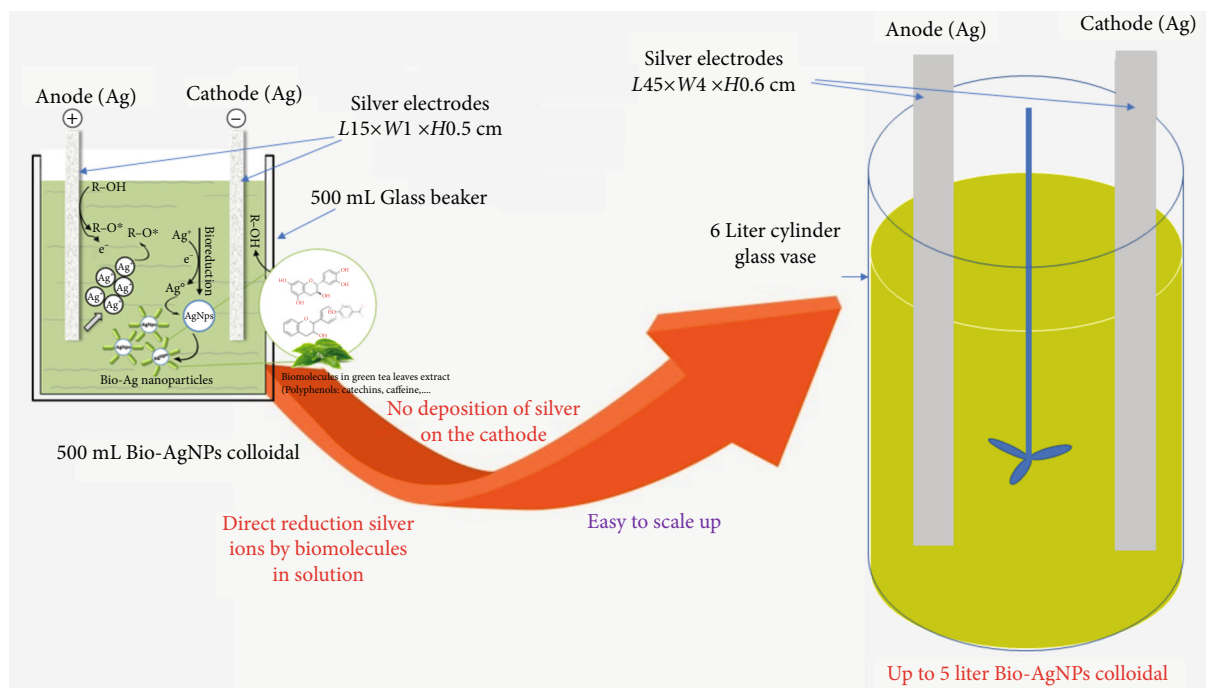
FIGURE 3: Schematic representation of the biogenic AgNPs' scale-up generation mechanism by using both electrochemical process and GTE as the reducing agent.

Additionally, the effect of the amount of green tea on the yield of biogenic AgNPs was also evaluated using UV-vis spectroscopy. Figure 1(b) shows the UV-vis absorption spectra of biogenic AgNPs prepared using various amounts of GTE. It was also observed that the intensity of SPR band at 437 nm obviously increased with increasing amount of green tea and reached maximum at 2 g. The increase of characteristic band intensity is attributed to the increasing number of nanoparticles formed as a result of greater releasing of Ag^+ ions from Ag anode at higher GTE concentration [7, 13]. These results indicate that the amount of green tea can affect the yield of biogenic AgNPs. However, when the amount of green tea is 2 g, the further increase of number of Ag^+ ions and the released oxygen can increase the formation of Ag_2O leads to the yield of biogenic AgNPs is decreased.

The formation of biogenic AgNPs was further confirmed by X-ray and TEM measurements. XRD analysis and TEM results of biogenic AgNPs were shown in Figure 2. In Figure 2(a), it is clear to see three diffraction peaks at 38.1°, 44.3°, and 64.4° correspond to the d(111), d(200), and d(220) fcc crystal planes of bulk Ag (JCPDS No. 04-0783), respectively. The TEM observation also reveals that as-synthesized biogenic AgNPs were spherical, homogeneous in size range of 34 nm, and shape. As shown in Figure 2(b), it can be seen that the presence of other material membrane around silver nanoparticles might be due to the formation of biomolecule matrix from GTE. The EDX spectrum of the biogenic AgNPs (Figure 2(c)) reveals the existence of Ag, O, and C components in the sample. The existence of O and C components can be due to emission from the formation of biomolecule matrix around AgNPs. In addition, EDX spectrum confirmed a high atomic weight percentage of Cu element, due to emission of the copper substrate used in the SEM and EDX measurements. These results exhibited that novel biogenic AgNPs were successfully synthesized by using both green electrochemical method and GTE extracts as reducing agent.

3.2. The Formation Mechanism of Biogenic AgNPs by GTE-Mediated Green Electrochemical Method. As described in Figure 3 and according to some previous reports, under a direct-current voltage source, the electron transfer occurred at the anode side, biomolecules in GTE (R-OH) were decreased to form R-O. radicals and release electrons [14]. Then, Ag^+ ions, which were released from the anode, interacted with R-O. radicals and received electrons to form Ag^0 atoms. As a result, the silver atoms then grew to form the biogenic AgNPs. Here, the biomolecules played an essential role in both reductant and stabilizer for AgNPs. Stabilization may likely be caused by capping of natural biomolecules such as the flavonoid and terpenoid components to create a monolayer on the AgNPs surface in solution. On the other hand, the formation of AgNPs on the cathode side as explained by Khaydarov et al. [6] could be taken place, but it was remarkably prevented due to the formation of R-OH—Ag^+ and stirring force of a magnetic stirrer. The processes of the AgNP formation are described below [6, 13–15].

(1) The formation of R-O. radicals and releasing of Ag^+ ions from Ag anode:

$$R\text{-}OH \rightarrow R\text{-}O + H^+ + e^-$$
$$Ag^0 - e^- \rightarrow Ag^+ \tag{1}$$

(a)

(b)

(c)
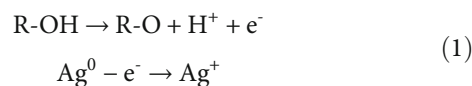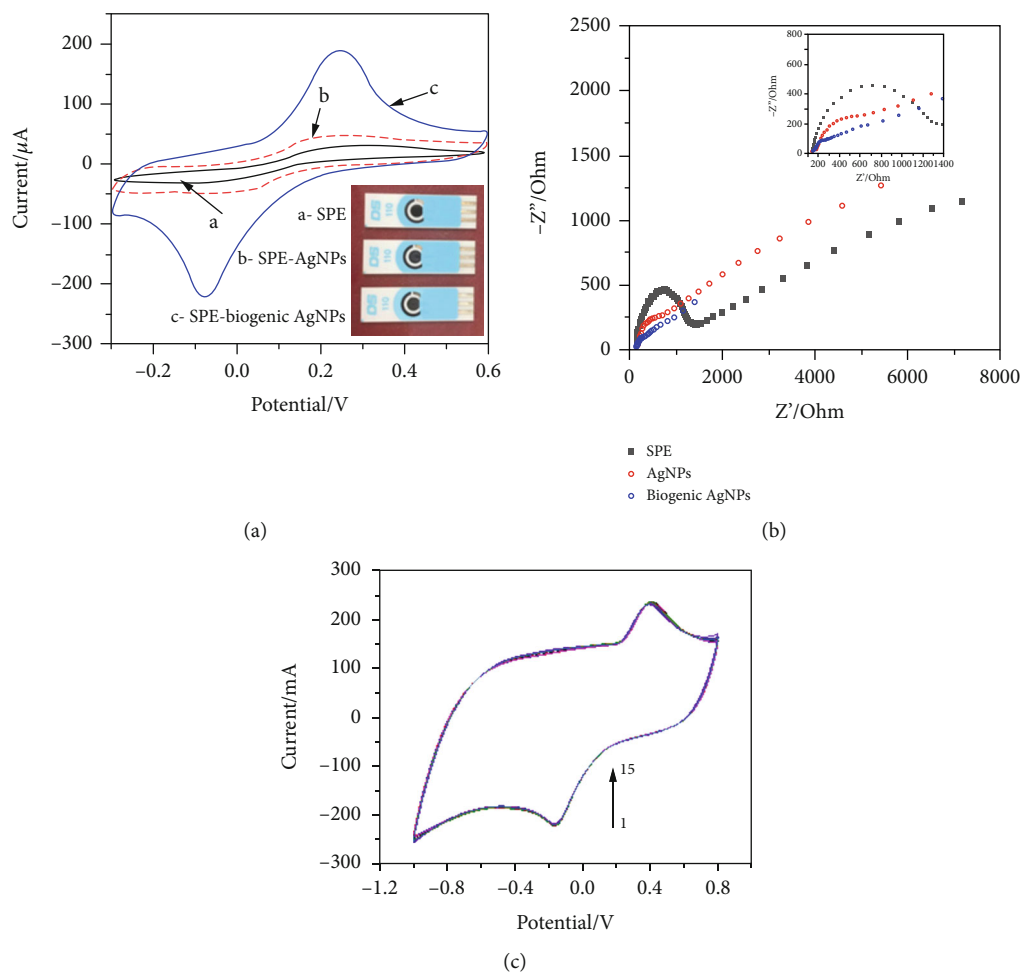
FIGURE 4: (a) CV of bare SPE (curve a), pure AgNPs-SPE (curve b), and biogenic AgNP-SPE (curve c) electrodes in 5 mM $K_3[Fe(CN)_6]/K_4[Fe(CN)_6]$ (1 : 1) mixture at 50 mV s^{-1}; (b) Nyquist plots of bare SPE, pure AgNPs-SPE, and biogenic AgNP-SPE electrodes recorded in 0.1 mol L^{-1} KCl solution containing 5 mM $K_3[Fe(CN)_6]/K_4[Fe(CN)_6]$; (c) CV of biogenic AgNP-SPE electrode for 15 cycles.

(2) The formation of the intermediate complex:

$$R\text{-}O + Ag^+ \rightarrow R\text{-}O\text{-}\text{-}\text{-}Ag^+ \qquad (2)$$

(3) Reductive formation of Ag^0 atom in solution:

$$R\text{-}O + Ag^+ + e^- \rightarrow R = O(quinone) + Ag^0 \qquad (3)$$
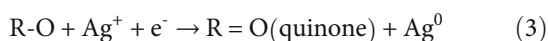
Role of the -OH groups in the bioreduction of Ag^+ to Ag^0 and the formation of AgNPs was discussed by Hussain and Khan [16]. It is easy to transfer the proton to Ag^+ ions to form AgNPs under an applied voltage condition. Moreover, the formation of the intermediate complex (R-O—Ag^+) not only enhances the formed AgNP stabilization [17] and protects them from the oxidation arising from the release of oxygen or hydrogen due to the electrolysis of water in GTE, but also prevents the reduction of Ag^+ ions at the surface of the cathode. Thus, the technological yield of AgNP synthesis process was significantly improved compared to some conventional electrochemical methods. The synthesis yield of AgNP formation calculated is about 98%.

In the synthesis of biogenic AgNPs using normal plant extracts, biogenic AgNP production was affected by many other factors such as the reducing capacity of the biomolecules, extract dosage, reaction time, and temperature [4, 16]. For the synthesis of biogenic AgNPs using GTE at room temperature and pressure, the preparation time from 2 h to 24 h was needed [17, 18]. The reduction process in a long time causes poor crystallization of AgNPs, low efficiency, and difficulty in the large scale-up produce [19]. In fact, some recent reports show that the biogenic AgNP formation process was promoted and controlled by using high temperature [13], microwave [4], and hydrothermal [20]. Instead of that, in this study, the utilization of the direct current contributes to promote the electron releasing process and the formation of R-O. radicals. According to that, the reducing process of Ag^+ into Ag^0 induced more quickly, leading to improve the quality of biogenic AgNP nanocrystals. It should be emphasized that the above-proposed method not only offers many promising benefits for biogenic AgNPs synthesis in the future such as lowcost, without using chemical additives, rapid synthesis, and simple scale-up but also uses the herb resources from nature. The technological keys to the electrochemical
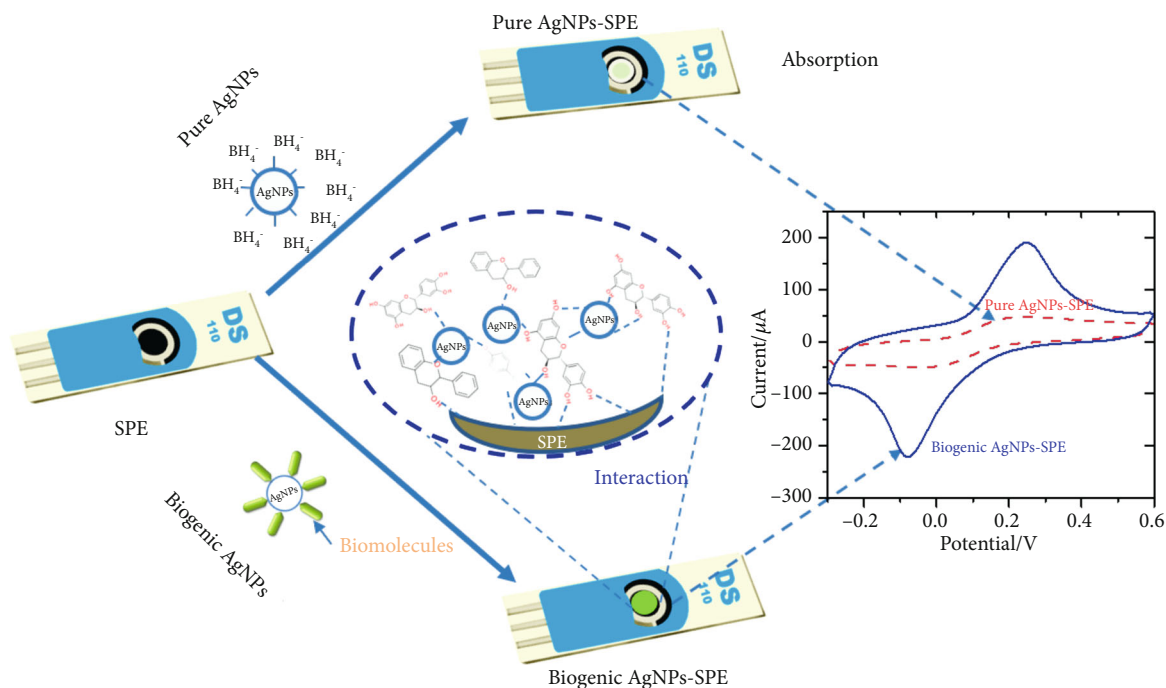
FIGURE 5: A mechanism for the enhanced electrochemical properties of the biogenic AgNPs deposited on the surface of the SPE compared to the pure AgNPs.

synthesis of biogenic AgNPs are the voltage value applied on two electrodes in green tea leave extract.

3.3. The Electrochemical Activity of Novel Biogenic AgNPs.
The electrochemical activity of novel biogenic AgNPs was analyzed and compared to pure AgNPs using two electrochemical techniques, including the CV and EIS techniques. We evaluated the charge transfer performance of as-prepared samples, and the CV of bare SPE, pure AgNPs-SPE, and biogenic AgNP-SPE electrodes was recorded in a mixture of 5 mM $K_3[Fe(CN)_6]/K_4[Fe(CN)_6]$ (1:1) at a scan rate of 50 mV s^{-1} as shown in Figure 4(a). For the bare SPE, the cyclic voltammetry response displayed the low current signal (I_a = 28 μA and I_c = −26 μA). The CV response was improved for pure AgNPs-SPE (I_a = 30 μA and I_c = −43 μA), suggesting that pure AgNPs were decorated on the SPE surface. More interestingly, compared to the bare SPE and pure AgNPs-SPE, biogenic AgNPs-SPE exhibited the outstanding current signal with I_a = 137 μA and I_c = −182 μA. This current signal enhancement can be due to the excellent conductivity and the large specific surface area of uniform biogenic AgNPs, as well as the formation of biomolecule matrix around AgNPs.

Figure 4(b) illustrates that the Nyquist plots of bare SPE, pure AgNPs-SPE, and biogenic AgNP-SPE electrodes were recorded in 0.1 mol L^{-1} KCl solution containing 5 mM $K_3[Fe(CN)_6]/K_4[Fe(CN)_6]$. As can be observed, the Nyquist plots of all electrodes displayed a semicircle portion at higher frequencies to a limited electron transfer process and a linear part at a lower frequency range corresponding to the diffusion process. For the bare SPE, the calculated value of electron-transfer resistance (R_{ct}) from diameter of semicircle

was about 1109 Ω (Figure 4(b), black curve). After bare SPE was modified with pure AgNPs, the value of R_{ct} decreased to 504 Ω. Particularly, compared with pure AgNPs-SPEs, the EIS of the biogenic AgNPs-SPEs showed smaller semicircular regions with a R_{ct} value of approximately 140 Ω. The lower R_{ct} value for biogenic AgNPs-SPEs indicates that the electron transport rate between the medium and electrode was significantly increased upon the SPE modification with biogenic AgNPs, which can be due to the effect of biomolecule matrix in the ability of modified electrode. These results also corroborated well the obtained results from CV measurements. More particularly, the electrochemical stability performance of biogenic AgNP-SPE electrode was also examined. As shown in Figure 4(c), after 15 cycles, the change of the reduction peak currents in CV measurements only varied ~2.4%, indicating that the active electrode surface and the immobilization of biogenic AgNPs on the SPE surface were extremely stable. The mechanism for the enhanced electrochemical properties of biogenic AgNPs deposited on the surface of the SPE as compared with pure AgNPs was described in Figure 5. This enhancement can be attributed due to the attachment of biogenic AgNPs on the carbon surface of the SPE through the formation of the C-O coordinate bonds between O atom of biomolecules on the biogenic AgNPs surface and C atom of SPE [21, 22]. The bonding formation of biogenic AgNPs with SPE based on biomolecules as a linker helps enhance the electron transfer kinetics and stability during the electrochemical process. Besides, the presence of biomolecule matrixes owning many flexible π-π bonds around AgNPs also facilitates the rapid electron transfer and enhances the active surface area. In contrast, for pure AgNPs-SPE, AgNPs which were stabilized
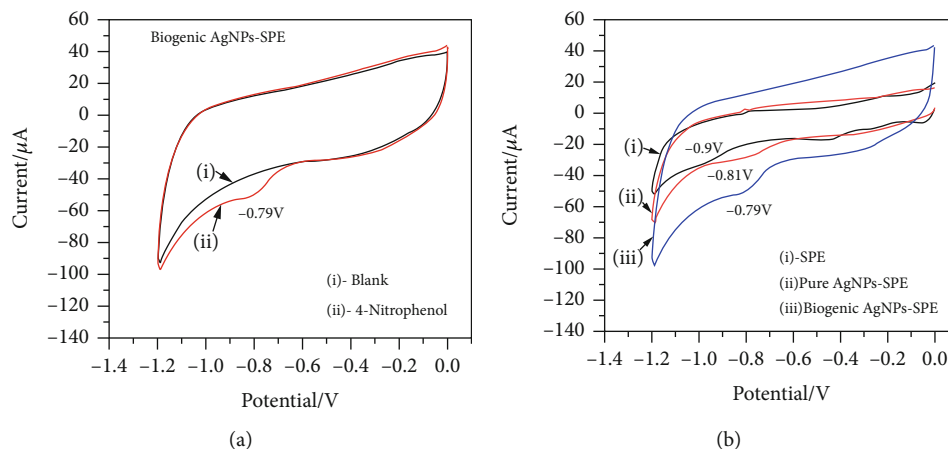
FIGURE 6: CV of (a) $10\,\mu M$ 4-NP at biogenic AgNPs-SPE in 0.1 M PBS (pH 7.4); (b) $10\,\mu M$ of 4-NP at bare SPE, pure AgNPs-SPE, and biogenic AgNPs-SPE in 0.1 M PBS (pH 7.4).
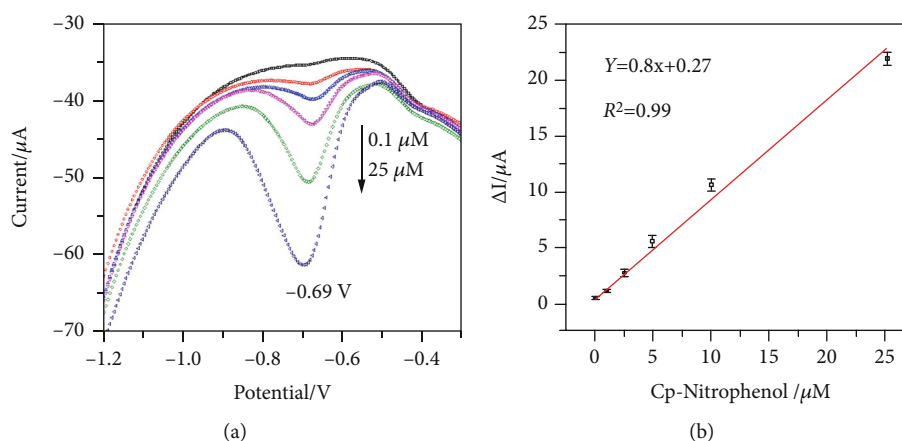
FIGURE 7: DPV in 0.1 M PBS (pH 7.4) containing different concentrations of 4-NP: (a) biogenic AgNPs-SPE for 4-NP at different concentrations and (b) linear relationship between peak currents and 4-NP concentrations.

by BH_4^- are only absorbed physically on the SPE surface without bonding agents. More importantly, biogenic AgNP-SPE is able to easily and strongly adsorb the analytes such as ions, chemical compounds due to the conjugation effect and electrostatic interaction of biomolecules, along with that the oxygen functional groups can improve the electrocatalytic activity of the synthesized electrode [23]. These results suggest that the biogenic AgNPs-SPE will be an ideal candidate for green electrochemical sensors in a variety of environmental monitoring and biomedical applications.

3.4. The Use of Biogenic AgNPs as Probe for Detection of 4-Nitrophenol. In the following, to demonstrate further the promising electrochemical properties of the biogenic AgNPs-SPE, the 4-NP detection capability using the SPE, pure AgNPs-SPE, and biogenic AgNPs-SPE electrodes was performed (Figure 6) in 0.1 M PBS (pH 7.4). Figure 6(a) shows the CV response of the biogenic AgNPs-SPE in 0.1 M PBS (pH 7.4) without (curve i) and with $10\,\mu M$ 4-NP (curve ii). In the case adding of 4-NP, there was a sharp peak

at -0.79 V, which is good agreement with some previous reports related to the reduction peak of 4-NP [10–12].

Figure 6(b) shows the CV response of $10\,\mu M$ of 4-NP in 0.1 M PBS (pH 7.4) for all the three electrodes. The results show that it was observed at the reduction peak of 4-NP at -0.9 V (curve i), -0.81 V (curve ii), and -0.79 V (curve iii) in the case of the SPE, pure AgNPs-SPE, and biogenic AgNPs-SPE, respectively. The pure AgNPs-SPE and biogenic AgNPs-SPE showed the higher catalytic current responses than that of bare SPE. This result indicates that AgNP-modified electrodes possess good electrocatalytic ability towards 4-NP, due to the good conductivity and compatibility of AgNPs [8, 12]. Additionally, the biogenic AgNPs-SPE showed the enhancement of current signal when compared to pure AgNPs-SPE because of the presence of the biomolecule matrix. This enhancement is a positive result arising from the strong electrostatic interaction and new bindings formed between biomolecules and 4-NP as proposed above.

Figure 7(a) exhibits the differential pulse voltammetry (DPV) response of the biogenic AgNPs-SPE for the variation in the concentrations of 4-NP at the scan rate of $6\,mV\,s^{-1}$ and

the potential scanning from -0.4 V to -1.2 V. In the concentration range of 0.1-25 μM, the obtained calibration curves (Figure 7(b)) show that there was a linear relationship between the electrochemical responses and 4-NP concentrations with the correlation coefficient, $R^2 = 0.99$. The sensitivity for this electrode was found to be 6.69 μA μM^{-1} cm^{-2}. From this observation, it is clear that the utilization of biogenic AgNPs as electrocatalyst created a positive effect on electron transfer process during the redox reaction of 4-NP; furthermore, it played an essential role as great electrocatalyst for the reduction of 4-NP.

4. Conclusions

A scalable green electrochemical method has been presented for the rapid and large synthesis of biogenic AgNPs using the bulk silver bars and GTE as reducing agent, along with a direct-current voltage source. The proposed method was based on a simple electrochemical process that can rapidly synthesize the purity biogenic AgNPs with high yield, notably, without the use of any additive chemicals. Interestingly, the as-synthesized biogenic AgNPs with an average particle size of 34 nm were applied as an excellent probe for the 4-NP detection. The biogenic AgNPs-SPE demonstrated good sensitivity (6.69 μA μM^{-1} cm^2) in the linear range from 0.1 μM to 25 μM of 4-NP, suggesting that biogenic AgNPs are the ideal candidates for green electrochemical sensors. It can be believed that the biogenic AgNPs will be a promising material for biomedical and bio/chemosensing applications.

Data Availability

Data are available on request.

Conflicts of Interest

The authors declare that they have no conflicts of interest.

Authors' Contributions

V.T. Hoang and N.X. Dinh contributed equally to this work.

Acknowledgments

References

[1] Y. A. Krutyakov, A. A. Kudrinskiy, A. Y. Olenin, and G. V. Lisichkin, "Synthesis and properties of silver nanoparticles: advances and prospects," *Russian Chemical Reviews*, vol. 77, no. 3, pp. 233–257, 2008.

[2] B. Zewde, A. Ambaye, J. Stubbs Iii, and D. Raghavan, "A review of stabilized silver nanoparticles–synthesis, biological properties, characterization, and potential areas of applications," *Nanomed*, vol. 4, p. 1043, 2016.

[3] Q. H. Tran, V. Q. Nguyen, and A.-T. Le, "Silver nanoparticles: synthesis, properties, toxicology, application and perspec-

[4] M. Sökmen, S. Y. Alomar, C. Albay, and G. Serdar, "Microwave assisted production of silver nanoparticles using green tea extracts," *Journal of Alloys and Compounds*, vol. 725, pp. 190–198, 2017.

[5] W. R. Rolim, M. T. Pelegrino, B. de Araújo Lima et al., "Green tea extract mediated biogenic synthesis of silver nanoparticles: characterization, cytotoxicity evaluation and antibacterial activity," *Applied Surface Science*, vol. 463, pp. 66–74, 2019.

[6] R. A. Khaydarov, R. R. Khaydarov, O. Gapurova, Y. Estrin, and T. Scheper, "Electrochemical method for the synthesis of silver nanoparticles," *Journal of Nanoparticle Research*, vol. 11, no. 5, pp. 1193–1200, 2009.

[7] D. T. Thuc, T. Q. Huy, L. H. Hoang et al., "Green synthesis of colloidal silver nanoparticles through electrochemical method and their antibacterial activity," *Materials Letters*, vol. 181, pp. 173–177, 2016.

[8] C. Karuppiah, S. Palanisamy, S.-M. Chen et al., "Green biosynthesis of silver nanoparticles and nanomolar detection of p-nitrophenol," *Journal of Solid State Electrochemistry*, vol. 18, no. 7, pp. 1847–1854, 2014.

[9] M. Mavaei, A. Chahardoli, Y. Shokoohinia, A. Khoshroo, and A. Fattahi, "One-step synthesized silver nanoparticles using isoimperatorin: evaluation of photocatalytic, and electrochemical activities," *Scientific Reports*, vol. 10, no. 1, p. 1762, 2020.

[10] C. Zhang, S. Govindaraju, K. Giribabu, Y. S. Huh, and K. Yun, "AgNWs-PANI nanocomposite based electrochemical sensor for detection of 4-nitrophenol," *Sensors and Actuators B: Chemical*, vol. 252, pp. 616–623, 2017.

[11] B. Dinesh and R. Saraswathi, "Electrochemical synthesis of nanostructured copper-curcumin complex and its electrocatalytic application towards reduction of 4-nitrophenol," *Sensors and Actuators B: Chemical*, vol. 253, pp. 502–512, 2017.

[12] N. I. Ikhsan, P. Rameshkumar, and N. M. Huang, "Controlled synthesis of reduced graphene oxide supported silver nanoparticles for selective and sensitive electrochemical detection of 4-nitrophenol," *Electrochimica Acta*, vol. 192, pp. 392–399, 2016.

[13] M. R. Siddiqui, M. Khan, A. Khan, W. T. Tahir, and W. Khathlan, "Green synthesis of silver nanoparticles mediated by Pulicaria glutinosa extract," *International Journal of Nanomedicine*, vol. 1507, 2013.

[14] S. R. Waldvogel, S. Mentizi, and A. Kirste, "Boron-doped diamond electrodes for electroorganic chemistry," in *Radicals in Synthesis III* pp. 1–31, Springer, Berlin, Heidelberg.

[15] N. Tarannum, D. Divya, and Y. K. Gautam, "Facile green synthesis and applications of silver nanoparticles: a state-of-the-art review," *RSC Advances*, vol. 9, no. 60, pp. 34926–34948, 2019.

[16] S. Hussain and Z. Khan, "Epigallocatechin-3-gallate-capped Ag nanoparticles: preparation and characterization," *Bioprocess and Biosystems Engineering*, vol. 37, no. 7, pp. 1221–1231, 2014.

[17] A. Gade, S. Gaikwad, V. Tiwari, A. Yadav, A. Ingle, and M. Rai, "Biofabrication of silver nanoparticles by Opuntia ficus-indica: in vitro antibacterial activity and study of the mechanism involved in the synthesis," *Current Nanoscience*, vol. 6, no. 4, pp. 370–375, 2010.

[18] Q. Sun, X. Cai, J. Li, M. Zheng, Z. Chen, and C.-P. Yu, "Green synthesis of silver nanoparticles using tea leaf extract and evaluation of their stability and antibacterial activity," *Colloids and*

tives," *Advances in Natural Sciences: Nanoscience and Nanotechnology*, vol. 4, article 033001, 2013.

Surfaces A: Physicochemical and Engineering Aspects, vol. 444, pp. 226–231, 2014.

[19] M. A. Asghar, E. Zahir, S. M. Shahid et al., "Iron, copper and silver nanoparticles: green synthesis using green and black tea leaves extracts and evaluation of antibacterial, antifungal and aflatoxin B1 adsorption activity," *LWT*, vol. 90, pp. 98–107, 2018.

[20] P. Tippayawat, N. Phromviyo, P. Boueroy, and A. Chompoosor, "Green synthesis of silver nanoparticles in aloe vera plant extract prepared by a hydrothermal method and their synergistic antibacterial activity," *PeerJ*, vol. 4, article e2589, 2016.

[21] V. Kumar, R. K. Gupta, R. K. Gundampati et al., "Enhanced electron transfer mediated detection of hydrogen peroxide using a silver nanoparticle–reduced graphene oxide–polyaniline fabricated electrochemical sensor," *RSC Advances*, vol. 8, p. 619, 2018.

[22] J. Simonet, "Enolization versus carbonylation at glassy carbon surface through cathodic means," *Electrochemistry Communications*, vol. 31, pp. 1–4, 2013.

[23] T. Sun, H. Pan, Y. Mei et al., "Electrochemical sensor sensitive detection of chloramphenicol based on ionic-liquid-assisted synthesis of de-layered molybdenum disulfide/graphene oxide nanocomposites," *Journal of Applied Electrochemistry*, vol. 49, no. 3, pp. 261–270, 2019.

WILEY | Hindawi

Research Article

The Effect of Multiwalled Carbon Nanotubes on the Thermal Conductivity and Cellular Size of Polyurethane Foam

Huynh Mai Duc [ID],[1] **Dat Nguyen Huu** [ID],[1] **Trung Tran Huu** [ID],[1] **Lu Le Trong,**[1] **Hai Luong Nhu** [ID],[2] **Hong Phan Ngoc,**[2] **Thao Nguyen Van,**[2] **Quynh Hoa Kieu Thi** [ID],[3] **and Giang Nguyen Vu** [ID][1]

[1]*Institute for Tropical Technology, Vietnam Academy of Science and Technology, Vietnam*
[2]*Centre for High Technology Development, Vietnam Academy of Science and Technology, Vietnam*
[3]*Institute of Biotechnology, Vietnam Academy of Science and Technology, Vietnam*

Correspondence should be addressed to Giang Nguyen Vu; nvgiang@itt.vast.vn

Polyurethane (PU) foam is known as the popular material for the applications in many fields of industry and life. To improve the mechanical and thermal properties of this material, in this research, PU foam was reinforced with aniline-modified multiwalled carbon nanotubes (MWCNTs). Fourier transform infrared FTIR spectrum of modified MWCNTs showed the aniline was grafted on the surface of MWCNTs through the appearance of $-NH_2$ stretches. The effect of MWCNTs with and without modification on the density, porosity, compressive strength, and heat conductivity of PU/MWCNT foam nanocomposites was investigated. The dispersibility of MWCNTs in the PU matrix was enhanced after modification with aniline. Compressive strength of PU nanocomposite reached the highest value after adding 3 wt.% of modified MWCNTs into PU foam. Besides, the water uptake of PU nanocomposites using 3 wt.% of MWCNTs was decreased to 13.4% as compared to that using unmodified MWCNTs. The improvement in thermal conductivity of PU/aniline-modified MWCNT nanocomposite was observed due to the change in the cellular size of PU foam in the presence of MWCNTs as shown by SEM images.

1. Introduction

Unlike most plastics, polyurethane (PU) foam belongs to the cellular material that possesses unique properties in thermal porosity and mechanical properties. These properties can be changed in a wide range by adjusting the raw materials to manufacture PU foam such as polyol, isocyanate, and catalysts. Thanks to such flexible properties, PU foam has been applied in many different areas from aerospace components, ships, ballistic vests, and automobiles [1, 2]. However, the material has some drawbacks due to low mechanical and thermal properties that limit its applications [2]. Therefore, many researchers have focused on overcoming these disadvantages in order to improve the properties of PU foam [3, 4].

A great deal of studies have been reported on PU nanocomposite foams that reinforced with different types of nano-particles such as nanoclay [4–6], titanium dioxide [7], and carbon nanofibers [8–10] to create a class of foam material with promising properties. In the research of Xu et al. [11], the addition of 2 phr of organoclay nanoparticles into PU foam led to the improvements in the tensile and compressive strengths of PU foam (110 and 152%, respectively). Saha et al. [2] used 1 wt.% of TiO_2 nanoparticles to reinforce PU foam. The obtained results showed a slight increase in Young's modulus, tensile strength, and compression strength of the PU/TiO_2 nanocomposites about 14.6%, 5%, and 16.2%, respectively, as compared to PU foam. Carbon nanofibers (CNFs) were also studied as high-performance reinforcement additives for PU foam due to their excellent axial tensile strength, superior thermal and electrical properties, and thermal conductivity [12–14]. Guo et al. [15] reported that both the tensile modulus and tensile strength of the PU/MWCNT nanocomposites are remarkably enhanced by about 90% as

comparison with pure PU foam as the addition of 1 wt.% of MWCNTs into PU foam. Importantly, the elongation at break of PU/carbon nanotube (CNT) composite is greatly improved by about 500%, indicating that the toughness of neat PU is enhanced by adding CNTs into the matrix. Similar results were also reported by Sinaret for MWCNTs reinforced PU foam [3]. Compressive strength of PU/MWCNT composite with 0.5 wt.% of filler reached the peak at 1.162 MPa as compared to other foam composites. The energy absorption was increased from 22.89 J for PU matrix to 24.53 J for foam composites with 3 wt.% of MWCNTs.

Although previous papers showed that MWCNTs could significantly improve the properties of the PU foam nanocomposites, the number of papers regarding thermal conductivity of PU/MWCNT foam nanocomposites is somewhat scarce.

Carbon nanotubes (CNTs) were known as a sunlight absorber that has low cost, reusability, and excellent light-to-heat conversion properties [16]. Under sunlight, CNTs can absorb and scatter photons due to the strong interaction between CNTs and incident solar light; the generation of heat occurs from the surface of the CNTs where strong coupling occurs between the incident radiation and the electrons on the surface of the CNTs [17]. For PU foam composites, the generated heat on the surface of the CNTs could then transfer to the matrix and was stored in cell structure. Santiago-Calvo et al. [18] have modeled the thermal conductivity of PU/CNT foam through four heat conduction mechanisms: conduction along the cell walls and the struts of the solid polymer, conduction through the gas phase, thermal radiation, and convection within the cells. The authors indicated that the thermal conductivity of a PU foam could be improved by an addition of small amount of CNT nanoparticles (0.1–0.4 wt.% of CNT). However, the thermal conductivity of PU foam nanocomposites reinforced a large amount in the range of 1-5 wt.% of MWCNTs which has not been mentioned yet.

Therefore, this study will prepare the foam nanocomposites containing MWCNTs with high concentrations. The thermal conductivity, morphology, and compressive strength of foam nanocomposites will be also investigated and discussed in detail. Moreover, MWCNTs have been modified with aniline to improve the compatibility with PU matrix as well as the properties of PU foam nanocomposites.

2. Experiment

2.1. Material. Methyl diphenyl diisocyanate (MDI) and polypropylene polyethylene (PPG) were the products of Oriken chemical company, Malaysia. Multiwalled carbon nanotubes (MWCNTs) with a purity of 99% used in this study was supplied by Institute of Materials Science, Vietnam Academy of Science and Technology, Vietnam. The MWCNTs has an average diameter of 20 nm and a length of 50-200 microns. Aniline (purity of 99.5%) and nitric acid (concentration of 68%) were supplied by Xilong Chemical Company (China). Absolute alcohol was bought from Duc Giang Chemical Company (Vietnam).

2.2. Preparation of PU Foam and PU/MWCNT Foam Nanocomposites

2.2.1. Modification of MWCNTs with Aniline. First, MWCNTs were treated by concentrated nitric acid before being filtered and washed by distilled water to a pH of 7 [19, 20] and then dried at 80°C for 24 hours to obtain treated MWCNTs. After treatment, MWCNTs were modified with aniline as follows: 0.528 g MWCNTs were added into a mixture containing 120 ml of water and 20 ml of ethanol under sonication for 30 minutes at room temperature. Next, 6 g glyceride and aniline solution were added into a solution under stirring at 70°C for 24 hours. Finally, the MWNTs were filtered and washed with distilled water before being dried at 80°C for 6 hours.

2.2.2. Fabrication of PU/MWCNT Foam Nanocomposites. The PU foam nanocomposites containing 0, 1, 3, and 5 wt.% of MWCNTs were prepared as follows: MWCNTs were firstly added to the polyol under mechanically stirring for 5 minutes at 1200 rpm. The mixture continued to be ultrasound by using T18 digital Ultra Turrax (IKA) for 30 minutes at 20 kHz of frequency. Finally, isocyanate was added to the MWCNT/polyol mixture using mechanical mixer with 1500 rpm for 10 seconds. After that, the mixture was quickly poured into a mould with dimensions 250 × 250 × 250 mm and left to foam freely in one direction for 24 h before removing from the mould. PU foam without MWCNTs was prepared under the same conditions.

2.3. Characterizations

2.3.1. Fourier Transform Infrared (FTIR) Spectra. Fourier transform infrared spectra (FTIR) were used to analyze samples with and without modification on a Fourier Nexus 670 spectrometer (USA), in the wave range of 4000-400 cm^{-1} with a resolution of 4 cm^{-1} and an average of 32 scans.

2.3.2. Density and Porosity. The density of PU foam nanocomposites is determined according to ASTMD 1622-93, and the porosity of PU foam samples is determined according to ISO 5013-1985.

2.3.3. SEM Micrograph. Cell size of foam nanocomposites and MWCNT distribution were observed using a Field Emission Scanning Electron Microscope (FE-SEM) under a voltage of 80 kV and magnifications 30 and 50,000. Necessarily, samples were coated with silver to improve the qualification of SEM images at high magnification.

2.3.4. Compressive Strength. The compression tests were conducted according to ASTM D1621 at the crosshead speed of 10 mm/min using Zwick Z2.5 instrument (Germany).

2.3.5. Water Uptake. The water uptake of PU foam nanocomposites is determined according to ISO 5013-1985.

2.3.6. Volume Resistivity. Volume resistivity is determined on the Takeda TR8401 machine (Japan) with DC voltage of 100 V at 25°C and a humidity of 50%.

2.3.7. Thermal Conductivity. The thermal conductivity measurements of the foams were carried on a THB 500 (Linseis, Germany) with the range from 0.01 to 100 W/m·K^{-1} at 20°C. Measurements were made under steady heat flow conditions through the test samples, in accordance with the UNE12667 method.

2.3.8. Heat of Absorption of Foam. The absorber thermometric system (as seen in Figure 1) is a vacuum chamber connected to 250 W infrared light inside. Samples were placed in the chamber with the distance of 390 mm from light source. The temperatures of irradiated surface, nonirradiated surface, and inside sample were collected to measure the heat absorption ratio.

3. Results and Discussion

3.1. FTIR Spectra of Original MWCNTs, Acid-Treated MWCNTs, and Aniline-Modified MWCNTs. FTIR spectra of original, acid, and aniline-modified MWCNTs are shown in Figure 2. For original MWCNTs, the peak at 1628 cm^{-1} is characterized for C=C bonding, which related to the original structure of carbon nanotubes. After treatment with nitric acid, there is a new peak at 1717 cm^{-1} corresponding to C=O stretching, indicating the existence of carboxyl groups in treated MWCNTs due to oxidation of HNO$_3$ acid [19].

The characteristic groups of aniline can be observed in the FT-IR spectrum of aniline-modified MWCNTs. Peaks at 3436 cm^{-1} and 3368 cm^{-1} are characterized for -NH$_2$ stretches. Weak peaks at 3037 cm^{-1} and 2924 cm^{-1} are assigned to the C-H bond of the benzene ring in aniline. C-N stretching vibration is appeared at 1262 cm^{-1}. Moreover, a slight shift from 1717 cm^{-1} to 1728 cm^{-1} of the C=O group vibration may be due to the interaction between COOH groups on the surface of acid-treated MWCNTs and -NH$_2$ groups of aniline. It could indicate that aniline was successfully attached to MWCNT.

3.2. Effect of MWCNT Contents on the Properties of PU/MWCNT Nanocomposites. The effects of MWCNT contents on the porosity, density, and compressive strength of the PU/MWCNT nanocomposites were studied and are reported in Table 1. In this table, the density of PU foam increased by the presence of MWCNTs. Neat PU has the density of 0.034 g/cm^3 and increases to 0.055 g/cm^3 for the nanocomposite containing 5 wt.% of MWCNTs. The change is consistent with the results of Sinar et al. [3], the density of PU foam/3 wt.% of MWCNT nanocomposites also increased by 11.2% as compared with PU foam. The reduction in the porosity was observed for the PU foam nanocomposites with increasing MWCNT contents. For instance, the porosity reached to 89.7% and 76.32% for PU foam and PU nanocomposites using 5 wt.% of MWCNTs, respectively. The result can be explained by the presence of MWCNTs in PU foam which led to the increase in the viscosity of precursor solution that prevented the formation and growth of bubble during foam preparation. Therefore, the higher MWCNT content was introduced in PU foam, the lower porosity was formed in its structure.

Figure 1: Absorber thermometric system.
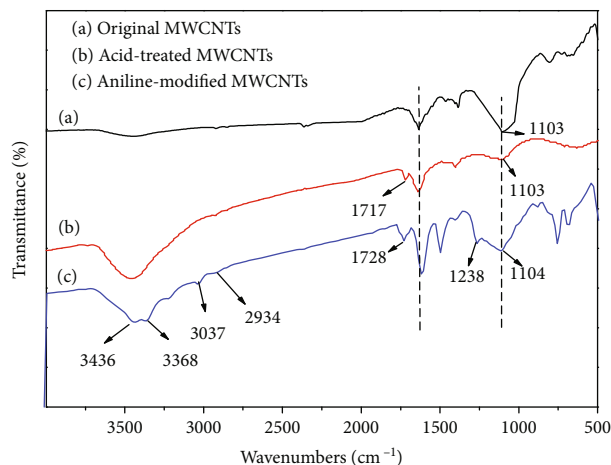
Figure 2: FT-IR spectra of original, acid-treated, and aniline-modified MWCNTs.

Table 1: Density, porosity, and compressive strength of PU/MWCNT foam nanocomposites at various MWCNT contents.

MWCNT contents (wt.%)	Density (g/cm^3)	Porosity (%)	Compressive strength (kPa)
0	0.034	89.7	82.81
1	0.042	82.1	95.26
3	0.048	76.9	111.9
5	0.055	76.3	90.13

The compressive strength of PU foam was also yielded higher than introduction of MWCNTs causing the change in the microstructure of the foam. Neat PU foam has the lowest compressive strength at 82.81 kPa while the PU foam nanocomposite containing 3 wt.% of MWCNTs has the maximum compressive strength at 111.9 kPa. This is due to fine dispersion and good interaction of MWCNTs in PU matrix

at 3 wt.% content. However, the compressive strength of the nanocomposites tends to strongly decrease as MWCNT content exceeds 3 wt.% due to the agglomeration of MWCNTs on PU matrix [3, 20]. Thus, 3 wt.% of MWCNT content was selected for the next investigation.

3.3. The Effect of Modified MWCNTs on the Properties of PU/MWCNT Nanocomposites.

To determine the effect of aniline modification, the properties of PU nanocomposites using 3 wt.% of MWCNTs with and without aniline were studied and are shown in Table 2. As seen in Table 2, the nanocomposites containing aniline-modified MWCNTs reveal the high density and low porosity in comparison with that containing unmodified MWCNTs. This may be due to the presence of aniline on the surface of MWCNTs that could enhance the dispersibility of MWCNTs and the viscosity of PU foam. The fine dispersion of modified MWCNTs in PU matrix also caused the slight increase in compressive strength (3%) and the decrease in water uptake (13.4%) as compared to the PU/unmodified MWCNT nanocomposites. On the one hand, the decrease in water uptake is attributed to hydrophobic surface of MWCNTs after modification with aniline. On the other hand, the reduction of porosity of the nanocomposites is also the reason for this decrease. It is worth noting that aniline improves the electrical conductivity that could also enhance thermal conductivity for PU/modified MWCNT nanocomposites as compared to PU/unmodified MWCNT nanocomposites [8].

3.4. Thermal Properties of PU Foam Nanocomposites

3.4.1. Heat of Absorption.

The temperature at surface of samples when exposed under a constant light source has been used to determine the heat absorption capacity of the samples. Figure 3 reveals the temperature change as a function of the exposing time for the nanocomposites with different modified MWCNTs concentrations.

The heat absorption process can be assumed by the following equations [21, 22]:

$$\text{Absorption process} : Q = E \cdot S \cdot k_1,$$

$$\text{Deabsorption process} : P = \alpha(T_1 - T_0),$$

$$\text{when the surface temperature remains constant} : Q = P$$

$$\text{Lead to } \frac{\alpha(T_1 - T_0)}{E \cdot S},$$

$$\text{Therefore, } \frac{k_1}{k_0} = \frac{T_1 - T_0}{T_2 - T_0},$$

$$(1)$$

where Q is the absorbing heat, P is the radiant heat, S is the surface area of sample, k_1 is the heat absorption constant of PU/MWCNT nanocomposite, k_2 is the heat absorption constant of PU reference, E is the radiant energy of light sources, α is the coefficient of heat absorption of the medium, T_0 is the room temperature (°C), T_2 is the saturated temperature of PU reference (°C), and T_1 is the saturated temperature of PU/MWCNT nanocomposite (°C).

TABLE 2: The properties of PU nanocomposites using 3 wt.% MWCNTs with and without modification.

Properties	Unit	Unmodified sample	Modified sample
Density	g/cm^3	0.048	0.050
Porosity	%	76.9	75.0
Compressive strength	kPa	111.9	115.3
Water uptake	%	68.8	59.6
Volume resistivity	Ω·m	0.75×10^{12}	1.67×10^9
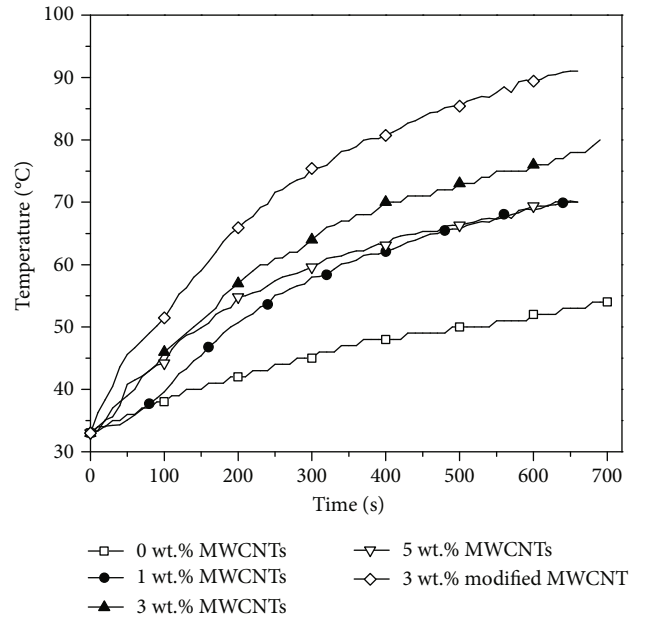
FIGURE 3: Temperature on the surface of the foam nanocomposites with different MWCNT contents.

As observation from Figure 3, the surface temperature of the samples increased rapidly in the first 400 seconds, then slowly reached a steady state over the last 300 seconds. Original PU foam showed the slow increase in temperature and reached the maximum value of 50°C after 700 seconds of testing. This is probably due to the high thermal insulation and less heat absorption of PU. In contrast, surface temperature of the foam nanocomposites has been dramatically changed with addition of 3 wt.% of modified MWCNTs and reached the maximum value of 90°C after 700 testing seconds. However, if the filler content is higher than 3 wt.%, the surface temperature of the foam nanocomposites is no longer enhanced. In this case, the addition of MWCNTs exceeds the fine dispersibility in PU matrix. Consequently, the heat-absorbing effect of the MWCNTs on the surface samples decreased. Thus, as MWCNTs were modified with aniline, the compatibility between dispersive phase and polymer matrix was improved. As a result, temperature at the surface of the nanocomposites containing 3 wt.% of modified MWCNTs is higher than that of unmodified samples.

From the obtained data of temperature on surface samples, the heat absorption ratio (as compared with PU foam)

TABLE 3: Heat absorption ratio and temperature deviation of PU/MWCNT nanocomposites with various MWCNT contents.

Properties	Foam nanocomposite				
	0 wt.% unmodifed MWCNTs	1 wt.% unmodifed MWCNTs	3 wt.% unmodifed MWCNTs	3 wt.% modified MWCNTs	5 wt.% unmodifed MWCNTs
Heat absorption ratio (k_1/k_0)	1.00	2.30	2.75	3.23	2.49
Temperature deviation (ΔT (°C))	31.4	27.5	24.8	16.9	20.8

and temperature deviation between irradiated and nonirradiated surfaces of samples were calculated and are shown in Table 3. The incorporation of MWCNTs into PU foam can enhance the heat absorption ratio from 2.30 to 2.75 as filler content changed from 1 wt.% to 3 wt.%, and then, it was decreased to 2.49 for the sample using 5 wt.% of modified MWCNTs. The higher heat absorption ratio was achieved for the PU/modified MWCNT samples meaning that the temperature deviation is the lowest for the PU/modified MWCNT nanocomposites as compared with PU matrix or PU/unmodified MWCNT nanocomposites. The obtained results demonstrated that MWCNTs could promote the heat conduction within the bulk of nanocomposites, especially modified MWCNTs.

3.4.2. Study of Thermal Conductivity. Figure 4 shows the changes in thermal conductivity of the foam nanocomposites as a function of MWCNT contents. The thermal conductivity for the PU foam is 0.035 W/m·K. This value increased to 0.072 W/m·K for PU/unmodified MWCNT nanocomposites as MWCNT contents changed in the range of 0–5 wt.%. The change in thermal conductivity is in agreement with the results of Santiago-Calvo et al. [18]. The authors investigated the effects of different MWCNT contents (0.1-0.4 wt.% loading) and reported that thermal conductivity could remarkably improve as compared with PU foam at high contents of nanoparticles due to an increase of the heat conduction through the solid phase. The addition of nanoparticles enhanced the density of foam resulting in an enhancement in the thermal conductivity of the solid matrix. Regarding the thermal conductivity, Yan et al. [23] also explained the formation of an interconnected network of the fibers at the high content with polymer matrix could lead to an increase of the conductivity of the solid matrix. This suggests that good dispersion and compatibility between the matrix and the filler give a positive effect for the thermal conductivity of the material. As seen in Figure 4, the incorporation of modified MWCNTs with PU foam shows the significant improvement in thermal conductivity as compared with the unmodified nanoparticles. The obtained results showed that modification with aniline could promote the dispersibility of MWCNTs in PU matrix, leading to the improvement in the thermal conductivity of the foam nanocomposites.

3.5. Morphology of Foam Nanocomposites and MWCNT Distribution in the Foam. Microstructures of the PU foam and foam nanocomposites were determined by scanning electron microscopy analysis (SEM). The change in morphology of the foam nanocomposites at various MWCNT contents is shown in Figure 5 and summarized in Table 4. The micrographs of PU foam and its nanocomposites
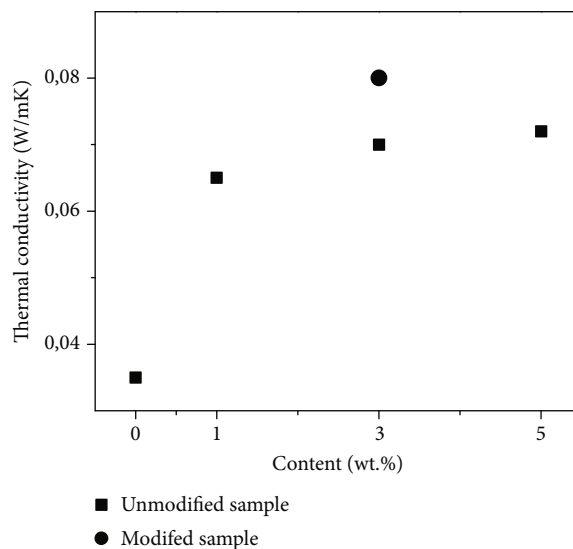
FIGURE 4: Thermal conductivity of modified 3 wt.% MWCNT nanocomposite and unmodified nanocomposites at various MWCNT contents.

showed a cellular structure with spherical and polyhedral shape. The cell distribution was somewhat uniform for PU foam and became less uniform after adding nanoparticles into PU foam. Average cell size calculated from micrograph of samples showed that the changes in cell size are obvious as shown in Table 4. The cell size of the pure PU foam is 714 μm, whereas the foam nanocomposites with 1 and 3 wt.% of unmodified MWCNTs has a cell size of 616 and 380 μm, respectively. However, the decrease in cell size was also recorded for sample containing 3 wt.% of modified MWCNTs, where cell size is 240 μm. It means that the cell size of the modified sample is finer than that of the unmodified sample at the same filler content.

In general, a cell size reduction of PU foam caused by the presence of nanoparticles has been reported previously [4]. MWCNTs played as a nucleation point for cell formation and growth of PU foam [24], leading to the creation of a larger number of cells; thus, the cell size became smaller. On the other hand, the viscosity of the foam nanocomposites seems to be higher than PU foam due to the incorporation of MWCNTs with PU matrix which limits the cell growth and results in smaller cell sizes when compared to the PU foam [4].

The distribution of MWCNTs with and without aniline modification in the PU matrix can be observed from SEM images at the higher magnification. It can be seen from Figure 6(a) that a uniform dispersion of modified MWCNTs

(a)

(b)

(c)

(d)
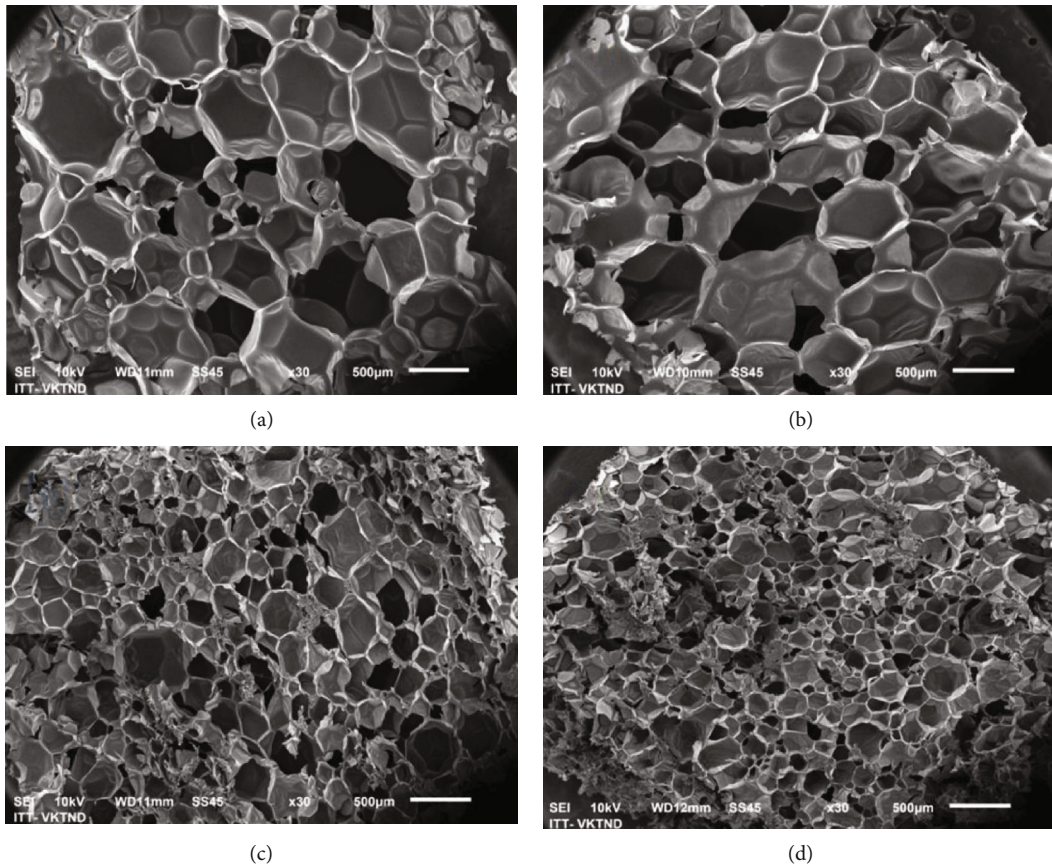
FIGURE 5: SEM micrographs of (a) original PU foam and foam nanocomposites containing (b) 1 wt.% MWCNTs, (c) 3 wt.% MWCNTs, and (d) 3 wt.% modified MWCNTs with low magnification (30 times).

TABLE 4: Microstructural results of foam nanocomposites.

Type of property	Neat PU	1 wt.% unmodifed MWCNTs	3 wt.% unmodifed MWCNTs	3 wt.% modified MWCNTs
Cell type	Closed	Closed	Closed	Closed
Symmetry of structure	Asymmetric	Asymmetric	Asymmetric	Asymmetric
Cell size (μm)	714	616	380	240

(a)

(b)
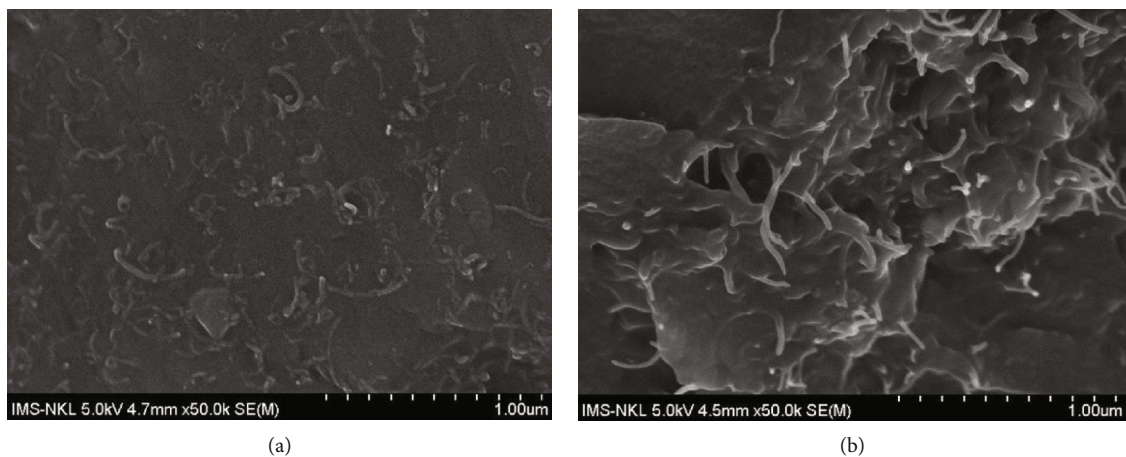
FIGURE 6: High magnification SEM micrograph of foam containing (a) 3 wt.% MWCNTs and (b) 3 wt.% modified MWCNTs.

was observed on the PU cell edges (not detected on the cell walls). However, the phase separation between the filler and matrix is quite clear due to the differences in the hydrophilic properties of PU and modified MWCNTs. The presence of aniline on the surface of MWCNTs improved the compatibility with PU matrix, which led to the generation of smaller cells as compared to the foam containing unmodified MWCNTs (Figure 6(b)).

4. Conclusion

The MWCNTs were successfully modified with aniline through the interaction between anilines with carboxylated MWCNTs. PU foam nanocomposites reinforced with unmodified and modified MWCNTs with different concentrations were prepared by a moulding process. The changes in properties of PU foam as introducing MWCNTs showed that the presence of MWCNTs led to an increase in density and a reduction on porosity due to the nanoparticle addition enhances the nucleation point for cell formation and growth of PU foam. The compressive strength of foam nanocomposite achieved the maximum value for the sample containing 3 wt.% of unmodified MWCNTs. As compared to unmodified samples, the foam nanocomposites containing 3 wt.% of modified MWCNTs show better results. The compressive strength of the PU/modified MWCNT nanocomposites increased from 111.9 kPa to 115.3 kPa, while water uptake significantly decreased from 68.8% to 59.6% as compared to the unmodified sample. A similar improvement in thermal conductivity was also seen for the nanocomposites containing modified MWCNTs with an increase from 0.072 W/m·K to 0.08 W/m·K. Moreover, SEM micrograph showed that the addition of modified MWCNTs affected the cellular size of foam more clearly than the unmodified filler. The average cell size of the foam decreased with increasing nanoparticle content, and the lowest value was 240 μm for the nanocomposite containing 3 wt.% of modified MWCNTs. A possible explanation of this result is that modified MWCNTs could be better dispersed in the PU matrix than the unmodified filler due to better chemical interactions of the modified nanoparticles with the PU matrix. It is worth noting that high temperature could be achieved at surface for the foam nanocomposites under light source opening up possibilities for drying agricultural products.

Data Availability

The data used to support this study can be available upon request to the corresponding author.

Conflicts of Interest

The authors declare that they have no conflicts of interest

Acknowledgments

References

[1] G. Shuzhong, Z. Chao, W. Weizhi et al., "Preparation and characterization of polyurethane/multiwalled carbon nanotube composites," *Journal of Polymers & Polymer Composites*, vol. 16, no. 8, pp. 471–478, 2008.

[2] M. C. Saha, E. Kabir Md., and S. Jeelani, "Enhancement in thermal and mechanical properties of polyurethane foam infused with nanoparticles," *Journal of Materials Science and Engineering*, vol. 479, no. 1-2, pp. 213–222, 2008.

[3] A. A. Sinar, Z. Firuz, M. A. N. Azni, A. Z. N. Hidayah, M. A. Hazizan, and H. A. Sahrim, "Compression test and energy absorption of polyurethane/multi walled carbon nanotubes foam composites," *Journal of Materials Science Forum*, vol. 819, pp. 246–250, 2015.

[4] L. Madaleno, R. Pyrz, A. Crosky et al., "Processing and characterization of polyurethane nanocomposite foam reinforced with montmorillonite-carbon nanotube hybrids," *Composites Part A: Applied Science and Manufacturing*, vol. 44, pp. 1–7, 2013.

[5] P. Mondal and D. V. Khakhar, "Rigid polyurethane–clay nanocomposite foams: preparation and properties," *Journal of Applied Polymer Science*, vol. 103, no. 5, pp. 2802–2809, 2007.

[6] F. Zhang, Z. Xiao, J. Huang, Z. Su, H. Zhang, and Q. Zhang, "One-pot synthesized polyurethane-based nanocomposites filled by original rectorite with enhanced strength and elongation," *Journal of Wuhan University of Technology-Materials Science Edition*, vol. 26, no. 3, pp. 483–490, 2011.

[7] D. L. Reid, R. Draper, D. Richardson et al., "In situ synthesis of polyurethane–TiO2 nanocomposite and performance in solid propellants," *Journal of Materials Chemistry A*, vol. 2, no. 7, p. 2313, 2014.

[8] V. Dolomanova, J. C. M. Rauhe, L. R. Jensen, R. Pyrz, and A. B. Timmons, "Mechanical properties and morphology of nano-reinforced rigid PU foam," *Journal of Cellular Plastics*, vol. 47, no. 1, pp. 81–93, 2011.

[9] L. Zhang, E. D. Yilmaz, J. Schjødt-Thomsen, J. C. Rauhe, and R. Pyrz, "MWNT reinforced polyurethane foam: processing, characterization and modelling of mechanical properties," *Composites Science and Technology*, vol. 71, no. 6, pp. 877–884, 2011.

[10] D. Yan, L. Xu, C. Chen, J. Tang, X. Ji, and Z. Li, "Enhanced mechanical and thermal properties of rigid polyurethane foam composites containing graphene nanosheets and carbon nanotubes," *Polymer International*, vol. 61, no. 7, pp. 1107–1114, 2012.

[11] Z. Xu, X. Tang, A. Gu, and Z. Fang, "Novel preparation and mechanical properties of rigid polyurethane foam/organoclay nanocomposites," *Journal of Applied Polymer Science*, vol. 106, no. 1, pp. 439–447, 2007.

[12] R. H. Baughman, A. A. Zakhidov, and W. A. de Heer, "Carbon nanotubes the route toward applications," *Science*, vol. 297, no. 5582, pp. 787–792, 2002.

[13] M. Dresselhaus and P. Avouris, *Carbon Nanotubes: Synthesis, Structure Properties and Applications*, Springer, Berlin, 2001.

[14] X. B. Peng, T. X. Liu, M. Wang, W. Huang, and W. D. Zhang, "Carbon nanotubes reinforced polymer composites," *Chemistry Online*, vol. 69, p. w016, 2006.

[15] S. Guo, C. Zhang, W. Wang et al., "Preparation and characterization of polyurethane/multiwalled carbon nanotube

composites," *Polymers and Polymer Composites*, vol. 16, no. 8, pp. 501–507, 2008.

[16] V.-D. Dao and H.-S. Choi, "Carbon-based sunlight absorbers in solar-driven steam generation devices," *Global Challenges*, vol. 2, no. 2, 2018.

[17] R. Singh and S. V. Torti, "Carbon nanotubes in hyperthermia therapy," *Advanced Drug Delivery Reviews*, vol. 65, no. 15, pp. 2045–2060, 2013.

[18] M. Santiago-Calvo, J. Tirado-Mediavilla, J. C. Rauhe et al., "Evaluation of the thermal conductivity and mechanical properties of water blown polyurethane rigid foams reinforced with carbon nanofibers," *European Polymer Journal*, vol. 108, pp. 98–106, 2018.

[19] C. Zhao, L. Ji, H. Liu et al., "Functionalized carbon nanotubes containing isocyanate groups," *Journal of Solid State Chemistry*, vol. 177, no. 12, pp. 4394–4398, 2004.

[20] V. R. D. Silva, M. A. Mosiewicki, M. I. Yoshida, M. C. D. Silva, P. M. Stefani, and E. Marcovich, "Polyurethane Foams Based on Modified Tung Oil and Reinforced with Rice Husk Ash II: Mechanical Characterization," *Polymer Testing*, vol. 32, no. 4, pp. 665–672, 2013.

[21] G. F. Nellis and S. A. Klein, *Introduction to Engineering Heat Transfer*, pp. 6-7, 2020.

[22] M. Bahrami, *Heat Transfer & Thermodynamics*, Spring 2005 ECE 309 University of Waterloo, 2005.

[23] D.-X. Yan, K. Dai, Z.-D. Xiang, Z.-M. Li, X. Ji, and W.-Q. Zhang, "Electrical conductivity and major mechanical and thermal properties of carbon nanotube-filled polyurethane foams," *Journal of Applied Polymer Science*, vol. 120, pp. 3014–3019, 2011.

[24] L. Madaleno, R. Pyrz, L. R. Jensen et al., "Synthesis of clay–carbon nanotube hybrids: growth of carbon nanotubes in different types of iron modified montmorillonite," *Composites Science and Technology*, vol. 72, no. 3, pp. 377–381, 2012.

WILEY | Hindawi

Research Article

Peroxymonosulfate Activation on a Hybrid Material of Conjugated PVC and TiO₂ Nanotubes for Enhancing Degradation of Rhodamine B under Visible Light

La Phan Phuong Ha,[1,2] **Tran Hong Huy,**[1,2] **Pham Huu Huan,**[1,2] **Nguyen Thi Minh Thu,**[1,2] **Cao Minh Thi** (ID),[3] **and Pham Van Viet** (ID)[1,2]

¹*Faculty of Materials Science and Technology, University of Science, VNU-HCM, 227 Nguyen Van Cu Street, District 5, Ho Chi Minh City 700000, Vietnam*
²*Vietnam National University-Ho Chi Minh City, Linh Trung Ward, Thu Duc District, Ho Chi Minh City 700000, Vietnam*
³*Ho Chi Minh City University of Technology (HUTECH), 475A Dien Bien Phu Street, Binh Thanh District, Ho Chi Minh City 700000, Vietnam*

Correspondence should be addressed to Cao Minh Thi; cmthi@hutech.edu.vn and Pham Van Viet; pvviet@hcmus.edu.vn

Visible-light-driven photocatalysis is a robust technology for amending the negative effect of pollutants on the environment with a minimum energy use. Herein, we describe a simple approach to producing such a photocatalyst by coupling conjugated polyvinyl chloride (cPVC) with the TiO₂ nanotube (TNT) thermolysis method. By activating peroxymonosulfate (PMS) to make a cPVC/TNT/PMS system using visible light as the source, we obtain a significant enhancement in the photocatalytic performance. We show that PMS use at a concentration of 3 mM can fully degrade rhodamine B (RhB) solution at a remarkably high concentration (200 mg L⁻¹) just in 120 min under visible light. The cPVC/TNT/PMS system also shows excellent stability in recycling tests for at least five times. Further, by confining the active species in photocatalytic reactions, we report a thorough understanding of the extent of involvement from those radicals. Our work presents a robust approach to make a high-performance, visible-light-driven photocatalyst, which can be potentially used in practice.

1. Introduction

Photocatalysis technology is a great means of treating environmental pollutants by making direct use of light to generate highly active oxygen species that are more favorable because of the high performance, environmental benefits, and low operating cost [1–4]. For photocatalytic materials to be used widely in practice, the source of the exciting light should be abundantly available (i.e., visible light that accounts for about 43% of the solar radiation and does not require any energy to be produced); the preparation of photocatalysts should also be simple, inexpensive, and robust [5, 6].

Recently, sulfate radical anion- (SO_4^-) induced advanced oxidation reactions that have been successfully used in treating organic pollutants in water [7–9]. In comparison with hydroxyl radical ($^{\cdot}OH$), SO_4^- has a higher reduction potential [10]. Also, SO_4^- has advantages such as pH independence [11], greater oxidation selectivity of organic pollutants, and longer lifetime during the reaction [12]. Peroxymonosulfate (PMS) activation-induced SO_4^- is usually generated via thermolysis, photolysis, photocatalysis, a metallic oxidant, and carbon materials [13–16]. Therein, activation of PMS assisted by a photocatalyst under visible light is environmentally sustainable and simple to perform without additional energy/chemical requirement.

Previous studies have shown that the combination of photocatalytic materials with readily available polymers after being conjugated would lead to the production of barely expensive nanocomposites but having a promising photocatalytic performance [17–23]. For instance, a conjugated polyvinyl chloride- (cPVC-) grafted SnS_2 nanocomposite, having a high photocatalytic performance in the reduction of aqueous Cr(VI) under visible light, was reported [18]. More recently, getting combined PANI and Ag_3PO_4, a highly efficient visible-light-driven photocatalyst with a core@shell structure was prepared [20]. Although visible-light-driven photocatalysts have been extensively reported for years, complex steps in preparation and low efficiency remain a major challenge for such photocatalysts to be used broadly and effectively [24–28]. Noticeably, a recent study has reported a prominently facile approach to produce a nanocomposite of conjugated polyvinyl chloride (cPVC) and TiO_2 nanotubes (TNTs), showing a remarkable photocatalytic performance under visible light [29]. By taking advantage of the ability for mass production of TNT with the abundant availability, chemical stability, and ease in the processing of cPVC, fabrication of cPVC/TNT nanocomposites could potentially be used broadly in practice. Moreover, the introduction of sulfate anion radicals into the reaction system, subsequently activated by the photocatalyst under light irradiation, results in a significant enhancement in the photocatalytic efficiency [8, 30–35]. Thus, the combination of a visible-light-driven photocatalyst with the strong oxidizing capability of SO_4^- radicals can potentially lead to the highest photocatalytic performance of that specific photocatalyst under visible light.

Herein, we use the effectiveness of cPVC/TNT nanocomposites and the introduction of PMS to produce an efficient photocatalyst under visible light. Our setting also demonstrates rational stability for a set of five-repeated rounds of photocatalytic activity. We also determine to what extent SO_4^- radicals played a role in the photocatalytic enhancement in situ via trapping experiments.

2. Experimental

2.1. Materials.
Commercial polyvinyl chloride (PVC), ethylene glycol (EG, 99.8%), tetrahydrofuran (THF, 99.0%), commercial TiO_2 powder (Merck, 99.99%), hydrochloric acid (HCl, China, 37%), sodium hydroxide (NaOH, Merck, 99%), peroxymonosulfate (PMS), potassium iodide (KI, 99.99%), isopropyl alcohol (IPA, C_3H_8O, 99.99%), potassium dichromate ($K_2Cr_2O_7$, 99.99%), *tert*-butanol (TBA; $(CH_3)_3COH$, 99.99%), rhodamine B (RhB, $C_{28}H_{31}ClN_2O_3$), and deionized (DI) water (Puris-Evo water system) were used.

2.2. Synthesis of Materials

2.2.1. Synthesis of TiO_2 Nanotubes (TNTs) via Hydrothermal Method.
The preparation of TNT via a hydrothermal process was reported in our previous works [36, 37]. Accordingly, 1.7 g of commercial TiO_2 powder was mixed with 157 mL of 10 M NaOH solution for a certain time to get a well-dispersed suspension. This mixture of TiO_2 powder and NaOH solution was subsequently transferred into a Teflon

container, closely sealed by a stainless-steel autoclave. The hydrothermal process was operated at a temperature of 135°C for 24 h. The hydrothermally treated mixture was then naturally cooled to room temperature, followed by a pH treatment using HCl and DI water to reach a pH value of 4 and 7, respectively. TNTs were obtained by drying the product at 60°C for several hours.

2.2.2. Synthesis of cPVC/TNT Nanocomposites.
The preparation of cPVC/TNT nanocomposites was reported in our recent work [29]. For preparing cPVC, first, PVC powder was added into a mixture of NaOH and ethylene glycol. Second, the three-component mixture was stirred for 30 min, followed by sonication for a further 30 min. Third, the well-dispersed mixture was transferred into a 3-neck flask, which was subsequently stirred for a certain time before treatment in nitrogen gas at 190°C for 3 h. Finally, cPVC was obtained by extensively washing the treated solution with DI water, followed by a drying step at 60°C. cPVC/TNT samples were then prepared straightforwardly. Different amounts of cPVC were dissolved in 10 mL THF. Subsequently, TNT was added into the cPVC/THF mixtures with the mass ratios (cPVC : TNT) of 10 : 100. The combination was then magnetically stirred for 30 min, which was sonicated for a further 30 min. Lastly, the final products were fully dried at 60°C for 1 h to obtain cPVC/TNT nanocomposites.

2.3. Characterizations.
Transmission electron microscopy (TEM) images were taken on a JEM 1400 at 100 kV to observe the materials' morphology. X-ray diffraction (XRD) patterns were taken using a Bruker D8-Advance 5005 (Cu Kα radiation, $\lambda = 0.154064$ nm) in the range 2θ from 10° to 70° to define the crystal structure of as-prepared materials. Also, Fourier-transform infrared spectroscopy (FTIR) spectra were captured on a JASCO-4700 to detect the vibration of molecules in the region of 480 to 4000 cm^{-1}, which used KBr pellets as the reference.

2.4. Evaluation of Photocatalytic Activity.
We used rhodamine B (RhB) as the organic pollutant in evaluating the photocatalytic degradation of our material. RhB is a water-soluble organic dye and is widely used in the textile industry. RhB can injure human eyes and skin and cause respiratory problems [38]. Furthermore, it induces phototoxicity and shows resistance to biooxidation. Thus, it is important to study the photocatalytic degradation in which RhB is the target pollutant. The photocatalytic tests were performed using 0.1 g of photocatalyst against a 60 mL rhodamine B (RhB) dye solution with a concentration of 200 mg L^{-1}. PMS (0.1 to 5 mM) was added to the RhB dye solution before introducing the photocatalyst. The PMS-activated photocatalyst/RhB mixture was stirred in the dark for 1.5 h to achieve adsorption/desorption. Subsequently, the equilibrated system was illuminated by visible light from a simulated solar light (Osram Ultra-Vitalux 300 W) attached with a UV cutting glass. The entire photocatalytic activities were performed for 3 h. Over intervals of 30 min, a small amount of the suspension was withdrawn, followed by centrifuge at a rapid rate to separate the solution from the suspension. Shortly after, a

UV-Vis spectrophotometer (U2910, Hitachi, Japan) was used to measure the solution's absorption spectrum in the range of 400 nm to 650 nm. The photocatalytic efficiency and the photocatalytic reaction rate were quantitatively calculated via

$$\eta = \frac{C_0 - C_t}{C_0} \times 100\%, \tag{1}$$

where η stands for photocatalytic degradation efficiency of RhB (%), C_0 regards the initial concentration of RhB, and C_t regards the concentration of RhB at time t.

2.5. Radical Trapping Test. The radical trapping experiments, using standard scavengers, including KI, $K_2Cr_2O_7$, IPA, and TBA, were performed to probe the extent of involvement in the photocatalytic reactions of the photogenerated hole, electron, SO_4^-, and $\cdot OH$, respectively. The concentration of the scavenger was 3 mM. The experimental conditions for these trapping experiments were like those described in the photocatalytic activity tests.

2.6. Evaluation of Photocatalytic Stability. After the first round of the photocatalytic activity, the photocatalyst was collected from the suspension by centrifuge at high speed and dried at 60°C. Subsequently, this collected photocatalyst was repeatedly used for further five photocatalytic activity tests to quantify the sample's stability against photocorrosion, one-time use problem, and so on.

3. Results and Discussion

Structural features of the as-prepared nanocomposite are characterized (Figure 1). The FTIR profile of the cPVC/TNT nanocomposite shows a prominent presence of a vibration peak at 1628 cm^{-1}, representing C=C bonds in cPVC [29, 39], and the well-known vibration of the Ti–O–Ti bond at around 500 cm^{-1} [40] (see Figure 1(a)). Also, this sample's XRD pattern shows the presence of anatase and rutile phase signals of TiO$_2$ (JCPDS No. 21–1272 and No. 65-6231) and a typical diffraction peak of cPVC at 25° (Figure 1(b)). Thus, FTIR and XRD results have evidenced success in the fabrication of the cPVC/TNT nanocomposite. The XRD pattern also indicates a good crystallinity of the cPVC/TNT nanocomposite, which is potentially favorable for photocatalytic activity.

Changes in the morphology of TNTs upon the combination with cPVC using TEM images are presented in Figure 2. TNT has a typical hollow morphology with an outer diameter of about 9.5 nm (Figures 2(a) and 2(b)). Further morphological details of TNT, prepared via the hydrothermal method, are previously reported [41]. Upon combination with cPVC, the TNT's relatively smooth surface becomes a rough surface, which is covered with nanoscale spherical objects (Figures 2(c) and 2(d)). Those nanoscale spherical objects could be attributed to the addition of cPVC to the surface of TNT, forming a nanocomposite. Importantly, the combination of cPVC and TNT has been successfully performed without damaging TNT's unique morphology.

Photocatalytic properties of the cPVC/TNT nanocomposite against the RhB solution upon PMS activation under visible light is studied (Figure 3). It is critical to note that the photocatalytic activity of the cPVC/TNT nanocomposite has been shown to outperform that of cPVC and TNT samples completely under visible light [29]; it is thus not necessary to reconsider it in this work. A referencing test is done with no photocatalyst for 180 min of irradiation, showing no self-degradation due to the light sensitizing effect (Figure 3(a)). Also, using a RhB solution with a high concentration (200 mg L^{-1}), we intentionally constrained the photocatalytic activity of the cPVC/TNT nanocomposite, leading to no visible light degradation of RhB. Subsequently, PMS with concentration varying from 0.1 to 5 mM is added into the photocatalytic system. Upon adding PMS, the photocatalytic performance of the cPVC/TNT nanocomposite prominently increases with a greater amount of PMS. The cPVC/TNT nanocomposite's photocatalytic activity seems to reach the highest performance upon being activated by PMS at the concentration of 3 mM, which takes only 120 min to degrade the pollutant fully. Also, the absorption spectra of RhB show a great decrease in its intensity during 120 min of reaction without shifting its typical peak, which indicates excellent photocatalytic performance (Figure 3(b)). In addition, a greater amount of PMS (4 and 5 mM) also shows good performance, but both take a longer time (150 min) to degrade RhB fully. Generally, the amount of generated $\cdot OH$ and SO_4^- directly depends on the PMS concentration. As shown in Figure 3(a), the degradation rate of RhB is accelerated when increasing the PMS concentration from 0.1 to 3 mM. However, when the PMS concentration is increased from 3 to 5 mM, a slight reduction in RhB degradation is observed. Two reasons could interpret this result. First, an optimal PMS could serve as electron acceptors, leading to the improvement of the photocatalytic performance, whereas the photogenerated electrons might not be readily sufficient to activate the excessive PMS [30]. Second, a typical reaction could be involved in the process that happens between excessive PMS and SO_4^- radicals to give rise to the generation of SO_5^- that has a lower oxidizing ability [42], leading to the decreased performance against RhB (see equation (2)). Thus, our results show that the cPVC/TNT nanocomposite's photocatalytic performance can be enhanced significantly by PMS activation with an optimal amount of PMS at the concentration of 3 mM.

$$SO_4^- + HSO_5^- \rightarrow SO_5^- + SO_4^- + H^+ \tag{2}$$
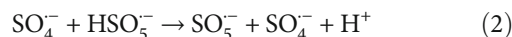
To have a better comparison with the state-of-the-art, we provide an extensive list of the current photocatalytic systems (Table 1). Key factors such as pollutant indicator, concentration of pollutants, optimal PMS concentration, amount of photocatalyst, and excitation source are tabulated. In summary, our system, cPVC/TNT/PMS/Vis, has shown competitive photocatalytic activity compared to a wide range of materials. We have used a low amount of photocatalyst in addition to a below-average PMS concentration to fully

(a)

(b)
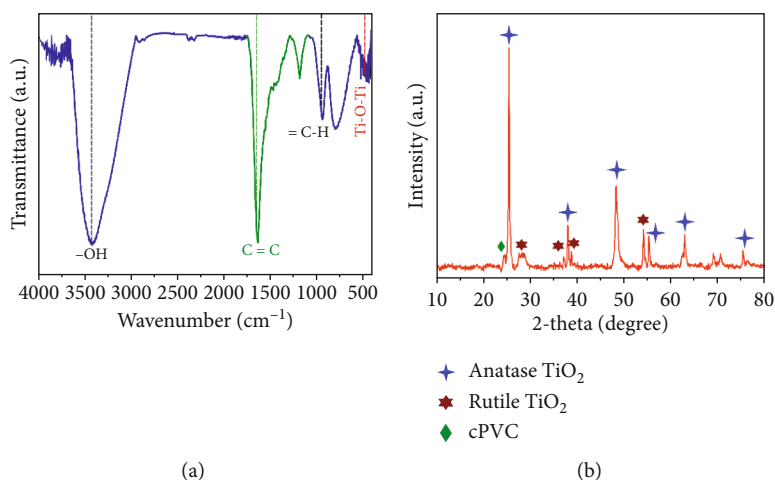
Figure 1: (a) FTIR spectrum and (b) XRD pattern of cPVC/TNT nanocomposite.

(a)

(b)

(c)

(d)
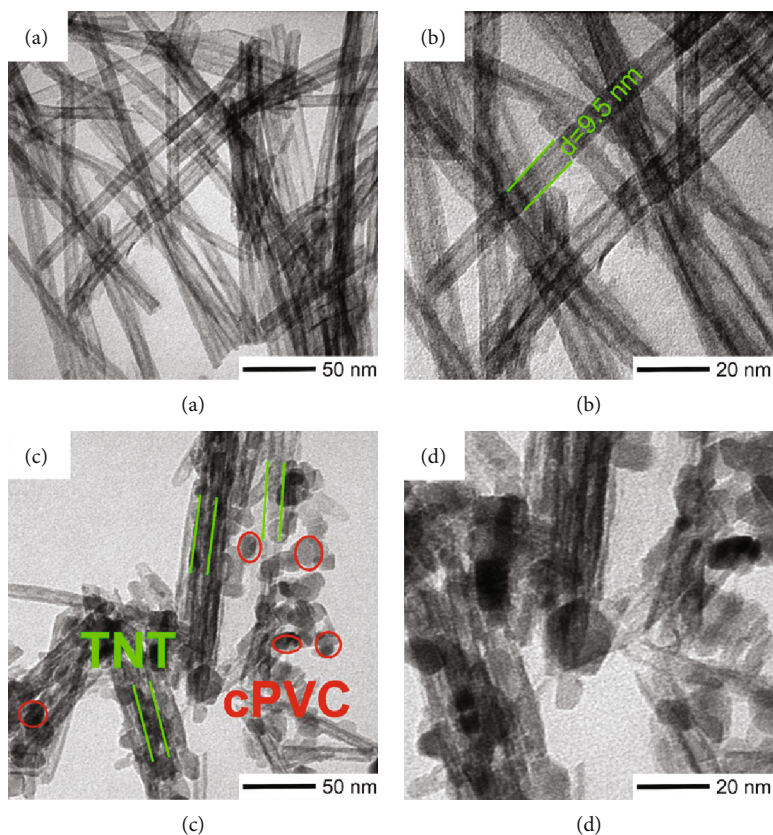
Figure 2: TEM image of (a, b) TNTs and (c, d) cPVC/TNT nanocomposite.

degrade RhB at a remarkably high concentration, which only uses visible light as the irradiation source.

In addition to the performance, photocatalysts having a certain benefit of recycling would allow them to be used widely in practice. By recycling the used photocatalyst, we test the photocatalytic performance of our cPVC/TNT nanocomposite against RhB with PMS's addition at the concentration of 3 mM for five repeated rounds (Figure 3(c)). Our results show that the photocatalytic performance decreases gradually after each round, which would be attributed to

the photocatalyst's loss in the postprocessing steps. However, even after five rounds of the repeated photocatalytic tests, the efficiency was still greater than 70%, which is a good merit given the remarkably high concentration of RhB as well as the use of visible light only.

Although we have shown that at a high concentration of RhB the cPVC/TNT nanocomposite's photocatalytic activity is strictly constrained, the introduction of sulfate radicals is the key factor to activate the reaction (Figure 3(a)). However, to develop a deep understanding of all radical species' extent

(a)

(b)

(c)

(d)
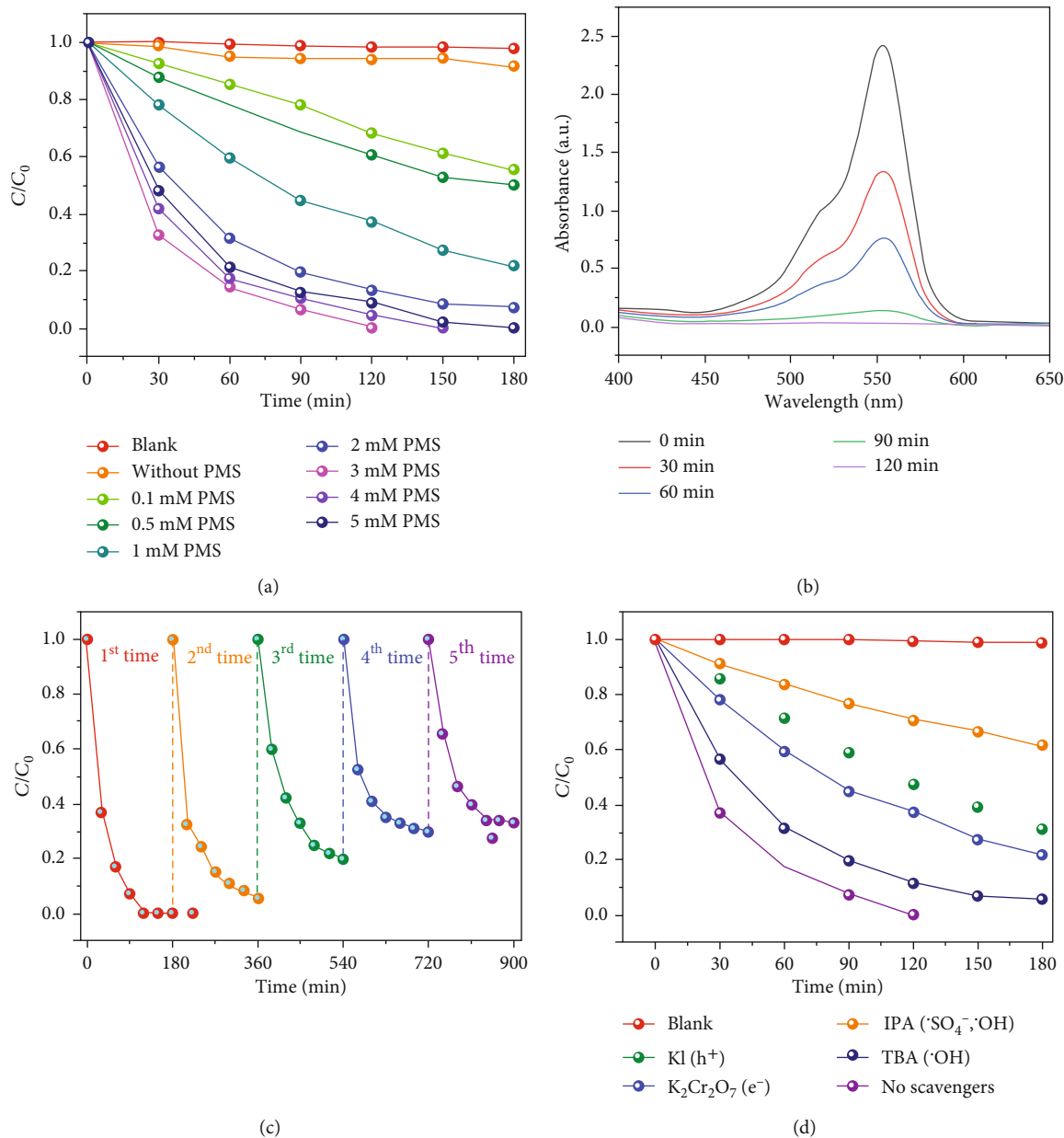
FIGURE 3: (a) Photocatalytic degradation of the cPVC/TNT nanocomposite against RhB upon PMS activation with a concentration varied from 0.1 mM to 5 mM under visible light. (b) Absorption spectra of RhB of the cPVC/TNT nanocomposite after being activated with PMS at a concentration of 3 mM during the photocatalytic reaction. (c) The photocatalytic performance of the cPVC/TNT nanocomposite after being recycled five repeated times. (d) Radical trapping test results.

of involvement during the photocatalytic reaction upon being activated by PMS, a series of trapping tests is conducted. The involvement of radical species in photocatalytic activity of the cPVC/TNT nanocomposite upon PMS activation can be classified into three groups (Figure 3(d)). The first group (using KI and $K_2Cr_2O_7$ as scavengers) regards the partial involvement of photogenerated electrons and holes, which shows a slight decline in the photocatalytic performance. This slight reduction has resulted from the partial loss in starting reactions (both electrons and holes can activate sulfate radicals), explaining the reason for the photocatalytic activity still present despite the absence of those

electrons or holes. There is a relatively higher loss in the photocatalytic activity in trapping holes than trapping electrons, which contrasts with previous works using TNT materials [41]. This result can be explained via the supposedly higher amount of SO_4^- which can be produced from holes in comparison with electrons (see equations (4), (5), (6), (7)). The second group is with regard to the involvement of ·OH groups, which is usually the main factor in semiconductor-induced photocatalytic reactions. Our results show that by confining the activity of ·OH groups, using TBA, the photocatalytic performance on the cPVC/TNT nanocomposite upon PMS activation is affected negligibly (Figure 3(d)). This result

TABLE 1: A comparison of photocatalytic activity against RhB between current systems having been assisted by PMS activation.

Catalyst system	Pollutant conc. ($mg\,L^{-1}$)	PMS conc. (mM)	Catalyst dosage ($g\,L^{-1}$)	Irradiation time (min)	Efficiency (%)	Ref.
$BiFeO_3$/PMS/Vis	5	5.0	1.0	40	60	[43]
Fe_3O_4/PMS/UV	383	12.0	5.0	120	80	[44]
$BiVO_4$/PMS/Vis	10	1.0	0.5	60	97	[45]
$CoFe_2O_4$/TNT/PMS/Vis	100	4.0	0.2	60	100	[46]
Mn_3O_4/ZIF-8	10	0.3	0.3	60	100	[47]
α-MnO_2/palygorskite/PMS/Vis	20	0.1	0.1	300	100	[48]
$CuBi_2O_4$/PMS/Vis	25	0.5	0.8	180	100	[49]
Fe-Co/PMS/UV	20	0.25	0.2	20	100	[50]
rGO/CoPc/PMS/Vis	120	0.07	0.5	40	100	[51]
cPVC/TNTs/Vis	200	3.0	0.1	120	100	This study
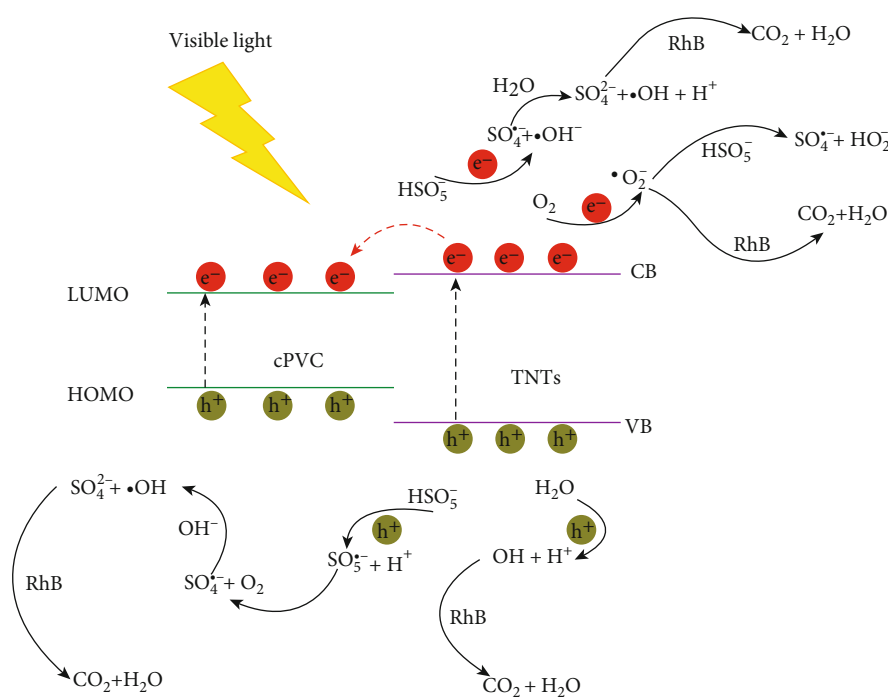
FIGURE 4: A schematic illustration of the photocatalytic degradation mechanism upon activation by PMS under visible light.

confirms the fact that in PMS-activated photocatalytic reactions, the role of $\cdot$OH groups is not the key in comparison to that of SO_4^- groups. The third group presents a case of strong confinement by trapping both SO_4^- and $\cdot$OH groups by using IPA. Our results show that the photocatalytic performance has been significantly decreased in this case.

The mechanism for the photocatalytic activity of the cPVC/TNT/PMS system under visible light is schematically illustrated in Figure 4. In the cPVC/TNT/PMS system, electrons generated from the conduction band (CB) could be used by dissolved oxygen or directly caught by the adsorbed PMS in which PMS is activated to produce SO_4^- (see equations (8) and (9)). Following this process is the enhanced sep-

aration of photogenerated electrons and holes. The remaining holes in the valence band (VB) could also directly oxidize pollutants due to its strong oxidation ability. Also, SO_4^- radicals can bring out radical interconversion reactions to yield $\cdot$OH by the reaction between SO_4^- and OH^- (see equation (10)). In our cPVC/TNT/PMS system, the photogenerated holes play a more important role than photogenerated electrons, which can be highlighted in two aspects. First, the photogenerated holes can oxidize RhB directly. Second, SO_5^- radicals with the lower oxidation capacity are also generated through the combination of PMS and holes (equation (6)), and the generated SO_5^- slightly contributed to $SO_4^-/\cdot$OH production by its self-sacrificing reactions (equation (7)).

Thus, more photogenerated carriers are effectively separated, and more electrons are transferred to participate in the photocatalytic reactions, which facilitates the PMS activation to increase further SO_4^-/OH. As a result, main active species such as holes (VB), $\cdot O_2^-$, $\cdot OH$, and SO_4^- have contributed to the excellent catalytic activity in the developed cPVC/TNT/PMS system under visible light (see equation (11) and Figure 4), and pollutants are readily degraded into smaller intermediates and finally into CO_2 and H_2O.

$$cPVC/TNTs + h\nu \rightarrow cPVC/TNTs\left(e_{CB}^- + h_{VB}^+\right) \quad (3)$$

$$HSO_5^- + e_{CB}^- \rightarrow SO_4^- + OH^- \quad (4)$$

$$SO_4^- + H_2O \rightarrow SO_4^{2-} + \cdot OH + H^+ \quad (5)$$

$$HSO_5^- + h_{VB}^+ \rightarrow SO_5^- + H^+ \quad (6)$$

$$SO_5^- \rightarrow 2SO_4^- + O_2 \quad (7)$$

$$HSO_5^- + \cdot O_2^- \rightarrow SO_4^- + HO_2^- \quad (8)$$

$$HSO_5^- + h\nu \rightarrow SO_4^- + \cdot OH \quad (9)$$

$$SO_4^- + OH^- \rightarrow SO_4^{2-} + \cdot OH \quad (10)$$

$$h_{VB}^+/\cdot O_2^-/\cdot OH/SO_4^- + RhB \rightarrow degradation\ products \quad (11)$$
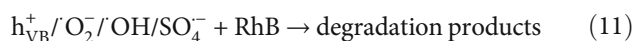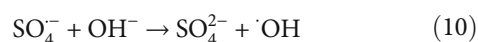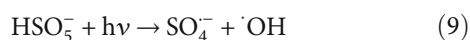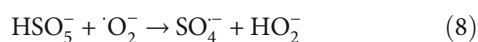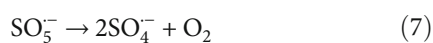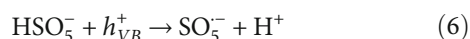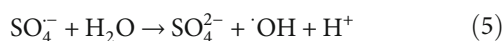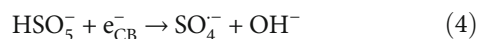
4. Conclusions

In summary, we have prepared a visible-light-driven photocatalyst by combining conjugated polyvinyl chloride and TiO_2 nanotubes via a simple thermolysis method. The introduction of PMS at the concentration of 3 mM has significantly enhanced the photocatalytic performance of the nanocomposite, which is also photostable and recycled with good performance. By confining the active radicals, we have determined that SO_4^- radicals are the key factor for enhancing the photocatalytic performance. Also, photogenerated holes are greater than photogenerated electrons in the extent of involvement. Production of a high-performance photocatalyst under visible light via a simple, inexpensive process will lead to wide use in practice.

Data Availability

The data used to support the findings of this study are available from the corresponding author upon request.

Conflicts of Interest

The authors declare that they have no conflicts of interest.

Authors' Contributions

La Phan Phuong Ha and Tran Hong Huy contributed equally to this work.

Acknowledgments

References

[1] M. A. Fox and M. T. Dulay, "Heterogeneous photocatalysis," *Chemical Reviews*, vol. 93, no. 1, pp. 341–357, 1993.

[2] M. R. Hoffmann, S. T. Martin, W. Choi, and D. W. Bahnemann, "Environmental applications of semiconductor photocatalysis," *Chemical Reviews*, vol. 95, no. 1, pp. 69–96, 1995.

[3] C. Xu, P. R. Anusuyadevi, C. Aymonier, R. Luque, and S. Marre, "Nanostructured materials for photocatalysis," *Chemical Society Review*, vol. 48, no. 14, pp. 3868–3902, 2019.

[4] T. H. Huy, B. D. Phat, C. M. Thi, and P. Van Viet, "High photocatalytic removal of NO gas over SnO_2 nanoparticles under solar light," *Environmental Chemistry Letters*, vol. 17, no. 1, pp. 527–531, 2019.

[5] T. P. Yoon, M. A. Ischay, and J. Du, "Visible light photocatalysis as a greener approach to photochemical synthesis," *Nature Chemistry*, vol. 2, no. 7, pp. 527–532, 2010.

[6] R. Asahi, T. Morikawa, T. Ohwaki, K. Aoki, and Y. Taga, "Visible-light photocatalysis in nitrogen-doped titanium oxides," *Science*, vol. 293, no. 5528, pp. 269–271, 2001.

[7] M. Ahmad, A. L. Teel, and R. J. Watts, "Mechanism of persulfate activation by phenols," *Environmental Science & Technology*, vol. 47, no. 11, pp. 5864–5871, 2013.

[8] Y. Y. Ahn, E. T. Yun, J. W. Seo et al., "Activation of peroxymonosulfate by surface-loaded noble metal nanoparticles for oxidative degradation of organic compounds," *Environmental Science & Technology*, vol. 50, no. 18, pp. 10187–10197, 2016.

[9] G. P. Anipsitakis and D. D. Dionysiou, "Degradation of organic contaminants in water with sulfate radicals generated by the conjunction of peroxymonosulfate with cobalt," *Environmental Science & Technology*, vol. 37, no. 20, pp. 4790–4797, 2003.

[10] Y. Chen, G. Zhang, H. Liu, and J. Qu, "Confining free radicals in close vicinity to contaminants enables ultrafast Fenton-like processes in the interspacing of MoS2Membranes," *Angewandte Chemie International Edition*, vol. 58, no. 24, pp. 8134–8138, 2019.

[11] J. Du, J. Bao, Y. Liu, S. H. Kim, and D. D. Dionysiou, "Facile preparation of porous Mn/Fe_3O_4 cubes as peroxymonosulfate activating catalyst for effective bisphenol A degradation," *Chemical Engineering Journal*, vol. 376, article 119193, 2019.

[12] X. Duan, Z. Ao, H. Zhang et al., "Nanodiamonds in sp^2/sp^3 configuration for radical to nonradical oxidation: core-shell layer dependence," *Applied Catalysis B: Environmental*, vol. 222, pp. 176–181, 2018.

[13] X. Cheng, H. Guo, Y. Zhang, G. V. Korshin, and B. Yang, "Insights into the mechanism of nonradical reactions of persulfate activated by carbon nanotubes: activation performance and structure-function relationship," *Water Research*, vol. 157, pp. 406–414, 2019.

[14] X. Duan, H. Sun, Y. Wang, J. Kang, and S. Wang, "N-Doping-induced nonradical reaction on single-walled carbon nanotubes for catalytic phenol oxidation," *ACS Catalysis*, vol. 5, no. 2, pp. 553–559, 2015.

[15] X. Lu, J. Zhao, Q. Wang et al., "Sonolytic degradation of bisphenol S: effect of dissolved oxygen and peroxydisulfate,

oxidation products and acute toxicity," *Water Research*, vol. 165, article 114969, 2019.

[16] Y. Qin, G. Li, Y. Gao, L. Zhang, Y. S. Ok, and T. An, "Persistent free radicals in carbon-based materials on transformation of refractory organic contaminants (ROCs) in water: a critical review," *Water Research*, vol. 137, pp. 130–143, 2018.

[17] B. Xu, T. Ding, Y. Zhang, Y. Wen, Z. Yang, and M. Zhang, "A new efficient visible-light-driven composite photocatalyst comprising ZnFe$_2$O$_4$ nanoparticles and conjugated polymer from the dehydrochlorination of polyvinyl chloride," *Materials Letters*, vol. 187, pp. 123–125, 2017.

[18] Y. Zhang, F. Zhang, Z. Yang, H. Xue, and D. D. Dionysiou, "Development of a new efficient visible-light-driven photocatalyst from SnS$_2$ and polyvinyl chloride," *Journal of Catalysis*, vol. 344, pp. 692–700, 2016.

[19] S. Debnath, N. Ballav, H. Nyoni, A. Maity, and K. Pillay, "Optimization and mechanism elucidation of the catalytic photodegradation of the dyes Eosin Yellow (EY) and Naphthol blue black (NBB) by a polyaniline-coated titanium dioxide nanocomposite," *Applied Catalysis B: Environmental*, vol. 163, pp. 330–342, 2015.

[20] L. Liu, L. Ding, Y. Liu et al., "A stable Ag$_3$PO$_4$@PANI core@-shell hybrid: enrichment photocatalytic degradation with π-π conjugation," *Applied Catalysis B: Environmental*, vol. 201, pp. 92–104, 2017.

[21] J. Zhang, H. Yang, S. Xu et al., "Dramatic enhancement of visible light photocatalysis due to strong interaction between TiO$_2$ and end-group functionalized P3HT," *Applied Catalysis B: Environmental*, vol. 174-175, pp. 193–202, 2015.

[22] P. D. Bui, H. H. Tran, F. Kang et al., "Insight into the photocatalytic mechanism of tin dioxide/polyaniline nanocomposites for no degradation under solar light," *ACS Applied Nano Materials*, vol. 1, no. 10, pp. 5786–5794, 2018.

[23] Y. Bai, K. Nakagawa, A. J. Cowan et al., "Photocatalyst Z-scheme system composed of a linear conjugated polymer and BiVO$_4$ for overall water splitting under visible light," *Journal of Materials Chemistry A*, vol. 8, no. 32, pp. 16283–16290, 2020.

[24] V. V. Pham, D. P. Bui, H. H. Tran et al., "Photoreduction route for Cu$_2$O/TiO$_2$ nanotubes junction for enhanced photocatalytic activity," *RSC Advances*, vol. 8, no. 22, pp. 12420–12427, 2018.

[25] T. K. Truong, T. Van Doan, H. H. Tran et al., "Effect of cr doping on visible-light-driven photocatalytic activity of ZnO nanoparticles," *Journal of Electronic Materials*, vol. 48, no. 11, pp. 7378–7388, 2019.

[26] P. Van Viet, T. H. Huy, T. T. Sang, H. M. Nguyet, and C. M. Thi, "One-pot hydrothermal synthesis of Si doped TiO$_2$ nanotubes from commercial material sources for visible light-driven photocatalytic activity," *Materials Research Express*, vol. 6, no. 5, article 055006, 2019.

[27] E. Fenelon, D.-P. Bui, H. H. Tran et al., "Straightforward synthesis of SnO$_2$/Bi$_2$S$_3$/BiOCl–Bi$_{24}$O$_{31}$Cl$_{10}$ Composites for drastically enhancing rhodamine B photocatalytic degradation under visible light," *ACS Omega*, vol. 5, no. 32, pp. 20438–20449, 2020.

[28] D. P. Bui, M. T. Nguyen, H. H. Tran, S. J. You, Y. F. Wang, and P. van Viet, "Green synthesis of Ag@SnO$_2$ nanocomposites for enhancing photocatalysis of nitrogen monoxide removal under solar light irradiation," *Catalysis Communications*, vol. 136, article 105902, 2020.

[29] D.-. P. Bui, H. Pham, T. Cao, and V. Pham, "Preparation of conjugated polyvinyl chloride/TiO2nanotubes for rhodamine B photocatalytic degradation under visible light," *Journal of Chemical Technology & Biotechnology*, vol. 95, pp. 2707–2714, 2020.

[30] F. Chen, G. X. Huang, F. B. Yao et al., "Catalytic degradation of ciprofloxacin by a visible-light-assisted peroxymonosulfate activation system: performance and mechanism," *Water Research*, vol. 173, article 115559, 2020.

[31] Y. Wang, X. Zhao, D. Cao, Y. Wang, and Y. Zhu, "Peroxymonosulfate enhanced visible light photocatalytic degradation bisphenol A by single-atom dispersed Ag mesoporous g-C3N4 hybrid," *Applied Catalysis B: Environmental*, vol. 211, pp. 79–88, 2017.

[32] J. Lim, D. Y. Kwak, F. Sieland, C. Kim, D. W. Bahnemann, and W. Choi, "Visible light-induced catalytic activation of peroxymonosulfate using heterogeneous surface complexes of amino acids on TiO$_2$," *Applied Catalysis B: Environmental*, vol. 225, pp. 406–414, 2018.

[33] Y.-Y. Ahn, H. Bae, H. I. Kim et al., "Surface-loaded metal nanoparticles for peroxymonosulfate activation: efficiency and mechanism reconnaissance," *Applied Catalysis B: Environmental*, vol. 241, pp. 561–569, 2019.

[34] J. Lee, U. von Gunten, and J. H. Kim, "Persulfate-based advanced oxidation: critical assessment of opportunities and roadblocks," *Environmental Science Technology*, vol. 54, no. 6, pp. 3064–3081, 2020.

[35] B. C. Hodges, E. L. Cates, and J. H. Kim, "Challenges and prospects of advanced oxidation water treatment processes using catalytic nanomaterials," *Nature Nanotechnology*, vol. 13, no. 8, pp. 642–650, 2018.

[36] P. Van Viet, T. H. Huy, S.-J. You, L. Van Hieu, and C. M. Thi, "Hydrothermal synthesis, characterization, and photocatalytic activity of silicon doped TiO$_2$ nanotubes," *Superlattices and Microstructures*, vol. 123, pp. 447–455, 2018.

[37] P. Van Viet, T. H. Huy, N. X. Sang, C. M. Thi, and L. Van Hieu, "One-step hydrothermal synthesis and characterisation of SnO$_2$ nanoparticle-loaded TiO$_2$ nanotubes with high photocatalytic performance under sunlight," *Journal of Materials Science*, vol. 53, no. 5, pp. 3364–3374, 2018.

[38] J. Sarma, A. Sarma, and K. G. Bhattacharyya, "Biosorption of commercial dyes on *Azadirachta indica* leaf powder: a case study with a basic dye rhodamine B," *Industrial & Engineering Chemistry Research*, vol. 47, no. 15, pp. 5433–5440, 2008.

[39] S. Narita, S. Ichinohe, and S. Enomoto, "Infrared spectrum of polyvinyl chloride. I," *Journal of Polymer Science*, vol. 37, no. 131, pp. 273–280, 1959.

[40] V. A. Zeitler and C. A. Brown, "The infrared spectra of some Ti-O-Si, Ti-O-Ti and Si-O-Si compounds," *The Journal of Physical Chemistry*, vol. 61, no. 9, pp. 1174–1177, 1957.

[41] T. H. Huy, D. P. Bui, F. Kang et al., "SnO$_2$/TiO$_2$ nanotube heterojunction: the first investigation of NO degradation by visible light-driven photocatalysis," *Chemosphere*, vol. 215, pp. 323–332, 2019.

[42] C. Cai, J. Liu, Z. Zhang, Y. Zheng, and H. Zhang, "Visible light enhanced heterogeneous photo-degradation of orange II by zinc ferrite (ZnFe$_2$O$_4$) catalyst with the assistance of persulfate," *Separation and Purification Technology*, vol. 165, pp. 42–52, 2016.

[43] F. Chi, B. Song, B. Yang, Y. Lv, S. Ran, and Q. Huo, "Activation of peroxymonosulfate by BiFeO3microspheres under visible

light irradiation for decomposition of organic pollutants," *RSC Advances*, vol. 5, no. 83, pp. 67412–67417, 2015.

[44] Y. Leng, W. Guo, X. Shi et al., "Degradation of rhodamine B by persulfate activated with Fe_3O_4: effect of polyhydroquinone serving as an electron shuttle," *Chemical Engineering Journal*, vol. 240, pp. 338–343, 2014.

[45] Y. Liu, H. Guo, Y. Zhang, W. Tang, X. Cheng, and H. Liu, "Activation of peroxymonosulfate by $BiVO_4$ under visible light for degradation of rhodamine B," *Chemical Physics Letters*, vol. 653, pp. 101–107, 2016.

[46] Y. Du, W. Ma, P. Liu, B. Zou, and J. Ma, "Magnetic $CoFe_2O_4$ nanoparticles supported on titanate nanotubes ($CoFe_2O_4$/TNTs) as a novel heterogeneous catalyst for peroxymonosulfate activation and degradation of organic pollutants," *Journal of Hazardous Materials*, vol. 308, pp. 58–66, 2016.

[47] L. Hu, G. Deng, W. Lu, Y. Lu, and Y. Zhang, "Peroxymonosulfate activation by Mn_3O_4 /metal-organic framework for degradation of refractory aqueous organic pollutant rhodamine B," *Chinese Journal of Catalysis*, vol. 38, no. 8, pp. 1360–1372, 2017.

[48] C. Huang, Y. Wang, M. Gong, W. Wang, Y. Mu, and Z.-H. Hu, "α-MnO_2/palygorskite composite as an effective catalyst for heterogeneous activation of peroxymonosulfate (PMS) for the degradation of rhodamine B," *Separation and Purification Technology*, vol. 230, article 115877, 2020.

[49] Y. Wang, F. Li, T. Xue et al., "Heterogeneous activation of peroxymonosulfate by hierarchical $CuBi_2O_4$ to generate reactive oxygen species for refractory organic compounds degradation: morphology and surface chemistry derived reaction and its mechanism," *Environmental Science and Pollution Research*, vol. 25, no. 5, pp. 4419–4434, 2018.

[50] C. Gong, F. Chen, Q. Yang et al., "Heterogeneous activation of peroxymonosulfate by Fe-Co layered doubled hydroxide for efficient catalytic degradation of rhoadmine B," *Chemical Engineering Journal*, vol. 321, pp. 222–232, 2017.

[51] C. Marinescu, M. Ben Ali, A. Hamdi et al., "Cobalt phthalocyanine-supported reduced graphene oxide: a highly efficient catalyst for heterogeneous activation of peroxymonosulfate for rhodamine B and pentachlorophenol degradation," *Chemical Engineering Journal*, vol. 336, pp. 465–475, 2018.

WILEY | Hindawi

Research Article

Effect Of Magnesium Perchlorate Content on the Mechanical, Thermal Stability, and Dielectric Properties of Plasticized PMMA/PVC-g-PMMA Electrolytes

Nguyen Thi Kim Dung,[1] Nguyen Thi Dieu Linh,[2] Do Quang Tham (ORCID),[3,4] Nguyen Thuy Chinh,[3] Man Minh Tan,[5,6] Tran Thi Mai,[3] Nguyen Thi Thu Trang,[3] Do Minh Thanh,[3] Nguyen Quang Tung,[2] and Thai Hoang (ORCID)[3]

[1]National Institute of Education Management, Thanh Xuan, Hanoi 10000, Vietnam
[2]Faculty of Chemical Technology, HaUI, Tay Tuu, North Tu Liem, Hanoi 10000, Vietnam
[3]Institute for Tropical Technology, VAST, 18 Hoang Quoc Viet, Nghia Do, Cau Giay, Hanoi 10072, Vietnam
[4]Graduate University of Science and Technology, VAST, 18 Hoang Quoc Viet, Nghia Do, Cau Giay, Hanoi 10072, Vietnam
[5]Institute of Theoretical and Applied Research, Duy Tan University, Hanoi 100000, Vietnam
[6]Faculty of Natural Sciences, Duy Tan University, Da Nang 550000, Vietnam

Correspondence should be addressed to Do Quang Tham; dqtham@itt.vast.vn

In this study, new types of gel polymer blend electrolytes (GPBEs) were prepared with the synthesized PVC-g-PMMA graft copolymer, PMMA, plasticizers (propylene carbonate (PC), dioctyl phthalate (DOP)), and different loadings of $Mg(ClO_4)_2$ via the solution casting method using tetrahydrofuran as solvent. Fourier transform infrared (FTIR) spectra of the electrolytes showed mutual molecular interactions between $Mg(ClO_4)_2$ and organic moieties. The scanning electron microscopy images of the GPBEs showed their wrinkled surface morphology due to their low elastic modulus and high flexibility. Energy-dispersive X-ray (EDX) spectroscopy and mapping technique revealed the regular distributions of all atomic elements such as Cl, Mg, O, and C in the doped GPBEs. With increasing the Mg salt concentration, Young's modulus and tensile strength of the GPBEs strongly decreased. Interestingly, the elongation at break of the GPBEs was higher than that of neat (undoped) GPBE and achieved the highest value of 215% at the salt content of 20 wt.%. The AC conductivity and ionic conductivity, as well as dielectric permittivity of plasticized PMMA/PVC-g-PMMA/$Mg(ClO_4)_2$ GPBE,s increased with frequency and $Mg(ClO_4)_2$ doping content. Ionic conductivity of the doped GPBEs can be achieved from 5.51×10^{-5} to 4.42×10^{-4} (S.cm^{-1}) using $Mg(ClO_4)_2$ contents in the range from 10 to 40 wt.%. The doped GPBEs are thermally stable up to 100°C with very low weight losses. The GPBE doped with 20 wt.% of $Mg(ClO_4)_2$ can be used as a new type of electrolyte for developing Mg batteries.

1. Introduction

Nowadays, lithium batteries are widely used for energy storage devices in smart phones, tablets/laptops, electric vehicles, etc. [1, 2]. However, fire and explosion accidents of lithium batteries have occasionally occurred worldwide, some of which caused serious threats to user's health [3–5]. The reasons for these accidents are known as the use of liquid electrolytes, the poor thermal stability of lithium salts, and the formation of oxygen in charging/recharging at high temperatures [3]. Therefore, it is necessary to develop new types of ionic batteries with low toxicity, greater safety, and lower cost than lithium batteries [5–11]. Over the past decades, gel polymer electrolytes have been extensively studied due to their high compliance, processability, mouldability, good electrode-electrolyte contact, and high ambient temperature conductivity. Besides, the increasing attention has been paid to the development of magnesium ion

cells/batteries with the high specific capacity, efficiency, and good cyclability [12, 13]. Gel polymer electrolytes can be produced when the polymer swells up in organic solvents or plasticizers, which can provide better contact with the electrode surface than the dry solid polymer electrolytes (free of solvents/plasticizers) [13].

Poly(vinyl chloride) (PVC) and their blends have been employed which used as gel polymer electrolytes [14–20]. Several studies have shown that the tensile properties, [15] thermal stability, [16] ionic conductivity, and [15] charge-discharge properties of PVC can be improved by the blending with poly(methyl methacrylate) (PMMA) or using graft copolymer-like PVC-graft-PMMA and plasticizers to form gel polymer blend (GPB) electrolytes [14, 20].

In our previous study, we have reported the mechanical and dielectrical properties of GPBEs doped with $Mg(ClO_4)_2$ salt [21]. It was found that plasticizers are very important to improve the ionic conductivity of the GPBEs. However, it is necessary to enhance the mechanical and dielectrical properties for the GPBEs to expand the applicability of the materials. In this study, a graft copolymer named PVC-g-PMMA (PVCg) was synthesized and mixed with PMMA and plasticizers to prepare PMMA/PVCg gel polymer blend electrolytes. The graft copolymer was expected as a compatibilizer for improving mechanical and electrical properties of the GPBEs. The effects of magnesium perchlorate on these properties and morphology of the electrolytes were also investigated.

2. Experimental

2.1. Materials.
Polyvinyl chloride (PVC, SG-660, k index of 65-67) is a commercial product of Plastic & Chemical Corp., Ltd. (TPC Vina, Vietnam). Methyl methacrylate (MMA, 99%), poly(methyl methacrylate) (PMMA, weight average molecular weight of 120000), and propylene carbonate (PC, 99.7%) were purchased from Aldrich (USA). Tetrahydrofuran (THF, 99.7%), chloroform (CH_3Cl, 99.5%), and $Mg(ClO_4)_2$ were reagent grade products of Xilong Co., Ltd., China. Ethyl alcohol (ethanol, 99.7%), methyl alcohol (methanol, 99.7%), and dioctyl phthalate (DOP, 95%) were provided by Duc Giang Chemical and Detergent powder Joint Stock Company, Vietnam. Chemicals were of analytical grade and used as received.

2.2. Preparation of Electrolyte Films.
Graft copolymer of PVC-g-PMMA (labeled as PVCg) with the PMMA graft content of 20.3 wt% had been prepared as stated in the previous study [22]. As similarly, the weight ratio of PVC : PMMA was kept as 1 : 1 in this study. Therefore, the compositions of GPBEs were prepared as shown in Table 1, where the weight of PMMA in PVC-g-PMMA was calculated of 0.115 g and that of PVC was 0.45 g, or PMMA : PVC weight ratio of 1 : 1. In an example of preparation of an electrolyte film, PMMA, PVCg, plasticizers, and $Mg(ClO_4)_2$ were charged in a flask containing THF. The mixture was stirred at 40°C for 4 hours to obtain a homogenous solution which was then poured into a $10 \times 10 \times 1$ (cm) release paper. The THF solvent was allowed to evaporate naturally in a fume hood for

TABLE 1: Compositions and sample labels for electrolyte films doped with different $Mg(ClO_4)_2$ contents.

Label of sample	PMMA (g)	PVCg (g)	DOP +PC(g)	$Mg(ClO_4)_2$ (g)
GPBE.0	0.335	0.565	1.800	—
GPBE.10	0.335	0.565	1.800	0.300
GPBE.20	0.335	0.565	1.800	0.675
GPBE.30	0.335	0.565	1.800	1.157
GPBE.40	0.335	0.565	1.800	1.800

24 h, then complete drying in vacuum oven at 40°C for 24 h. The collected film was stored in a desiccator for at least 24 h before characterizations. The compositions and sample labels are described in Table 1.

2.3. Characterization.
FTIR spectra of all samples were performed on a Fourier transform infrared spectrometer (Nicolet/Nexus 670, USA) with 32 scans, $4 cm^{-1}$ resolution, and in wave number ranging from 400 to $4000 cm^{-1}$ at room temperature.

The tensile properties of the electrolyte samples were conducted on a universal testing machine (Zwick V.2.5, Germany) with a crosshead speed of 50 mm/min, in accordance with ASTM D882 for thin plastic films.

Complex dielectric properties (real part—Z' [R] and imaginary part—Z'' [X]) of electrolyte films were measured by using an Agilent E4980A instrument at R-X impedance parameters using the 16451B test fixture, in the frequency range of 25 Hz-1 MHz (according to the limit of the Agilent E4980A instrument), with a peak amplitude of 1.0 V and applied voltage to the ground electrode of 0 V (Earth ground), at room temperature (24-28°C), as per ASTM D150 standard. Electrolyte films were sandwiched between stainless steel (SS) electrodes as the SS/GPBEs/SS configuration or Mg electrodes as the SS/Mg/GPBEs/Mg/SS configuration. Mg electrodes with a diameter of 5 mm were cut from the Mg sheet.

AC conductivity (σ) and dielectric constant (ε) of electrolyte films were determined from measured R-X values (capacitive reactance and resistance of complex impedance) as the equations at every frequency (f): [23–25].

$$\sigma_{AC} = \frac{1}{R} \times \frac{t}{A}, \tag{1}$$

$$\varepsilon = \frac{1}{2\pi f \varepsilon_0 |X|} \times \frac{t}{A}, \tag{2}$$

where t is the thickness of the electrolyte film, A is the (contact) area of the working electrode (with 0.005 m in diameter), f is the frequency, $|X|$ is the absolute value of X (measured capacitive reactance), R is the measured resistance component, and ε_0 is the vacuum permittivity (8.854×10^{-12} F/m).

Morphology, element composition, and elemental mapping of the samples were analyzed by scanning electron microscopy (SEM) combined with energy dispersive X-ray
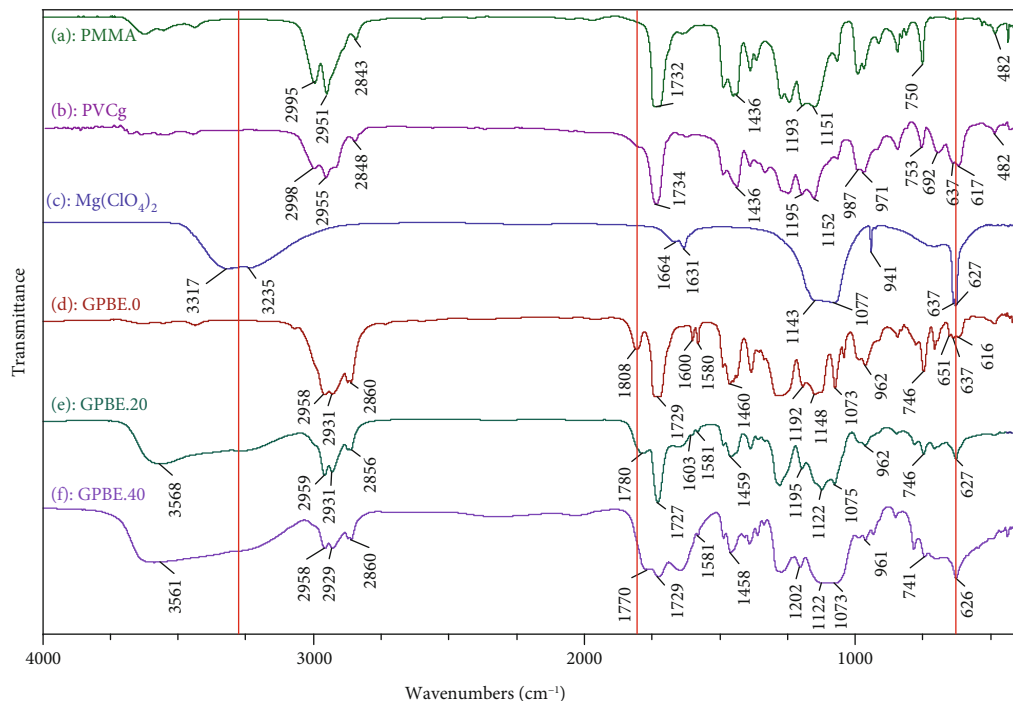
FIGURE 1: The FTIR spectra of (a) PMMA, (b) PVCg copolymer, (c) $Mg(ClO_4)_2$, and spectra of GPBEs with different $Mg(ClO_4)_2$ contents.

TABLE 2: Band assignments for specific groups in FTIR spectra of PMMA, PVCg, GPBE.0, $Mg(ClO_4)_2$, GPBE.20, and GPBE.40 samples.

	Vibration absorption in the wavenumber (cm^{-1}) for specific groups							
Vibration mode	PMMA	PVCg	$Mg(ClO_4)_2$	GBPE.0	GBPE.10	GBPE.20	GBPE.30	GBPE.40
νC=O (PMMA)	1732	1734	—	1729	1729	1729	1729	1727
νC=O (PC)	—	—	—	1808	1780	1780	1774	1770
δC=O (PMMA)	750	753	—	746	745	746	745	741
δC=O (PC)	—	—	—	771	779	778	778	780
Aromatic ring	—	—	—	1600	1601	1603	1601	1601
	—	—	—	1580	1580	1581	1580	1580
δCH_3	1484;	1486;	—	1487	1487	1485	1485	1483
	1436	1436		1460	1460	1459	1459	1457
δCH_2	1387	1388	—	1383	1385	1385	1384	1388
νC-O	1272	1274	—	1275	1277	1276	1276	1276
νCl-O/	—	—	1143	—	—	—	—	—
	—	—	1077	—	—	1075	1075	1075
νC-Cl	—	—	637	616	627	627	627	626
	—	—	627	637	—	—	—	—

(EDX) spectroscopy (JSM-6510LV SEM instrument, Jeol, Japan).

Thermal Gravimetric Analysis (TGA) was carried out in a NETZSCH TG 209F1 (Germany) instrument to study the thermal degradation properties of the electrolyte under nitrogen gas with a flow rate of 40 ml/min, from room temperature to 650°C with a heating rate of 10°C/min, and specimen weight of about 6-7 mg. All above measurements were carried out in laboratory rooms with relative humidity of 40-50%, and the sample was measured right after removed from the vacuum environment.

3. Results and Discussion

3.1. FTIR Spectra. Figure 1 displays the FTIR spectra of the raw materials and synthesized samples. Referred to previous studies [22], it is very easy to assigned all absorption peaks for specific groups of PMMA (Figure 1(a)), PVCg (Figure 1(b)), and GPBE (Figure 1(c)). For more details, Table 2 lists some main band assignments for PMMA, PVC, and GBPE samples without and with magnesium perchlorate salt (20, 40 wt.%). Comparing with the spectra of neat PMMA and PVCg, the spectrum of the GPBE.0 sample (Figure 1(d)) appears some

(a)

(b)

(c)

(d)
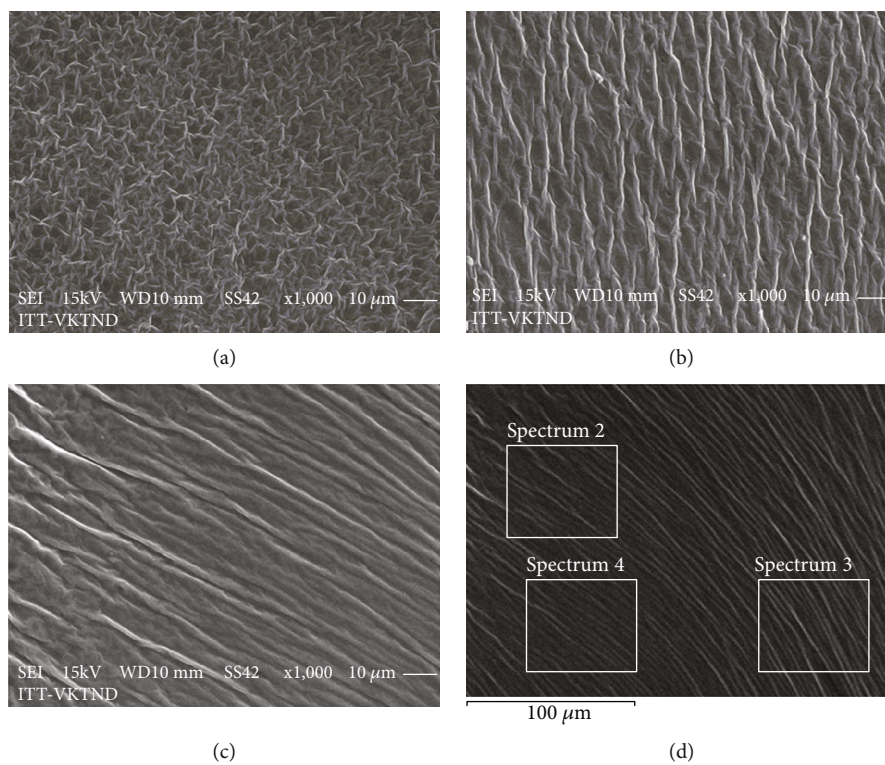
Figure 2: SEM images of (a) GPBE.0, (b) GPBE.10, and (c, d) GPBE.20 films.

Multielement EDS mapping (layered)

Cl K series

(a)

(b)

Mg K series

O K series

(c)

(d)
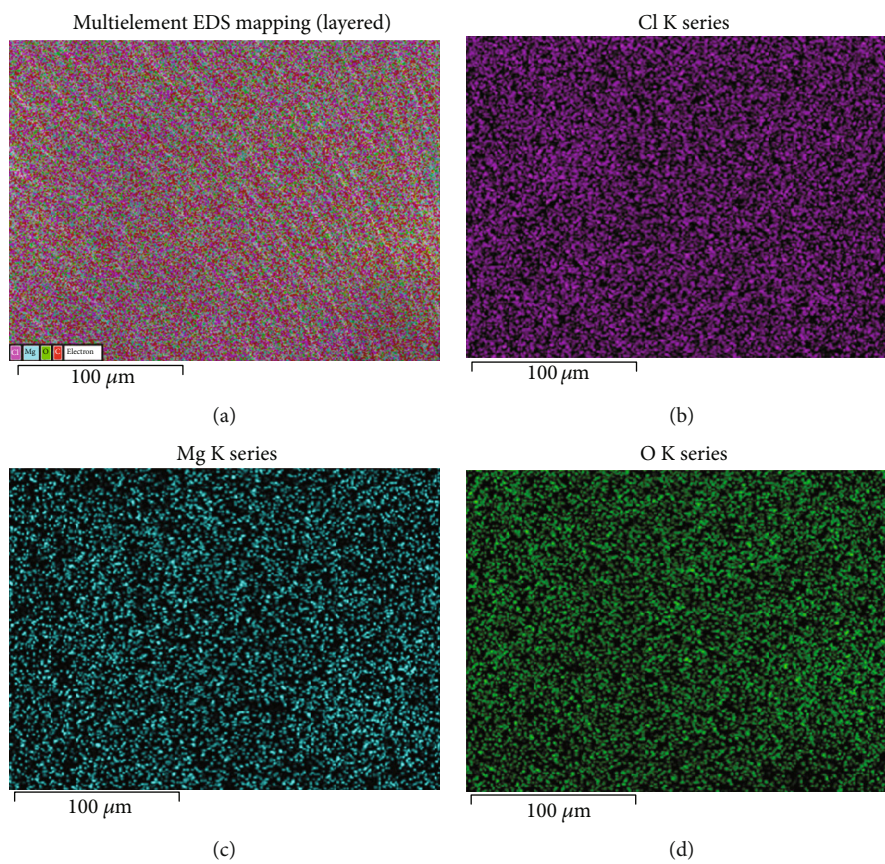
Figure 3: Single elemental mapping of the GPBE.20 film for C, O, Cl, and Mg atoms.

Spectrum 2				
Element	Line type	Weight %	Deviation %	Atomic %
C	K series	62.35	0.28	72.83
O	K series	24.85	0.26	21.79
Mg	K series	1.75	0.03	1.01
Cl	K series	11.04	0.09	4.37
Total		100.00		100.00
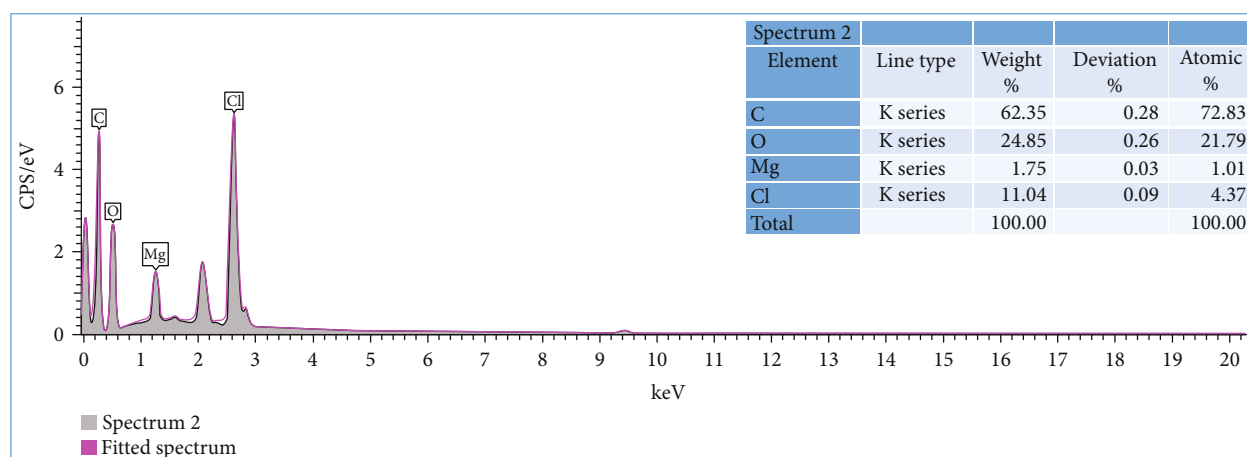
FIGURE 4: EDX spectrum of the GPBE.20 electrolyte film and analyzed composition table.

TABLE 3: Tensile properties of GPBE films with and without $Mg(ClO_4)_2$.

Label of sample	Young's modulus (MPa)	Elongation at break (%)	Tensile strength (MPa)
GPBE.0	2.75	58	1.15
GPBE.10	1.83	142	1.10
GPBE.20	1.38	215	1.02
GPBE.30	1.12	174	0.96
GPBE.40	0.86	167	0.85

(a)

(b)
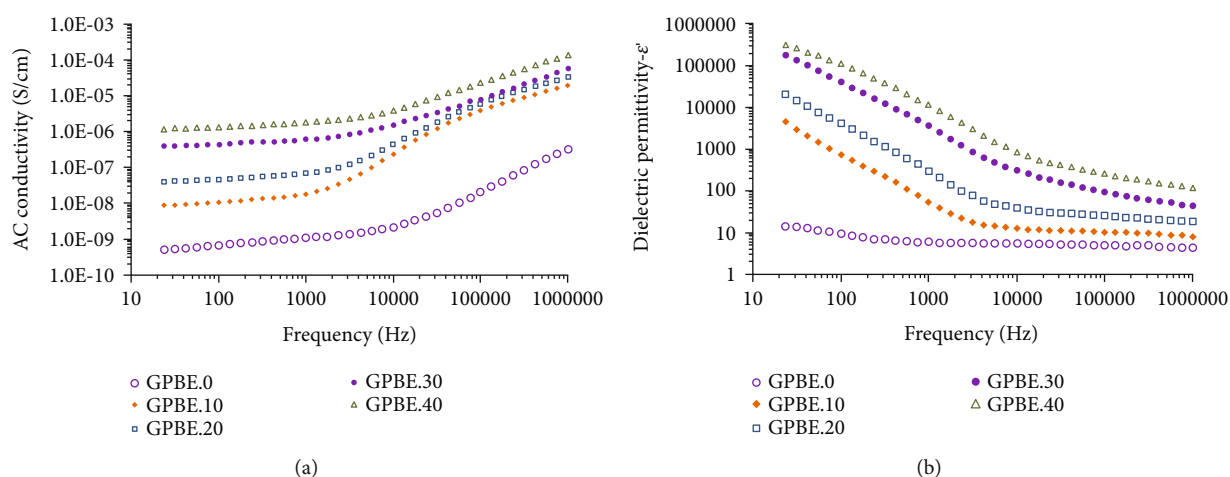
FIGURE 5: Dielectric properties of GPBEs as functions of frequency (a) AC conductivity and (b) dielectric permittivity, with the SS/GPBE/SS electrode configuration at 25°C.

new peaks attributed to the presence of plasticizers, the peaks at 1805 cm^{-1} and 1732 cm^{-1} can be assigned for C=O stretching vibrations (ν) of the PC plasticizer and PMMA, and the doublet at 1600 and 1580 cm^{-1} is assigned for aromatic ring of the DOP plasticizer (Table 2 column 5), whereas comparing with spectrum of the GPBE.0 sample, the FTIR spectra of GPBEs doped with different weight amounts of $Mg(ClO_4)_2$ (Figures 1(e) and 1(f)) show some differences. The first is the strong absorption band of ν(OH) in the wavenumber region from 3700 to 3100 cm^{-1} due to the moisture absorption of $Mg(ClO_4)_2$ from the air during FTIR recording. The second difference is the disappearance of three peaks (651, 637, and 616 cm^{-1}), instead of only one peak at 627 cm^{-1} which appeared in the region of 660-600 cm^{-1}. In addition, the band attributed to C=O of PC appearing at 1808 cm^{-1} in spectrum of GPBE0 is shifted to 1780 and 1770 cm^{-1} in spectrum of GPBE.20 and GPBE.40, respectively. This shift increases with increasing $Mg(ClO_4)_2$ content, indicating the strong interactions between $Mg(ClO_4)_2$ and organic moieties (polymers and plasticizers) in the electrolytes.

(a)

(b)
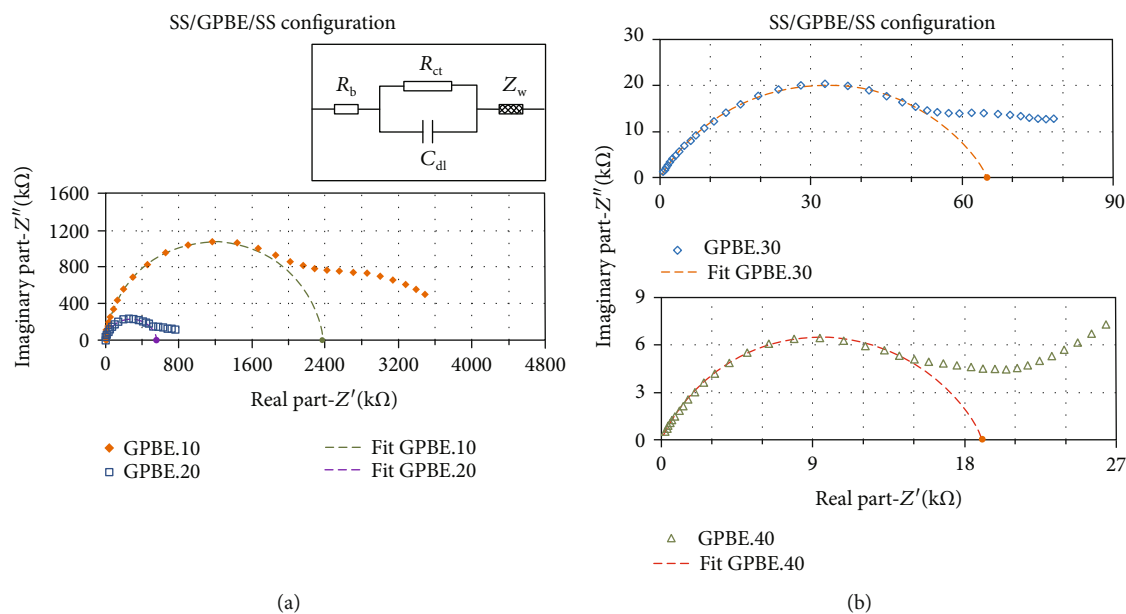
FIGURE 6: Nyquist plot and optimized fitting semicircles of GPBEs doped with different $Mg(ClO_4)_2$ contents.

3.2. Surface Morphology of Electrolyte Films. Figure 2 represents the SEM images of GPBE.0, GPBE.10, and GPBE.20 films. It can be seen that there are wrinkles on the surfaces of two kinds of samples (undoped and doped with magnesium salt), which are caused by the high flexibility of the films containing high plasticizer content. It was reported that PMMA/PVC blend films have craters or islands due to the immiscibility of ethylene/propylene carbonate plasticizer with PVC, which caused the separation of the PVC-rich phase and plasticizer-rich phase [26]. In order to improve the miscibility of plasticizer with the PMMA/PVC blend, ethylene carbonate was replaced by DOP which is known as one of the best plasticizer for PVC; moreover, PVC-g-PMMA graft copolymer was also employed in this study. As a result, the SEM images of new GPBEs clearly reveal that no craters or islands were observed on the surface of GPBEs. In addition, it is also interesting to see that the number of wrinkles on the surface of the $Mg(ClO_4)_2$-doped electrolyte film decreases with increasing Mg salt content.

To clarify the phase compositions at the wrinkles and the surface of the GPBE samples, elemental mapping of the GPBE.20 sample at its surface was conducted. In comparison with the original SEM image (Figure 2(d)) that was selected for EDS analysis, Figure 3(a) shows that the main chemical elements of GPBE.20 including Mg, C, O, and Cl are all appeared and regularly distributed in its layered EDS mapping image, even at the wrinkles. Other EDS mapping images of single elements such as Cl, Mg, and O also confirm their regular distributions in the GPBE.20 sample. In other words, the wrinkles are not the interphase, and there is not any phase separation in the electrolyte sample. It means that using PVC-g-PMMA and DOP can improve the compatibility for the PMMA/PVC blend (50 : 50 wt./wt.).

Figure 4 displays a selected EDX spectrum of the GPBE.20 electrolyte film and the composition table result. The chemical elements of the electrolyte were detected with
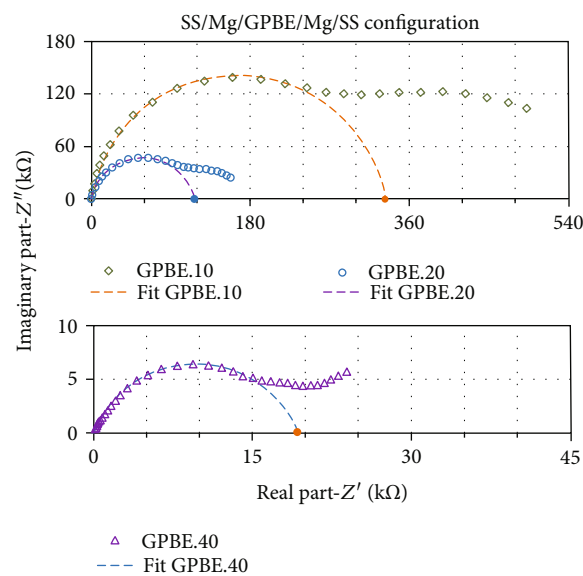
FIGURE 7: Nyquist plot and optimized fitting semicircles of GPBEs doped with different $Mg(ClO_4)_2$ contents.

relevant peaks labeled with C, O, Mg, and Cl. It is noted that the unlabeled peak (between Mg and Cl peaks) is of Pt coat and not taken into account. The table result (inside Figure 4) verifies that magnesium atom appears on the surface of the electrolyte films (1.75wt.%) with lower concentration than those in the bulk (mathematically evaluated as 2.31 wt.%).

3.3. Tensile Properties. Table 3 shows that Young's modulus of GPBE films strongly decreases from 2.75 to 0.65 MPa with increasing $Mg(ClO_4)_2$ contents from 0 to 40 wt.%, and their tensile strength also decreases from 1.72 to 0.84 MPa. In fact, these free-standing films can be commonly mounted in the

TABLE 4: The evaluated values R_b, R_{ct}, and ionic conductivities of the GPBEs.

Sample label	SS/GBPE/SS electrode configuration			SS/Mg/GBPE/Mg/SS electrode configuration		
	R_b (Ω)	R_{ct} (Ω)	σ_{ion} (S/cm)	R_b (Ω)	R_{ct} (Ω)	σ_{ion} (S/cm)
GPBE.10	544.4	2.37×10^6	5.51×10^{-5}	268.8	2.90×10^5	1.14×10^{-4}
GPBE.20	345.0	5.57×10^5	8.86×10^{-5}	120.0	1.17×10^5	2.55×10^{-4}
GPBE.30	139.8	6.51×10^4	2.19×10^{-4}	—	—	—
GPBE.40	97.1	1.90×10^4	3.15×10^{-4}	69.2	1.88×10^4	4.42×10^{-4}
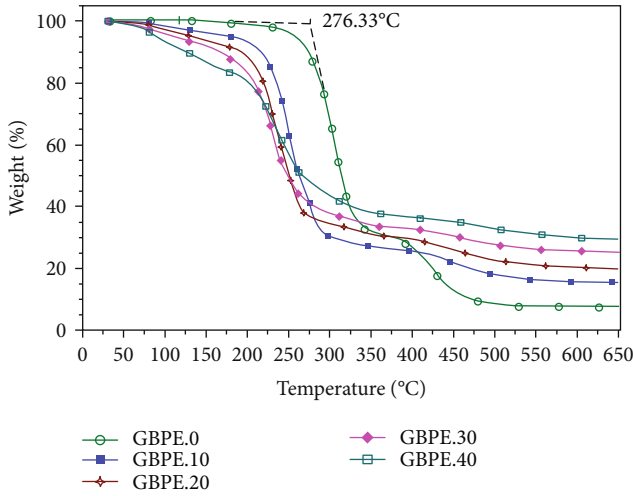
FIGURE 8: TGA diagrams of GPBE.0 and GPBE samples.

tensile test machine. The elongation at break of Mg(ClO$_4$)$_2$-doped GPBEs is higher than that of the undoped GPBEs and reaches the highest value of 215% with 20 wt.%-doped content. In comparison with the previous study, tensile strength and modulus of present GPBEs (using PVC-g-PMMA) are several folders higher than plasticized PMMA/PVC/Mg(ClO$_4$)$_2$ electrolytes with equal salt contents. It demonstrates that the PVC-g-PMMA graft copolymer has played an important role as a compatibilizer to increase the adhesion between polymers and plasticizers.

3.4. Dielectric Properties. Figure 5 displays logarithm plots of AC conductivity and dielectric permittivity as a function of frequency (from 25 Hz to 1 MHz) for the GPBEs with different doping contents of Mg(ClO$_4$)$_2$. Figure 5(a) indicates that AC conductivity of all doped GPBEs increases with frequency and with magnesium salt concentration. The AC conductivities of doped GPBEs are several orders higher than undoped GPBE (GPBE.0). For example, the AC conductivity at 1 kHz of neat GPBE.0 is about 1.07×10^{-9} S/cm. However, the values of GPBE.10, GPBE.20, GPBE.30, and GPBE.40 samples are of 1.83×10^{-8}, 6.86×10^{-7}, 6.03×10^{-7}, and 1.83×10^{-6} S/cm, respectively. Figure 5(b) shows the strongly increase of dielectric permittivity of Mg(ClO$_4$)$_2$-doped electrolytes with the salt concentration. It should be noted that the weights of polymers and plasticizers (Table 3) are kept the same for all GPBEs. The enhancements in AC conductivity and dielectric permittivity are only related to the increase

of the ion carrier concentration, which are generated by the electrolysis of the magnesium salt in the GPBEs.

Figures 6 and 7 display the Nyquist complex impedance plots of GPBEs with different doping contents of Mg(ClO$_4$)$_2$ using SS/GPBE/SS and SS/Mg/GPBE/Mg/SS electrode configurations, in the range from 25 Hz to 1 MHz at room temperature. The impedance plots exhibit two regions, a part of semicircle and a tail, which could be modelled to the equivalent circuit drawn inside Figure 6(a), (where R_b is a bulk resistance, C_{dl} is a double-layer capacitor, R_{ct} is a charge transfer resistance, and Z_w is an interfacial impedance of GPBEs) [23]. Although the first region is not a full semicircle, when completed by fitting, the resistances (R_{ct}, R_b) can be evaluated via the intercepts of the semicircle with the real part axis at low- and high-frequency regions, respectively. It is easy to recognize that the diameters of the fitted semicircles (~$2R_{ct}$ resistances) are reduced by increasing Mg(ClO$_4$)$_2$ doping contents.

For more details, Table 4 shows the evaluated values of R_{ct} and R_b of GPBE films from Figures 6 and 7. For the SS/GPBE/SS configuration, obtained results indicate that R_{ct} and R_b of electrolyte samples decrease with increasing salt content from 10 to 40 wt.%. Based on equation (1), the ionic conductivity of GPBEs doped with Mg(ClO$_4$)$_2$ (GPBE.10, 20, 30, 40) increases from 5.51×10^{-5} to 3.15×10^{-4} (S.cm^{-1}). With the SS/Mg/GPBE/Mg/SS configuration, obtained results also show a similar decrease of R_{ct} and R_b of electrolyte samples with increasing the salt content. However, the lower value of R_{ct} for the SS/Mg/GPBE configuration at the same content of Mg(ClO$_4$)$_2$ confirmed that equilibrium was established between Mg metal and Mg^{2+} ions in the GPPE [27]. Table 4 also shows that the intercept (R_b) values using the SS/Mg/GPBE configuration are higher than using for the GPBE samples with the SS/GPBE configuration.

3.5. Thermal Stability. Figure 8 illustrates the TGA diagrams of the undoped (or neat) GBPE and the GPBEs that were doped with magnesium perchlorate salt at different loadings. Table 5 displays the thermo analysis results from the above TGA diagrams. Figure 8 and Table 5 clearly present some differences between the undoped GPBE sample (GPBE.0) and doped GBPE samples (GPBE.10, 20, 30, 40); in other words, magnesium perchlorate affects the thermal stability of the neat GPBE. In the temperature region below 200°C, the TGA line of the GPBE.0 sample keeps almost constant, which indicates it is thermo-stable in this temperature range. Meanwhile, the TGA curves of doped GPBEs show the first weight loss in this temperature region, due to the removal of

TABLE 5: Thermal parameters of GPBE films with and without $Mg(ClO_4)_2$.

Analysis result\sample	GPBE.0	GPBE.10	GPBE.20	GPBE.30	GPBE.40
Onset temperature (°C)	276.3	229.0	212.2	208.2	207.7
Weight at 75°C (%)	100	99.49	98.88	97.86	97.33
Weight at 100°C (%)	100	98.35	97.28	95.97	93.33
Weight at 200°C (%)	98.93	93.10	88.43	83.66	80.48
Weight at 400°C (%)	26.86	25.56	29.33	32.8	36.7
Weight at 650°C (%)	7.641	15.49	19.95	25.31	29.3

adsorbed water [28]. Table 5 shows that the weight loss at 150°C of the doped GPBEs increases with increasing magnesium salt contents. This may result from the present of $Mg(ClO_4)_2$ as a weak Lewis acid property which can accelerate the degradation of PVC. However, with temperature lower than 100°C, the GPBE.10 and GBPE.20 samples are thermally stable with low weight losses, e.g., 1.65 wt.% and 2.72 wt.%, respectively.

In the temperature region from 200 to 650°C, both two types of undoped and doped electrolyte samples undergo thermal degradation of organic moieties and decomposition of magnesium salt. In this temperature range, the GPBE.0 sample undergoes degradation with two distinct stages, the first stage starts from 220°C to 330°C with the onset temperature of 277.4°C, and this can be attributed to the dehydrochlorination of PVC and unsaturated groups of PMMA [16, 29, 30]. The second stage starts from 330 to 650°C with char residual of about 8 wt.%. In 200-280°C range, the TGA curves of doped electrolyte samples also show their second stages of thermal degradation, in which their curves shift to lower temperature compared to that of the GPBE.0 sample. This means that magnesium perchlorate salt strongly reduces the thermal stability of the plasticized PVCg/PMMA blend. Table 5 shows that the onset temperatures of doped electrolyte samples strongly reduce when increasing the salt contents. This phenomenon can be due to the decomposition of perchlorate groups that has generated the oxide atoms which accelerate the oxidation and dehydrochlorination of PVC as well as the degradation of other organic substances in the GPBEs.

It should be noted that stabilizers had not been mixed with PVC while preparing plasticized PVC-g-PMMA/PMMA blend electrolytes in order to investigate the sole effect of magnesium perchlorate on its thermal stability and other electrical properties. This suggests that stabilizers for PVC should be used in order to limit the thermal stability of the $Mg(ClO_4)_2$-doped GPBEs.

4. Conclusion

$Mg(ClO_4)_2$-doped GPBEs have been prepared by using the solution casting method. The obtained results showed that PVC-g-PMMA played an important role as the compatibilizer for enhancing mechanical and dielectrical properties of GPBEs. Some observable changes in FTIR spectra of GPBEs indicate the molecular interactions between the salt and plasticizers/polymers in the GPBEs. SEM images and EDX map-

ping technique demonstrated that $Mg(ClO_4)_2$ regularly distributed into the plasticizers/polymers system. Young's modulus and tensile strength of GPBEs strongly reduced with the loading $Mg(ClO_4)_2$ content. The elongation at break of the doped GPBEs was higher than the undoped GPBE and reached the highest value of 215% at the doping content of 20 wt.%. The AC and ionic conductivities of GPBEs increased with the loading $Mg(ClO_4)_2$ content. Magnesium perchlorate reduced the thermal stability of GPBE films; however, the doped GPBEs are thermally stable with low weight losses at temperature lower than 100°C. Stabilizers and anhydrous magnesium perchlorate and water-free media should be used when preparing GBPE films for the next studies. In overall consideration of mechanical, dielectrical properties and thermal stability of the GPBEs, the plasticized PMMA/PVC-g-PMMA with 20 wt.% $Mg(ClO_4)_2$ can be chosen as a best candidate of electrolyte for magnesium batteries with working temperature lower than 100°C.

Data Availability

The data used to support the findings of this study are included within the article.

Conflicts of Interest

All authors declare that they have no conflicts of interest.

Acknowledgments

References

[1] J. Bao, C. Tao, R. Yu, M. Gao, Y. Huang, and C. Chen, "Solid polymer electrolyte based on waterborne polyurethane for all-solid-state lithium ion batteries," *Journal of Applied Polymer Science*, vol. 134, no. 48, 2017.

[2] A. Manthiram, X. Yu, and S. Wang, "Lithium battery chemistries enabled by solid-state electrolytes," *Nature Reviews Materials*, vol. 2, no. 4, 2017.

[3] Q. Wang, J. Sun, and G. Chu, *Lithium ion Battery Fire and Explosion, in Fire Safety Science – Proceedings of the Eighth International Symposium*, Tsinghua University, Beijing, China, 2005.

[4] M. S. Apitanawit, *Influence of the Samsung Galaxy Note 7's Battery Problem on Consumer Perception and Intention to Purchase Samsung Smartphone in the Future*, Master Science Program in Marketing, Thammasat University, 2016.

[5] K. Liu, Y. Liu, D. Lin, A. Pei, and Y. Cui, "Materials for lithium-ion battery safety," *Science advances*, vol. 4, no. 6, p. eaas9820, 2018.

[6] D. Liu, W. Zhu, Z. Feng, A. Guerfi, A. Vijh, and K. Zaghib, "Recent progress in sulfide-based solid electrolytes for Li-ion batteries," *Materials Science and Engineering B*, vol. 213, pp. 169–176, 2016.

[7] L. Yue, J. Ma, J. Zhang et al., "All solid-state polymer electrolytes for high-performance lithium ion batteries," *Energy Storage Materials*, vol. 5, pp. 139–164, 2016.

[8] U. Ali, K. J. B. A. Karim, and N. A. Buang, "A review of the properties and applications of poly (methyl methacrylate) (PMMA)," *Polymer Reviews*, vol. 55, no. 4, pp. 678–705, 2015.

[9] S. W. Moore and P. J. Schneider, *A Review of Cell Equalization Methods for Lithium Ion and Lithium Polymer Battery Systems*, Society of Automotive Engineers, Inc., 2001.

[10] P. Saha, M. K. Datta, O. I. Velikokhatnyi, A. Manivannan, D. Alman, and P. N. Kumta, "Rechargeable magnesium battery: current status and key challenges for the future," *Progress in Materials Science*, vol. 66, pp. 1–86, 2014.

[11] P. Yao, H. Yu, Z. Ding et al., "Review on polymer-based composite electrolytes for Lithium batteries," *Frontiers in Chemistry*, vol. 7, pp. 522–522, 2019.

[12] J. Wang, S. Song, S. Gao, R. Muchakayala, R. Liu, and Q. Ma, "Mg-ion conducting gel polymer electrolyte membranes containing biodegradable chitosan: preparation, structural, electrical and electrochemical properties," *Polymer Testing*, vol. 62, pp. 278–286, 2017.

[13] R. Manjuladevi, M. Thamilselvan, S. Selvasekarapandian, R. Mangalam, M. Premalatha, and S. Monisha, "Mg-ion conducting blend polymer electrolyte based on poly(vinyl alcohol)-poly (acrylonitrile) with magnesium perchlorate," *Solid State Ionics*, vol. 308, pp. 90–100, 2017.

[14] N.-S. Choi and J.-K. Park, "New polymer electrolytes based on PVC/PMMA blend for plastic lithium-ion batteries," *Electrochimica Acta*, vol. 46, no. 10-11, pp. 1453–1459, 2001.

[15] H.-S. Han, H.-R. Kang, S.-W. Kim, and H.-T. Kim, "Phase-separated polymer electrolyte based on poly(vinyl chloride)/poly(ethyl methacrylate) blend," *Journal of Power Sources*, vol. 112, no. 2, pp. 461–468, 2002.

[16] S. Ramesh, C.-W. Liew, E. Morris, and R. Durairaj, "Effect of PVC on ionic conductivity, crystallographic structural, morphological and thermal characterizations in PMMA–PVC blend-based polymer electrolytes," *Thermochimica Acta*, vol. 511, no. 1-2, pp. 140–146, 2010.

[17] M. P. Scott, M. Rahman, and C. S. Brazel, "Application of ionic liquids as low-volatility plasticizers for PMMA," *European Polymer Journal*, vol. 39, no. 10, pp. 1947–1953, 2003.

[18] S. Rajendran and T. Uma, "Effect of ZrO_2 on conductivity of $PVC–LiBF_4$–DBP polymer electrolytes," *Materials Letters*, vol. 44, no. 3-4, pp. 208–214, 2000.

[19] S. Ramesh, G. B. Teh, R.-F. Louh, Y. K. Hou, P. Y. Sin, and L. J. Yi, "Preparation and characterization of plasticized high molecular weight PVC-based polymer electrolytes," *Sadhana*, vol. 35, no. 1, pp. 87–95, 2010.

[20] W. Li, M. Yuan, and M. Yang, "Dual-phase polymer electrolyte with enhanced phase compatibility based on Poly(MMA-g-PVC)/PMMA," *European Polymer Journal*, vol. 42, no. 6, pp. 1396–1402, 2006.

[21] D. Q. Tham, T. T. Mai, T. Hoang et al., "Preparation and characterizations of plasticized $PMMA/PVC/Mg(ClO_4)_2$ electrolytes," *Vietnam Journal of Science and Technology*, vol. 57, no. 5, pp. 559–571, 2019.

[22] D. Q. Tham, T. T. Mai, T. Hoang, N. T. T. Trang, N. T. Chinh, and D. X. Thang, "Preparation and FTIR studies of PMMA/PVC polymer blends, PVC-g-PMMA graft copolymers and evaluating graft content," *Vietnam Journal of Science and Technology*, vol. 57, no. 1, pp. 32–41, 2019.

[23] G. Girish Kumar and N. Munichandraiah, "Poly(methylmethacrylate)—magnesium triflate gel polymer electrolyte for solid state magnesium battery application," *Electrochimica Acta*, vol. 47, no. 7, pp. 1013–1022, 2002.

[24] K. M. Anilkumar, B. Jinisha, M. Manoj, and S. Jayalekshmi, "Poly(ethylene oxide) (PEO) – poly(vinyl pyrrolidone) (PVP) blend polymer based solid electrolyte membranes for developing solid state magnesium ion cells," *European Polymer Journal*, vol. 89, pp. 249–262, 2017.

[25] S. Ramesh, "Miscibility studies of PVC blends (PVC/PMMA and PVC/PEO) based polymer electrolytes," *Solid State Ionics*, vol. 148, no. 3-4, pp. 483–486, 2002.

[26] A. M. Stephan, T. P. Kumar, N. G. Renganathan, S. Pitchumani, R. Thirunakaran, and N. Muniyandi, "Ionic conductivity and FT-IR studies on plasticized PVC/PMMA blend polymer electrolytes," *Journal of Power Sources*, vol. 89, no. 1, pp. 80–87, 2000.

[27] G. G. Kumar and N. Munichandraiah, "Reversibility of Mg/Mg2+ couple in a gel polymer electrolyte," *Electrochimica Acta*, vol. 44, no. 15, pp. 2663–2666, 1999.

[28] D. J. Devlin and P. J. Herley, "Thermal decomposition and dehydration of magnesium perchlorate hexahydrate," *Thermochimica Acta*, vol. 104, pp. 159–178, 1986.

[29] D. Q. Tham, T. Hoang, N. V. Giang, N. T. K. Dung, and I. Chung, "Synthesis and characterization of (4-arm-star-PMMA)/PMMA-g-SiO_2 hybrid nanocomposites," *Green Processing and Synthesis*, vol. 7, no. 5, pp. 391–398, 2018.

[30] J. Chen, X. A. Nie, J. C. Jiang, and Y. H. Zhou, "Thermal degradation and plasticizing mechanism of poly (vinyl chloride) plasticized with a novel cardanol derived plasticizer," *IOP Conference Series: Materials Science and Engineering*, vol. 292, p. 012008, 2018.

WILEY | Hindawi

Research Article

Metal-Organic Framework MIL-53(Fe): Synthesis, Electrochemical Characterization, and Application in Development of a Novel and Sensitive Electrochemical Sensor for Detection of Cadmium Ions in Aqueous Solutions

Hoang Vinh Tran [ID], Hue Thi Minh Dang [ID], Luyen Thi Tran [ID], Chau Van Tran, and Chinh Dang Huynh

School of Chemical Engineering, Hanoi University of Science and Technology, 1 Dai Co Viet Road, Hanoi 100000, Vietnam

Correspondence should be addressed to Hue Thi Minh Dang; hue.dangthiminh@hust.edu.vn
and Luyen Thi Tran; luyen.tranthi@hust.edu.vn

A metal-organic framework MIL-53(Fe) was successfully synthesized by a simple hydrothermal method. A synthesized MIL-53(Fe) sample was characterized, and results indicated that the formed MIL-53(Fe) was a single phase with small particle size of 0.8 μm and homogeneous particle size distribution was obtained. The synthesized MIL-53(Fe) has been used to modify a glassy carbon electrode (GCE) by a drop-casting technique. Cyclic voltammetry (CV) and electrochemical impedance spectroscopy (EIS) measurements of the MIL-53(Fe)-modified GCE showed that the MIL-53(Fe) was successfully immobilized onto the GCE electrode surface and the electrochemical behavior of the GCE/MIL-53(Fe) electrode was stable. In addition, several electrochemical parameters of MIL-53(Fe)-modified GCE (GCE/MIL-53(Fe)) including the heterogeneous standard rate constant (k^0) and the electrochemically effective surface area (A) were calculated. Obtained results demonstrated that the synthesized MIL-53(Fe) with the small particle size, highly homogeneous particle size, and high electrochemically effective surface area was able to significantly enhance the electrochemical response signal of the working electrode. Therefore, the GCE/MIL-53(Fe) electrode has been used as a highly sensitive electrochemical sensor for cadmium ion (Cd(II)) monitoring in aqueous solution using differential pulse voltammetry (DPV) technique. The response signal of the electrochemical sensor increased linearly in the Cd(II) ion concentration range from 150 nM to 450 nM with the limit of detection (LOD) of 16 nM.

1. Introduction

The pollution of water sources caused by heavy metal ions, inorganic substances, organic matters, and bacteria from different agricultural, industrial, and medical waste sources has seriously affected people's lives and the ecosystems and organisms in the aquatic environment [1–3]. Determining the concentration of pollutants is an important step in environmental monitoring and supervision and is a basis for offering solutions to protect the environment. Chromatography and its associated techniques such as atomic emission spectroscopy (AES), atomic fluorescence spectroscopy (AFS), atomic absorption spectroscopy, and inductively coupled plasma mass spectrometry are common and effective methods for identifying environmental contaminants [3, 4]. However, the above techniques showed many disadvantages such as long testing times, expensive equipment, and complex measurement processes [3, 5]. Therefore, development of new techniques, which possess the advantages of high sensitivity, quick detection, and ease of use, is needed for the on-site, real-time, and continuous monitoring of environmental pollutants [6–11].

In which, electrochemical sensors can offer advantages of low detection limits, wide linear response ranges, and good

stability and reproducibility. Moreover, electrochemical sensors can be easily prepared from many advanced materials to improve sensitivity and selectivity. In general, an electrochemical sensor is configured from two main parts, which are named a sensing element and a transducer. When the sensing element interacts with an analyte, the transducer can convert the sensed information into an electrical signal [10, 12–14]. The important characteristics of the sensor include sensitivity, stability, selectivity, response time, cost, and reusability [9]. To improve the sensitivity of electrochemical sensors, advanced materials have been applied to modified electrodes, including nanostructured conducting polymers [12, 15], metal and metal oxide nanoparticles [16–18], nanostructured carbon materials (such as porous carbon, carbon nanotube, and graphene/graphene oxide) [17–19], and metal-organic frameworks (MOFs) [6, 9, 20–24]. Among them, MOF materials which are constructed by metal ions or clusters and organic ligands via coordination bonds have unique properties including their structural diversity, flexible framework functionality, large metal cluster density, high stability, abundant adsorption sites, and a large surface area exceeding that of activated carbons and zeolites which are traditional porous materials [9, 21, 23–26]. Moreover, the physical and chemical characteristics of MOFs can be customized and precisely designed, depending on how they are synthesized [27]. The development of MOF material-based electrochemical sensors for determining pollutants in water has practical significance and high potential in the field of the environment [9, 28]. Therefore, a number of MOFs have been used in electrochemical sensors to detect organic substances, inorganic ions, antibiotics, and heavy metals in aqueous solutions [9, 20–24, 26, 29, 30].

MIL-53(Fe) (MIL: Materials of Institute Lavoisier), a class of MOFs generated by a combination between iron(III) cations and 1,4-dicarboxylic acid, consists of three-dimensional networks or secondary building units which contain FeO_6 hexagonal chains and dicarboxylate anions [31]. The emergent features of MIL-53(Fe) compared with other MOFs are chemically stable and have lower toxic metal centers and green, sustainable pathways for fabrication [31]. However, only few works have been dedicated to the development of an electrochemical sensor based on MIL-53 for detection of heavy metal ions in aqueous solutions (MIL-53(Al) [10]). Therefore, in this work, an effective hydrothermal method was carried out to synthesize a metal-organic framework MIL-53(Fe), which was then used to modify the glassy carbon electrode (GCE) for sensitive electrochemical determination of Cd(II) ion concentration in aqueous solutions. In addition, the specific characteristics of the synthesized MIL-53(Fe) were also carefully analyzed by various chemical-physical techniques.

2. Experimental

2.1. Chemicals and Instrumentations

2.1.1. Chemicals. Iron(III) chloride hexahydrate $FeCl_3 \cdot 6H_2O$ (99%wt.), terephthalic acid C_6H_4-1,4-$(COOH)_2$ (TPA) (98%wt.), methanol CH_3OH (MeOH) (anhydrous, 99.8% $v/$ v), sodium acetate CH_3COONa (99%wt.), and cadmium nitrate tetrahydrate $Cd(NO_3)_2 \cdot 4H_2O$ (99%wt.) were purchased from Sigma-Aldrich. Dimethylformamide C_3H_7NO (DMF) (99.94%) was purchased from Fisher Chemical. Polyethylene glycol 2000 ($H(OCH_2CH_2)_nOH$, PEG 2000) was purchased from Alfa Aesar. Chitosan (CS, MW = 400,000 $g\,mol^{-1}$, degree of acetylation (DA) = 70%) was prepared by deacetylation of chitin in our laboratory [32, 33]. Acetate buffer solution 0.1 M (ABS) with pH 5.0 was prepared by using the appropriate amounts of sodium acetate and acetic acid.

2.1.2. Instrumentations. A PGSTAT302N AutoLab electrochemical workstation (Netherlands) was used to perform electrochemical measurements. X-ray diffraction (XRD) measurements were carried out using a Bruker D8 Advance diffractometer equipped with Cu-Kα radiation ($\lambda = 1.54056$ Å). Scanning electron microscope (SEM) images of MIL-53(Fe) were investigated using a Hitachi S4800 scanning electron microscope. The structure of MIL-53(Fe) was examined using Fourier transform infrared spectroscopy (FT-IR) spectra measured with a Nicolet 6700 FT-IR spectrometer. Transmission electron microscope (TEM) images were taken using a TECNAI F20-G2 high-resolution transmission electron microscope.

2.2. Synthesis of MIL-53(Fe).
0.623 g of $FeCl_3 \cdot 6H_2O$ and 0.383 g of TPA were mixed in 50 mL of DMF solvent using an IKA magnetic stirrer with a stirring rate of 200 rpm for 10 minutes to get a solution. Then, the solution was added in an autoclave, and the hydrothermal synthesis was performed at 150°C for 12 hours. The product obtained after the hydrothermal process was filtrated, washed with 150 mL of MeOH and distilled water, and then dispersed in distilled water and stirred on the IKA magnetic stirrer with a stirring rate of 200 rpm for 15 hours. After that, the product was vacuum-dried at 170°C for 12 hours. Finally, the synthesized product was finely ground and stored in a desiccator.

2.3. Electrochemical Characterizations of MIL-53(Fe) and Detection of Cd(II) Ions Using MOF-Based Electrochemical Sensors

2.3.1. Fabrication of MIL-53(Fe)-Modified Electrodes. GCE was polished using 0.3 and 0.05 μm alumina slurries on a polishing cloth; then, it was cleaned carefully by deionized water and dried under an infrared lamp. A slurry of MIL-53(Fe) was prepared by dispersing 6.0 mg of MIL-53(Fe) into a 2 mL mixture of CS solution (10 mg mL^{-1} in acetic acid 3% v/v) and 1.0 mg of PEG-2000 using ultrasonic processing for 5 minutes. Finally, 6 μL of the MOFs/CS/PEG mixture was drop-casted onto the surface of GCE, and it was dried in the air under an infrared lamp. The MIL-53(Fe)-modified GCE (GCE/MIL-53(Fe)) was obtained.

2.3.2. Electrochemical Measurements. A three-electrode configuration consisted of the GCE/MIL-53(Fe) as a working electrode (WE), a Pt electrode as a counter electrode (CE), and a Ag/AgCl electrode as a reference electrode (RE). CV and EIS measurements of the GCE/bare and GCE/MIL-
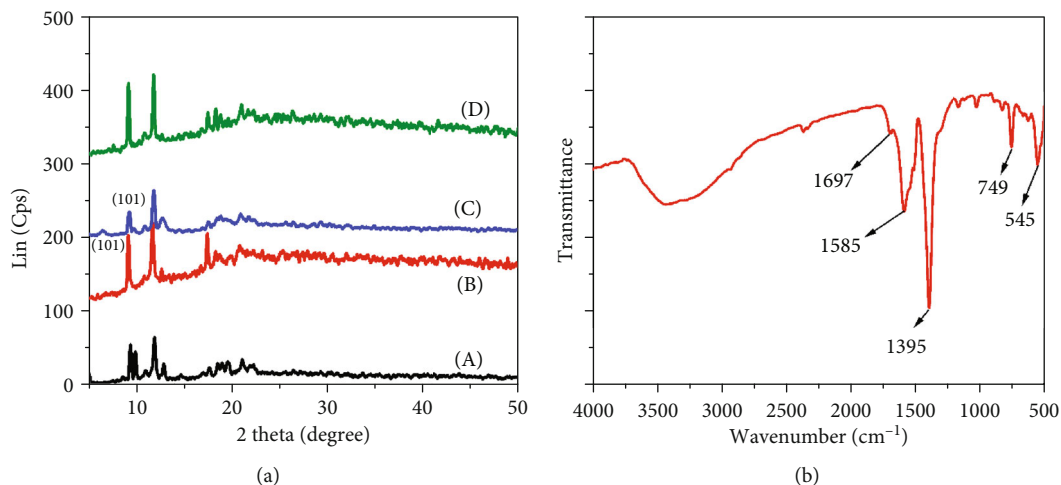
FIGURE 1: (a) XRD patterns of the fabricated MIL-53(Fe) samples when the hydrothermal time was (A) 8 h, (B) 12 h, (C) 15 h, and (D) 24 hours; (b) FT-IR spectrum of the fabricated MIL-53(Fe).

53(Fe) electrodes were performed in $K_3Fe(CN)_6/K_4Fe(CN)_6$ (0.005 M) and 0.1 M KCl solution. CVs were recorded at different scan rates of 25, 30, 35, 40, 45, 50, 55, 60, 65, 70, and 75 mV s^{-1}. EIS spectra were measured with frequency range: 100 kHz to 100 mHz, E_{AC} = 5 mV, E_{DC} = 180 mV. Cadmium ions in aqueous solutions were detected using the MOF-based electrochemical sensors with DPV measurements. The electrolyte solutions contained cadmium ions (in ABS) with the concentrations of 150, 200, 250, 300, 350, 400, and 450 nM. A deposition potential of −1.2 V was applied for 120 s under stirring. After preconcentration, DPV measurements were recorded from −1.1 to −0.3 V with a pulse amplitude of 50 mV and width of 50 ms. Before the next detection, the desorption process was performed under the potential of 0.4 V for 100 s to remove the residual metal ions.

3. Results and Discussion

3.1. Characterizations of MIL-53(Fe). The XRD patterns of as-prepared MIL-53(Fe) samples with various hydrothermal times including 8, 12, 15, and 24 hours are presented in Figure 1(a). It can be seen that the samples prepared with the hydrothermal time of 8 hours (Figure 1(a), curve A) and 24 hours (Figure 1(a), curve D) have specific peaks of the MIL-53(Fe); however, there are several peaks belonging to other crystals [31, 34]. Meanwhile, the XRD patterns of samples prepared with the hydrothermal time of 12 or 15 hours (Figure 1(a), curves B and C, respectively) show only characteristic peaks of MIL-53(Fe) at 9.5, 12.5, and 18.2 degrees of 2-theta [31, 34]. These peaks shift slightly compared to the previous reports due to the different reaction conditions [35, 36]. Comparing XRD patterns of sample B and sample C (samples were synthesized with the hydrothermal time of 12 and 15 hours, respectively), the hydrothermal time for the formation of MIL-53(Fe) was finally chosen to be 12 hours because of the sharper and higher characteristic peaks, which implied that the crystals were formed completely. The FT-IR spectrum of the MIL-53(Fe) (Figure 1(b)) exhibits the typical vibrational bands of the car-

boxylic acid function in the region of 1400–1700 cm^{-1}. The adsorption band of the carboxyl group of the ligand coordinated to the Fe(III) ion is visible at 1585 cm^{-1}. The peak at 749 cm^{-1} corresponds to the C–H bonding vibration of the benzene rings [37, 38]. Moreover, the presence of the Fe–O vibration at 545 cm^{-1} indicates the formation of a metal-oxo bond between the carboxylic group of terephthalic acid and the Fe(III) [39].

The surface morphology of the MIL-53(Fe) was investigated by using SEM that is shown in Figure 2(a), which can be observed that the MIL-53(Fe)'s particle size is quite small and homogeneous with the distribution of the particle size around 0.8 μm (Figure 2(b)). The TEM images (Figures 2(c) and 2(d)) indicate that there are small pseudospherical particles in the range of 5–8 nm which were attached to the surface of the MIL-53(Fe) crystals [26]. The small particle size and the homogeneous particle size distribution of the obtained MIL-53(Fe) have an important role in improving the repeatability and reproducibility of electrochemical sensors.

3.2. Electrochemical Characterizations of MIL-53(Fe). Figure 3 shows the CV (Figure 3(a)) and EIS spectra (Figure 3(b)) of the GCE/bare (curve A) and GCE/MIL-53(Fe) (curve B) electrodes performed in $K_3Fe(CN)_6/K_4Fe(CN)_6$ (0.005 M) and 0.1 M KCl solution. It can be seen that there are two peaks on the two CV curves corresponding to the oxidation of $Fe(CN)_6^{4-}$ and the reduction of $Fe(CN)_6^{3-}$ (Figure 3(a)). In the case of the GCE/MIL-53(Fe) electrode (curve B), the peak current is higher than that of the bare GCE electrode (curve A). This result can be attributed to the increase in the electroactive area when the MIL-53(Fe) was loaded on the GCE, leading to the accumulation of the electroactive species on the electrode surface and the increase in the current density. The EIS spectra (Figure 3(b)) of the two different electrodes consist of two parts: a semicircle which characterizes the charge transfer process and a linear region which characterizes the diffusion process. These EIS spectra can be simulated by an equivalent circuit based on the Randles model (Figure 3(b), inset). This equivalent circuit
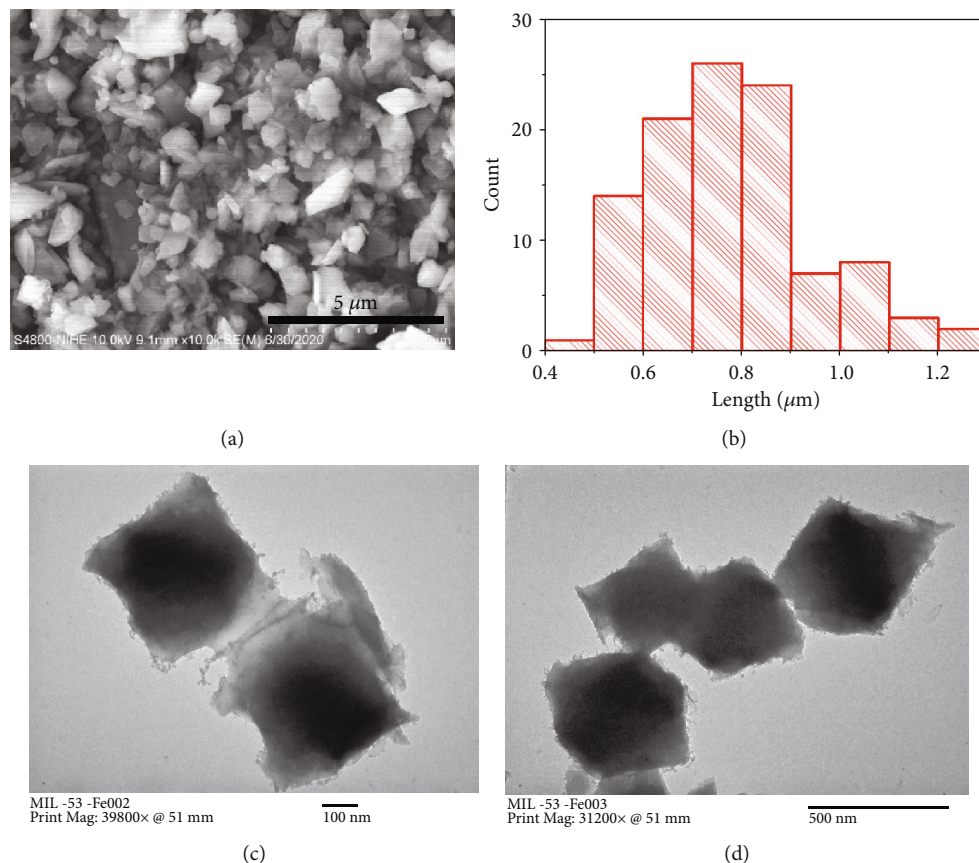
(a)

(b)

(c)

(d)

FIGURE 2: (a) SEM image; (b) particle diameter distribution; (c, d) TEM images of the synthesized MIL-53(Fe).

(a)

(b)
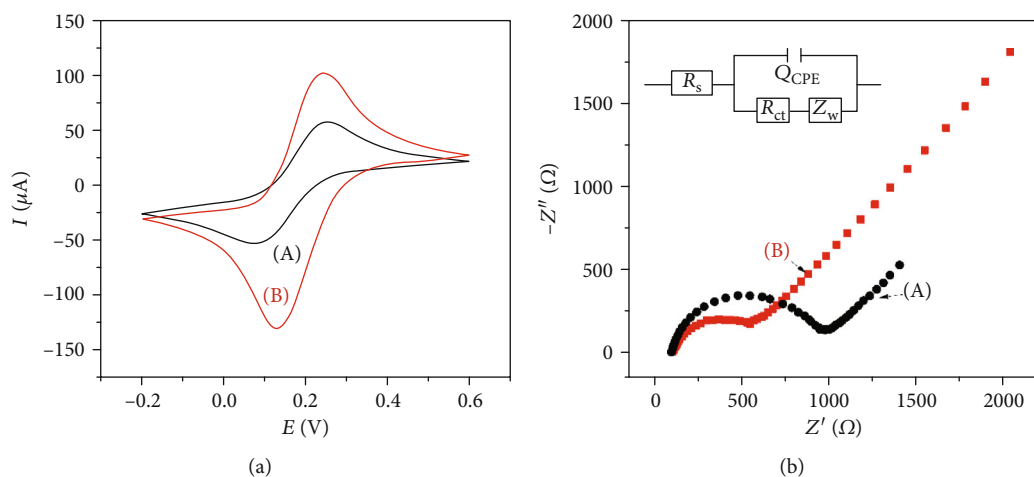
FIGURE 3: (a) Cyclic voltammograms of (A) GCE/bare and (B) GCE/MIL-53(Fe) electrodes; (b) EIS spectra (Nyquist plots) of (A) GCE/bare and (B) GCE/MIL-53(Fe) electrodes (inset: Randles equivalent circuit). Experimental conditions: $K_3Fe(CN)_6/K_4Fe(CN)_6$ (0.005 M) and 0.1 M KCl solution. CVs were recorded at a scan rate of $30\,mV\,s^{-1}$. EIS spectra were measured with frequency range 100 kHz to 100 mHz, $E_{AC} = 5\,mV$, $E_{DC} = 180\,mV$.

consists of a solution resistance (R_s), a charge transfer resistance (R_{ct}), a constant phase element (Q_{CPE}), and a Warburg diffusion coefficient (W). Fitted R_{ct} results of the GCE/MIL-53(Fe) and bare GCE were 425 Ω and 828 Ω, respectively, which implied that the MIL-53(Fe) layer-modified GCE with the small particle size, the homogeneous particle size distri-

bution, and the high electrochemically effective surface area was able to significantly enhance the electrochemical response of the working electrode. These EIS results are suitable for the CV results obtained in Figure 3(a).

CVs of the GCE/MIL-53(Fe) electrode in 0.1 M KCl solution containing 5 mM $Fe(CN)_6^{3-/4-}$ at different scan rates

FIGURE 4: (a) Cyclic voltammograms of the GCE/MIL-53(Fe) electrode in 0.1 M KCl solution containing 5 mM $Fe(CN)_6^{3-/4-}$ at different scan rates of 25, 30, 35, 40, 45,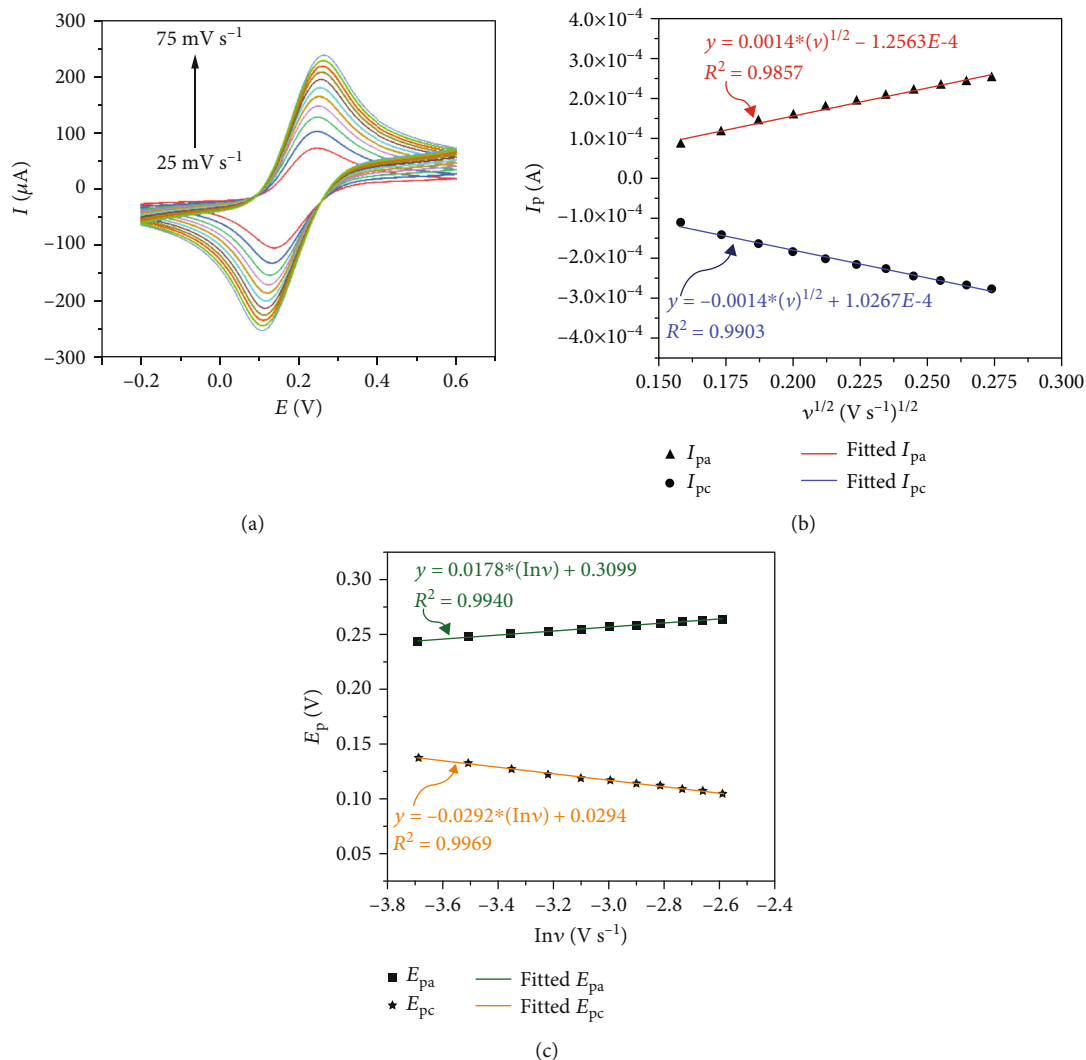 50, 55, 60, 65, 70, and 75 mV s^{-1}; (b) the relationships between the currents of anodic and cathodic peaks and the square root of the scan rate ($v^{1/2}$) and their corresponding linear fit lines: I_{pa}, the red line with the triangle symbols, and I_{pc}, the blue line with the circle symbols; (c) the relationships between the potentials of anodic and cathodic peaks and ln v and their corresponding linear fit lines: E_{pa}, the green line with the square symbols, and E_{pc}, the orange line with the star symbols.

from 25 to 75 mV s^{-1} are shown in Figure 4(a). From these obtained data, the relationships between the currents of anodic and cathodic peaks and the square root of the potential scan rate are plotted in Figure 4(b), i.e., with the relationship between I_{pa} vs. $v^{1/2}$ (marked by the red line with the triangle symbols)

$$y = 0.0014 \times v^{1/2} - 1.2563 \times 10^{-4} \ (R^2 = 0.9857) \qquad (1)$$

and I_{pc} vs. $v^{1/2}$ (the blue line with the circle symbols)

$$y = -0.0014 \times v^{1/2} + 1.0267 \times 10^{-4} \ (R^2 = 0.9903). \qquad (2)$$

In the cases of both anodic and cathodic peaks, the peak currents expressed linear dependence on the square root of the potential scan rate, indicating that the electrochemical

processes occurred in a diffusion-controlled regime on the MIL-53(Fe)-modified GCE electrode [40]. Besides, the relationships between the potentials of anodic and cathodic peaks and ln v were investigated, and their corresponding linear fit lines for each set of experimental data have been shown in Figure 4(c), i.e., E_{pa} vs. ln v (the green line with the square symbols)

$$y = 0.0178 \times \ln v + 0.3099 \ (R^2 = 0.9940) \qquad (3)$$

and E_{pc} vs. ln v (the orange line with the star symbols)

$$y = -0.0292 \times \ln v + 0.0294 \ (R^2 = 0.9969). \qquad (4)$$

The gradually increasing trend of the potential peak difference ($\Delta E = E_{pa} - E_{pc}$) with the potential scan rate v
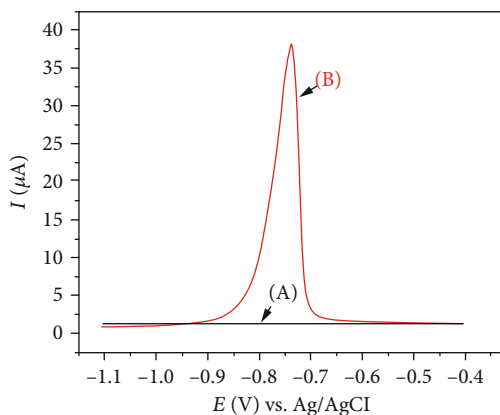
FIGURE 5: DPV results of (a) GCE/bare and (b) GCE/MIL-53(Fe) electrodes measured in $20\,\mu M$ Cd(II) and 0.1 M ABS (pH = 5.0) solution.

demonstrates that the electrochemical processes which happened on the GCE/MIL-53(Fe) electrode surface are quasireversible [41]. Moreover, as can be seen in Figure 4(c), both the potentials of anodic and cathodic peaks depend linearly on the natural logarithm of the scan rate, and these relationships can be expressed by the following equations [41, 42]:

$$E_{pa} = E^0 + m\left[0.78 + \ln\left(\frac{D^{1/2}}{k^0}\right) - 0.5\ln m\right] + 0.5m\ln v,$$

$$(5)$$

$$m = \frac{RT}{(1-\alpha)nF},$$

$$(6)$$

$$E_{pc} = E^0 - m'\left[0.78 + \ln\left(\frac{D^{1/2}}{k^0}\right) - 0.5\ln m'\right] - 0.5m'\ln v,$$

$$(7)$$

$$m' = \frac{RT}{\alpha nF},$$

$$(8)$$

where v (V s^{-1}) is the scan rate, E^0 (V) is the formal standard potential, α is the charge transfer coefficient, n is the number of transported electrons, k^0 (cm s^{-1}) is the electron transfer rate constant, D (cm^2 s^{-1}) is the diffusion coefficient, R is gas constant ($R = 8.314\,J\,mol^{-1}\,K^{-1}$), T is working temperature ($T = 298\,K$), and F is Faraday's constant ($F = 96480$ C mol^{-1}). The values of α and n can be calculated from the slopes of E_{pa} vs. ln v and E_{pc} vs. ln v, and the results are that the value of α is 0.379 and the value of n is 1.161. The value of n verified that the oxidation of Fe(CN)$_6^{4-}$ and the reduction of Fe(CN)$_6^{3-}$ which occurred on the GCE/MIL-53(Fe) electrode surface are through monoelectronic steps. The diffusion coefficients (D_O and D_R) of ferri- and ferrocyanide ions in 0.1 M KCl medium at 25°C are 7.20×10^{-6} cm^2 s^{-1} and 6.66×10^{-6} cm^2 s^{-1}, respectively [43]. From the intercepts of E_{pa} vs. ln v and E_{pc} vs. ln v and using $E^0 = (E_{pa} + E_{pc})/2 = 0.19\,V$ [41], the values of k^0 were calculated as

1.069×10^{-3} cm s^{-1} and 1.489×10^{-3} cm s^{-1} for the anodic and the cathodic branches, respectively, and the average value was 1.279×10^{-3} cm s^{-1}. These results further confirmed that, in the considered scan rate range, the oxidation of Fe(CN)$_6^{4-}$ and the reduction of Fe(CN)$_6^{3-}$ which occurred on the GCE/MIL-53(Fe) electrode surface are quasireversible.

The electrochemically effective surface area (A) of modified electrodes is an important factor increasing electrochemical active sites, enhancing electrochemical response, and improving sensitivity of electrochemical sensors [44]. In this work, the electrochemically effective surface area of the GCE/MIL-53(Fe) electrode was determined by CV data analysis by using the Randles-Sevcik equation for quasireversible reactions as follows [45]:

$$I_p = 3.01 \times 10^5 \alpha^{1/2} n^{3/2} A C_0 D^{1/2} v^{1/2},$$

$$(9)$$

where v (V s^{-1}), α, n, and D (cm^2 s^{-1}) were mentioned in Equations (5)–(8). A (cm^2) is the electrochemically effective surface area of the electrode, C_0 (mol cm^{-3}) is the concentration of redox species, and I_p (A) is the redox peak current. From Equation (9) and using the slope of the linear dependence of the anodic peak current on the square root of the potential scan rate (Figure 4(b)), the value of A of the GCE/MIL-53(Fe) electrode was calculated to be 0.453 cm^2. Thus, the electrochemically effective surface area of the modified GCE electrodes using the synthesized MIL-53(Fe) is significantly larger than that of the GCE electrodes ($A_{GCE} = 0.071$ cm^2). The above EIS and CV results verified that the synthesized MIL-53(Fe) material was successfully immobilized on the GCE electrode surface, the electrochemical activity of the GCE/MIL-53(Fe) electrode was stable, and the MIL-53(Fe) with a high electrochemically effective surface area was able to significantly enhance the electrochemical response of the WE. These data also further confirmed that in this study, the drop-casting method used to immobilize the MIL-53(Fe) on the WE surface was simple, convenient, and effective.

3.3. Detection of Cd(II) Ions Using MIL-53(Fe)-Based Electrochemical Sensors. To assess the ability of GCE/MIL-53(Fe) as an electrochemical sensor for detection of cadmium (Cd(II)) ions in aqueous solutions, the DPV of the GCE/bare and GCE/MIL-53(Fe) electrodes were recorded in 0.1 M ABS (pH = 5.0) solution containing $20\,\mu M$ Cd(II) (Figure 5). As can be observed in Figure 5 (curve a), with GCE, no obvious response was observed when the accumulation process was carried out for 120 s at -1.2 V in the solution containing $20\,\mu M$ Cd^{2+} and 0.1 M ABS buffer (pH = 5.0). This result implies that with the bare GCE, the ability to be used as an electrochemical sensor for detection of cadmium ions in aqueous solutions was almost negligible.

In contrast, the DPV result of GCE/MIL-53(Fe) (Figure 5, curve b) showed a strong response peak at -0.75 V with the peak current $I_{peak} = 37.29\,\mu A$, which characterizes the presence of Cd(II) ions in the aqueous solution, although the concentration of cadmium ions is relatively low
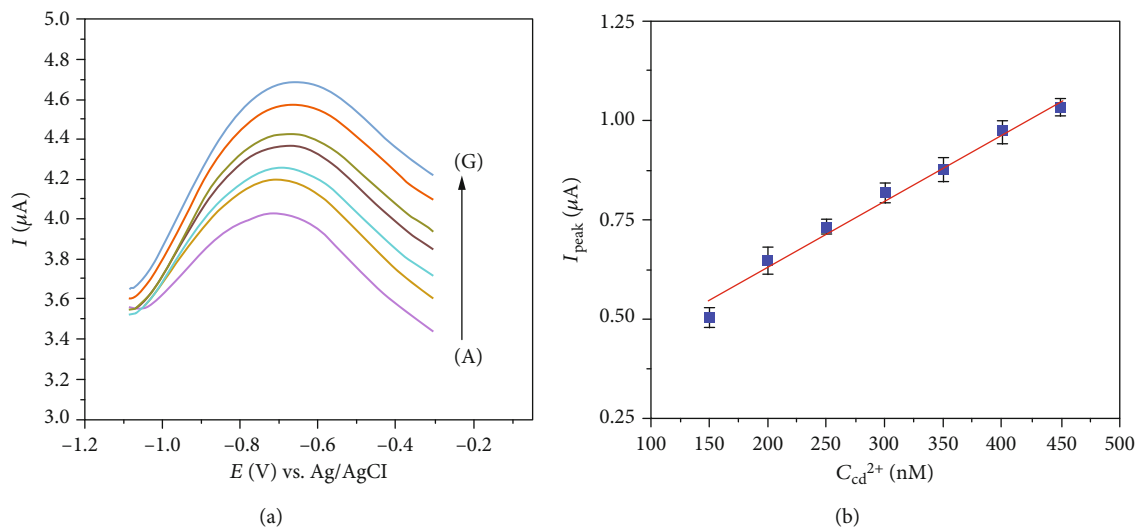
(a)

(b)

Figure 6: (a) DPV results of GCE/MIL-53(Fe) electrodes in Cd(II) solutions (with 0.1 M ABS (pH = 5.0)). Cd(II) concentrations (from A to G): 150, 200, 250, 300, 350, 400, and 450 nM; (b) response of the electrochemical sensors to different concentrations of Cd(II) ions.

Table 1: Comparison of the electrochemical sensor with someone else's in the previous literature.

Surface modification	Linear range (M)	Detection limit (M)	Reference
GCE/chitosan-carbon nanotubes	$1.334 \times 10^{-5} - 3.950 \times 10^{-5}$	7.1×10^{-6}	[47]
GCE/LAL*-AuNPs	$3.0 \times 10^{-7} - 1.4 \times 10^{-6}$	3.0×10^{-7}	[48]
GCE/MIL-100(Cr)	$0 - 1.0 \times 10^{-5}$	4.4×10^{-8}	[49]
GCE/porous carbon-PdNPs	$5.0 \times 10^{-7} - 5.5 \times 10^{-6}$	4.1×10^{-8}	[50]
GCE/MIL-53(Fe)	$1.5 \times 10^{-7} - 4.5 \times 10^{-7}$	1.6×10^{-8}	This work

*LAL: laser ablation in liquid.

(20 μM). This result implies that the electrochemical sensor based on the MIL-53(Fe)-modified GCE can be used for determination of Cd(II) ions in aqueous solutions.

These obtained results can be attributed to the MIL-53(Fe) material with abundant adsorption sites and a large surface area, which can adsorb Cd(II) ions from the aqueous solution, leading the Cd(II) ion enrichment process onto the GCE/MIL-53(Fe) surface. Therefore, the electrochemical measurements were performed to detect the presence of Cd(II) ions on the electrode surface at low concentration. In addition, the enhanced current at the GCE/MIL-53(Fe) electrode compared to the bare GCE also indicates that the obtained MIL-53(Fe) with the high electrochemically effective surface area exhibits electrocatalytic activity to the reduction of the target. These above results suggest that using MIL-53(Fe) material in development of the electrochemical sensor for detection of Cd(II) ions is totally suitable.

Figure 6(a) shows the DPV response results of the GCE/-MIL-53(Fe) with different Cd(II) concentrations. As can be seen, the increase in the concentration of Cd(II) target caused an increase in the peak current (I_{peak}) of the responses. The change in the electrochemical signal was obtained even at low concentration of Cd(II) ions (150 nM). And this phenomenon becomes more obvious when the target concentra-

tion continues to rise (up to 450 nM). The above results are explained that when Cd(II) ions in the aqueous solutions increase, the amount of Cd(II) ions accumulated on the surface of the MIL-53(Fe) layer increases, which leads to increasing in response current of the DPV results. The sensitivity of the electrochemical sensors was investigated by plotting I_{peak} versus different Cd^{2+} concentrations (Figure 6(b)). It shows that a linear relationship between I_{peak} vs. $[Cd^{2+}]$ in the range from 150 nM to 450 nM is I_{peak} (μA) = 0.2946 + 0.0017 × $[Cd^{2+}]$ (nM) with a correlation coefficient of R^2 = 0.9809. Based on a signal-to-noise ratio characteristic of 3 (S/N = 3) [32, 46], the detection limit of Cd^{2+} ions on GCE/MIL-53(Fe) was estimated to be 16 nM. The fabricated electrochemical sensor was compared to someone else's which has been reported in the previous studies (Table 1). Results in Table 1 indicate that the GCE/MIL-53(Fe) in this work has a great applied potential for Cd^{2+} determination on the terms including simple fabrication, direct detection, rapid analysis time, and high sensitivity.

4. Conclusion

We have synthesized the metal-organic framework MIL-53(Fe) using the effective hydrothermal method with

optimized synthesis conditions. The synthesized MIL-53(Fe) was characterized by XRD, SEM/TEM, and FT-IR measurements, and the obtained results indicated that the formed MIL-53(Fe) was a single phase with narrow size distribution and the mean size was around 800 nm. A layer of MIL-53(Fe)-modified glassy carbon electrode (GCE/MIL-53(Fe)) was fabricated via the simple drop-casting technique. The CV and EIS measurements of the GCE/MIL-53(Fe) electrode indicated that the MIL-53(Fe) layer with the small particle size and the high electrochemically effective surface area was able to increase the electrochemical response and improve the sensitivity of the electrochemical sensor. The novel electrochemical sensor based on the MIL-53(Fe) was designed and developed to detect Cd(II) ions in aqueous solutions, and the detection limit of the sensor was 16 nM. The evaluated results demonstrated that the metal-organic framework MIL-53(Fe)-modified glassy carbon electrode (GCE/MIL-53(Fe)) has great promising for Cd^{2+} ion sensing in water samples with expressed advantages such as high sensitivity, direct detection, and rapid analysis time.

Data Availability

The data used to support the findings of this study are included within the article.

Conflicts of Interest

The authors declare that they have no conflicts of interest regarding the publication of this paper.

Acknowledgments

References

[1] J. Li, C. Yu, Y. N. Wu et al., "Novel sensing platform based on gold nanoparticle-aptamer and Fe-metal-organic framework for multiple antibiotic detection and signal amplification," *Environment International*, vol. 125, pp. 135–141, 2019.

[2] L. Ma, X. Zhang, M. Ikram, M. Ullah, H. Wu, and K. Shi, "Controllable synthesis of an intercalated ZIF-67/EG structure for the detection of ultratrace Cd^{2+}, Cu^{2+}, Hg^{2+} and Pb^{2+} ions," *Chemical Engineering Journal*, vol. 395, article 125216, 2020.

[3] X. Xu, X. Niu, X. Li, Z. Li, D. Du, and Y. Lin, "Nanomaterial-based sensors and biosensors for enhanced inorganic arsenic detection: a functional perspective," *Sensors and Actuators B: Chemical*, vol. 315, article 128100, 2020.

[4] H. A. Vu, M. H. Nguyen, H. A. Vu-Thi et al., "Speciation analysis of arsenic compounds by high-performance liquid chromatography in combination with inductively coupled plasma dynamic reaction cell quadrupole mass spectrometry: application for Vietnamese rice samples," *Journal of Analytical Methods in Chemistry*, vol. 2019, Article ID 5924942, 10 pages, 2019.

[5] H. Chen, T. Yang, F. Liu, and W. Li, "Electrodeposition of gold nanoparticles on cu-based metal-organic framework for the electrochemical detection of nitrite," *Sensors and Actuators B: Chemical*, vol. 286, pp. 401–407, 2019.

[6] C.-S. Liu, J. Li, and H. Pang, "Metal-organic framework-based materials as an emerging platform for advanced electrochemical sensing," *Coordination Chemistry Reviews*, vol. 410, article 213222, 2020.

[7] T. R. Das and P. K. Sharma, "Sensitive and selective electrochemical detection of Cd^{2+} by using bimetal oxide decorated graphene oxide (Bi_2O_3/Fe_2O_3@GO) electrode," *Microchemical Journal*, vol. 147, article 1203, 2019.

[8] S. Duan and Y. Huang, "Electrochemical sensor using NH_2-MIL-88(Fe)-rGO composite for trace Cd^{2+}, Pb^{2+}, and Cu^{2+} detection," *Journal of Electroanalytical Chemistry*, vol. 807, pp. 253–260, 2017.

[9] X. Fang, B. Zong, and S. Mao, "Metal-organic framework-based sensors for environmental contaminant sensing," *Nano-Micro Letters*, vol. 10, no. 4, p. 64, 2018.

[10] D. Feng, P. Li, X. Tan et al., "Electrochemiluminescence aptasensor for multiple determination of Hg^{2+} and Pb^{2+} ions by using the MIL-53(Al)@CdTe-PEI modified electrode," *Analytica Chimica Acta*, vol. 1100, pp. 232–239, 2020.

[11] X. Liao, H. Fu, T. Yan, and J. Lei, "Electroactive metal-organic framework composites: design and biosensing application," *Biosensors and Bioelectronics*, vol. 146, article 111743, 2019.

[12] L. T. Tran, H. V. Tran, H. Thi Minh Dang, C. D. Huynh, and T. A. Mai, "Silver nanoparticles decorated polyaniline nanowires-based electrochemical DNA sensor: two-step electrochemical synthesis," *Journal of the Electrochemical Society*, vol. 167, no. 8, article 087508, 2020.

[13] H. V. Le and Q. T. Le, "Electrochemical preparation of polyaniline- supported Cu-CuO core-shell on 316L stainless steel electrodes for nonenzymatic glucose sensor," *Advances in Polymer Technology*, vol. 2020, Article ID 6056919, 7 pages, 2020.

[14] A. Mourya, B. Mazumdar, and S. K. Sinha, "Determination and quantification of heavy metal ion by electrochemical method," *Journal of Environmental Chemical Engineering*, vol. 7, no. 6, article 103459, 2019.

[15] T. L. Tran, T. X. Chu, D. C. Huynh, D. T. Pham, T. H. T. Luu, and A. T. Mai, "Effective immobilization of DNA for development of polypyrrole nanowires based biosensor," *Applied Surface Science*, vol. 314, pp. 260–265, 2014.

[16] H. V. Tran, N. D. Nguyen, B. Piro, and L. T. Tran, "Fabrication of a quinone containing layer on gold nanoparticles directed to a label-free and reagentless electrochemical miRNA sensor," *Analytical Methods*, vol. 9, no. 18, pp. 2696–2702, 2017.

[17] V. Mariyappan, S. Manavalan, S.-M. Chen, G. Jaysiva, P. Veerakumar, and M. Keerthi, "Sr@FeNi-S nanoparticle/carbon nanotube nanocomposite with superior electrocatalytic activity for electrochemical detection of toxic mercury(II)," *ACS Applied Electronic Materials*, vol. 2, no. 7, pp. 1943–1952, 2020.

[18] P. Veerakumar, S. M. Chen, R. Madhu, V. Veeramani, C. T. Hung, and S. B. Liu, "Nickel nanoparticle-decorated porous carbons for highly active catalytic reduction of organic dyes and sensitive detection of hg(II) ions," *ACS Applied Materials & Interfaces*, vol. 7, no. 44, pp. 24810–24821, 2015.

[19] T. L. Tran, T. T. Nguyen, T. T. Huyen Tran, V. T. Chu, Q. Thinh Tran, and A. Tuan Mai, "Detection of influenza A virus using carbon nanotubes field effect transistor based DNA sensor," *Physica E: Low-dimensional Systems and Nanostructures*, vol. 93, pp. 83–86, 2017.

[20] Y. Xue, S. Zheng, H. Xue, and H. Pang, "Metal-organic framework composites and their electrochemical applications," *Journal of Materials Chemistry A*, vol. 7, no. 13, pp. 7301–7327, 2019.

[21] R. Hu, X. Zhang, K.-N. Chi, T. Yang, and Y.-H. Yang, "Bifunctional MOFs-based ratiometric electrochemical sensor for multiplex heavy metal ions," *ACS Applied Materials & Interfaces*, vol. 12, no. 27, article 30770, p. 30778, 2020.

[22] Y. Wang, L. Wang, W. Huang et al., "A metal-organic framework and conducting polymer based electrochemical sensor for high performance cadmium ion detection," *Journal of Materials Chemistry A*, vol. 5, no. 18, pp. 8385–8393, 2017.

[23] L. Jiao, J. Y. R. Seow, W. S. Skinner, Z. U. Wang, and H.-L. Jiang, "Metal-organic frameworks: structures and functional applications," *Materials Today*, vol. 27, pp. 43–68, 2019.

[24] X. Wang, Y. Qi, Y. Shen et al., "A ratiometric electrochemical sensor for simultaneous detection of multiple heavy metal ions based on ferrocene-functionalized metal-organic framework," *Sensors and Actuators B: Chemical*, vol. 310, article 127756, 2020.

[25] S. Guo, Y. Zhu, Y. Yan et al., "(Metal-organic framework)-polyaniline sandwich structure composites as novel hybrid electrode materials for high-performance supercapacitor," *Journal of Power Sources*, vol. 316, pp. 176–182, 2016.

[26] T. A. Vu, G. H. Le, C. D. Dao et al., "Arsenic removal from aqueous solutions by adsorption using novel MiL-53(Fe) as a highly efficient adsorbent," *RSC Advances*, vol. 5, no. 7, pp. 5261–5268, 2015.

[27] S. Gu, Z. Bai, S. Majumder, B. Huang, and G. Chen, "Conductive metal-organic framework with redox metal center as cathode for high rate performance lithium ion battery," *Journal of Power Sources*, vol. 429, pp. 22–29, 2019.

[28] A. Gupta, S. K. Bhardwaj, A. L. Sharma, K. H. Kim, and A. Deep, "Development of an advanced electrochemical biosensing platform for E. coli using hybrid metal-organic framework/polyaniline composite," *Environmental Research*, vol. 171, pp. 395–402, 2019.

[29] W. Ye, Y. Li, J. Wang et al., "Electrochemical detection of trace heavy metal ions using a Ln-MOF modified glass carbon electrode," *Journal of Solid State Chemistry*, vol. 281, article 121032, 2020.

[30] J. Zhou, G. Tian, L. Zeng, X. Song, and X. W. Bian, "Nanoscaled metal-organic frameworks for biosensing, imaging, and cancer therapy," *Advanced Healthcare Materials*, vol. 7, no. 10, article 1800022, 2018.

[31] D. T. C. Nguyen, H. T. N. Le, T. S. Do et al., "Metal-organic framework MIL-53(Fe) as an adsorbent for ibuprofen drug removal from aqueous solutions: response surface modeling and optimization," *Journal of Chemistry*, vol. 2019, Article ID 5602957, 11 pages, 2019.

[32] H. V. Tran, C. D. Huynh, T. D. Le, and H. S. Hoang, "Hydroxyapatite nano-rods/chitosan modified glassy carbon electrode for Cu(II) ions determination," *Electronic Materials Letters*, vol. 16, no. 4, pp. 396–403, 2020.

[33] H. V. Tran, L. D. Tran, C. T. Ba et al., "Synthesis, characterization, antibacterial and antiproliferative activities of monodisperse chitosan-based silver nanoparticles," *Colloids and Surfaces A: Physicochemical and Engineering Aspects*, vol. 360, no. 1-3, pp. 32–40, 2010.

[34] J. Gordon, H. Kazemian, and S. Rohani, "Rapid and efficient crystallization of MIL-53(Fe) by ultrasound and microwave irradiation," *Microporous and Mesoporous Materials*, vol. 162, pp. 36–43, 2012.

[35] C. Scherb, A. Schödel, and T. Bein, "Directing the structure of metal-organic frameworks by oriented surface growth on an organic monolayer," *Angewandte Chemie International Edition*, vol. 47, no. 31, pp. 5777–5779, 2008.

[36] J. Gordon, H. Kazemian, and S. Rohani, "MIL-53(Fe), MIL-101, and SBA-15 porous materials: potential platforms for drug delivery," *Materials Science and Engineering: C*, vol. 47, pp. 172–179, 2015.

[37] P. Horcajada, C. Serre, G. Maurin et al., "Flexible porous metal-organic frameworks for a controlled drug delivery," *Journal of the American Chemical Society*, vol. 130, no. 21, pp. 6774–6780, 2008.

[38] A. Banerjee, R. Gokhale, S. Bhatnagar et al., "MOF derived porous carbon-Fe_3O_4 nanocomposite as a high performance, recyclable environmental superadsorbent," *Journal of Materials Chemistry*, vol. 22, no. 37, article 19694, 2012.

[39] C. Gong, D. Chen, X. Jiao, and Q. Wang, "Continuous hollow α-Fe_2O_3 and α-Fe fibers prepared by the sol-gel method," *Journal of Materials Chemistry*, vol. 12, no. 6, pp. 1844–1847, 2002.

[40] T.-X. Chu, V.-P. Vu, H.-T. Tran, T.-L. Tran, Q.-T. Tran, and T. Le Manh, "Molecularly imprinted polyaniline nanowire-based electrochemical biosensor for chloramphenicol detection: a kinetic study of aniline electropolymerization," *Journal of the Electrochemical Society*, vol. 167, no. 2, article 027527, 2020.

[41] S. Corona-Avendaño, G. Alarcón-Angeles, M. T. Ramírez-Silva, G. Rosquete-Pina, M. Romero-Romo, and M. Palomar-Pardavé, "On the electrochemistry of dopamine in aqueous solution. Part I: the role of [SDS] on the voltammetric behavior of dopamine on a carbon paste electrode," *Journal of Electroanalytical Chemistry*, vol. 609, no. 1, pp. 17–26, 2007.

[42] J. Li, L. He, J. Jiang et al., "Facile syntheses of bimetallic Prussian blue analogues $(K_xM[Fe(CN)_6]\cdot nH_2O$, M=Ni, Co, and Mn) for electrochemical determination of toxic 2-nitrophenol," *Electrochimica Acta*, vol. 353, article 136579, 2020.

[43] S. J. Konopka and B. McDuffie, "Diffusion coefficients of ferri- and ferrocyanide ions in aqueous media, using twin-electrode thin-layer electrochemistry," *Analytical Chemistry*, vol. 42, no. 14, pp. 1741–1746, 2002.

[44] Y. Ge, M. B. Camarada, L. Xu et al., "A highly stable black phosphorene nanocomposite for voltammetric detection of clenbuterol," *Mikrochimica Acta*, vol. 185, no. 12, article 566, 2018.

[45] J. Krejci, Z. Sajdlova, V. Nedela et al., "Effective surface area of electrochemical sensors," *Journal of the Electrochemical Society*, vol. 161, no. 6, pp. B147–B150, 2014.

[46] H. V. Tran, B. Piro, S. Reisberg, L. D. Tran, H. T. Duc, and M. C. Pham, "Label-free and reagentless electrochemical detection of microRNAs using a conducting polymer nanostructured by carbon nanotubes: application to prostate cancer biomarker miR-141," *Biosensors and Bioelectronics*, vol. 49, pp. 164–169, 2013.

[47] K.-H. Wu, H.-M. Lo, J.-C. Wang, S.-Y. Yu, and B.-D. Yan, "Electrochemical detection of heavy metal pollutant using crosslinked chitosan/carbon nanotubes thin film electrodes," *Materials Express*, vol. 7, no. 1, pp. 15–24, 2017.

[48] X. Xu, G. Duan, Y. Li et al., "Fabrication of gold nanoparticles by laser ablation in liquid and their application for simultaneous electrochemical detection of Cd^{2+}, Pb^{2+}, Cu^{2+}, Hg^{2+},"

ACS Applied Materials & Interfaces, vol. 6, no. 1, pp. 65–71, 2013.

[49] D. Wang, Y. Ke, D. Guo, H. Guo, J. Chen, and W. Weng, "Facile fabrication of cauliflower-like MIL-100(Cr) and its simultaneous determination of Cd^{2+}, Pb^{2+}, Cu^{2+} and Hg^{2+} from aqueous solution," *Sensors and Actuators B: Chemical*, vol. 216, pp. 504–510, 2015.

[50] P. Veerakumar, V. Veeramani, S. M. Chen, R. Madhu, and S. B. Liu, "Palladium nanoparticle incorporated porous activated carbon: electrochemical detection of toxic metal ions," *ACS Applied Materials & Interfaces*, vol. 8, no. 2, pp. 1319–1326, 2016.